New Physics with Atmospheric Neutrinos

By

Carlos Alberto Argüelles Delgado

A dissertation submitted in partial fulfillment of
the requirements for the degree of

Doctor of Philosophy
(Physics)

at the
UNIVERSITY OF WISCONSIN–MADISON
2015

Date of final oral examination: August 19, 2015

The dissertation is approved by the following members of the Final Oral Committee:

Francis Halzen, Professor, Physics

Albrecht Karle, Professor, Physics

Kael Hanson, Professor, Physics

Vernon Barger, Professor, Physics

Paolo Desiati, Scientist (Wisconsin IceCube Particle Astrophysics Center)

Abstract

The purpose of this thesis is to look for new phenomena in the IceCube atmospheric neutrino spectrum. First we revisit the high energy neutrino cross section in the perturbative QCD (pQCD) framework and perform a new next-to-next-to leading order calculation with new parton distribution functions. We further use the color dipole model of the nucleon and the assumption that cross sections behave asymptotically as $\ln^2(s)$ to extend the prediction of neutrino cross sections beyond pQCD. We then study the problem of neutrino oscillations with non-coherent interactions and solve the problem in the density matrix formalism efficiently by representing the neutrino state in terms of the SU(N) generators. This technique is used in three new physics scenarios: sterile neutrinos, non-standard interactions, Lorentz violation. Besides studying the phenomenology of this models in the atmospheric flux, the effect of Lorentz violation in the astrophysical flavor ratio is also discussed. We find that, given the current bounds, large deviations from the standard (1:1:1) expectation can be found. Having developed in detail the sterile neutrino phenomenology in IceCube a search for sterile neutrino signatures in the IceCube-86 2011 data is performed. No significant evidence for an eV-sterile neutrino is found and strong limits are put in the mixing angle improving by more than an order of magnitude bounds from ν_μ disappearance.

AGRADECIMIENTOS

"Andábamos sin buscarnos pero sabiendo que andábamos para encontrarnos."

— Julio Cortázar, Rayuela.[0]

Estoy seguro que esta es la sección más importante de este modesto trabajo. Uno no puede escribir ecuaciones sin antes saber andar. Y uno no puede aprender a andar en soledad; esos primeros pasos solo son posibles cuando el cariño de los padres se extiende unos largos metros dándonos valor para dar pasos al vacío, al mañana. Corresponde entonces agradecer primero a mis padres, Carlos y Sarisa, quienes me han apoyado incondicionalmente durante estos largos años a pesar de mis grandes defectos. Estos primeros pasos no fueron solitarios, mas bien fui acompañado por mis dos queridos hermanos Alonso y Sebastian; quienes siempre estuvieron dispuestos a jugar y acompañar. Muchas gracias hermanos. Los agradecimientos familiares no pueden terminar aquí; los hago extensivos a mis primos, tíos y abuelos. Muchas gracias a todos.

Más aún, es claro que este trabajo no hubiera sido posible sin el enérgico soporte de mi asesor, Francis Halzen, quien no solo supo encaminar mis esfuerzos, sino que siempre estuvo dispuesto a conversar y, sobretodo, discutir con emoción ideas nuevas. He crecido y aprendido mucho bajo tu tutela. Nuevamente, muchas gracias Francis: ¡salud!

No puedo dejar de mencionar a mis más cercanos colabores y coanalizadores: Jordi y Ben. Ustedes son físicos y amigos más que excelentes. He aprendido mucho de ustedes. Es claro que uno no puede encontrar la verdad sin tener al lado un amigo que le increpe, le discuta, le cuestione, le corrija. ¡Gracias por darme a palos cuando me equivocaba! Jordi muchas gracias por tu amistad y por siempre poner las cosas en perspectiva, en buscar la explicación y el método simple. Ben también muchas gracias por tu amistad, eres exceptional, y por empujar este trabajo día a día con gran criterio e inteligencia.

Quien lea esta tésis más allá de las primeras lineas pronto encontrará multiples referencias al trabajo de Chris; es evidente que todo el análisis descansa sobre su cuantioso y cuidadosamente elaborado trabajo.

[0] We went around without looking for each other, but knowing we went around to find each other.

La paciencia y voluntad de ayudar de Chris debe ser infinita. Recuerdo muchas noches, tardes, mañanas de intensas conversaciones con él en las cuales trataba de enseñarme con la más grande humildad. Muchas gracias Chris.

Ellos no son los únicos excelentes amigos y físicos que me han acompañado en estos años: hay muchos más. Mencionarlos a todos y listar sus innumerables cualidades sería un trabajo titaníco que sobrepasaría largarmente las páginas de esta tesis. No obstante, en estas breves lineas quisiera mencionar algunos más de ellos. Joachim: gracias por invitarme más de una vez a trabajar contigo en Mainz, tomar un helado, y por enriquecedoras y divertidas discusiones. Logan: muchas gracias por tener una actitud crítica en nuestros trabajos y por, al mismo tiempo, divertirnos tanto al hacerlos. Mike: gracias por seguir trabajando siempre con una sonrisa a pesar de las dificultades – eres un grande. Teppei: gracias por las divertidas conversaciones, por siempre buscar ideas nuevas y alegrarnos a todos el día. Alberto: gracias por seguir conversando de física, por esas largas y entretenidas conversaciones en *Skype* y extensos cafes. Nate: gracias por tu amistad y por trabajar conmigo durante esos primeros semestres llenos de cursos y tareas.

Finalmente, gracias a todos en WIPAC y en el departamento de física. Especiales gracias a mis compañeros en armas en IceCube: es una gran colaboración.

Aunque estas páginas solo platican de física estos años de estudio han ido mucho más allá de solucionar ecuaciones y hacer *plots*: ha sido una experiencia de vivencial. En ella no he estado solo. Además del soporte y compañia de mi familia, amigos y colegas anteriormente mencionados han habido muchos otros amigos que han decidido caminar conmigo. A continuación intentaré listarlos y agradecerles, pese a estar convencido que fallaré: ustedes son demasiados y han hecho tanto.

Zig, hermano, nos conocimos fortuitamente ya hace mucho en Buenos Aires, luego el destino fue generoso en reencontrarnos en Madison; más aún el azar nos hizo vecinos. En estos años hemos convertido una ciudad de concreto y ladrillo en un mural pintado con recuerdos. Uno podría intentar enumerarlos, ponerlos en palestra, pero esto no tendría utilidad. Lo pasado ya no esta ahí afuera, ya no se puede señalar, sino que es parte nuestra: tuya y mía. Como dice Borges: sólo aquello que se ha ido es lo que nos pertenece: nuestra amistad nos pertenece. Eres una persona extraordinaria, más que eso: eres único. Tampoco repetiré aquí tus pasiones y virtudes; son cuantiosas. Me basta decir que eres genial. Gracias por estos años y te agradezco por adelantado los cien siguientes.

Margarita, gracias por el tiempo maravilloso que pasamos juntos. Fue una aventura llena de drama y sonrisas. Tu amistad es algo que no se le puede poner precio. Muchas gracias por tu compañia, comprención, conversaciones adultas y fuertes abrazos. Estoy seguro que nos reencontraremos pronto. ¡Salud!

Zach, llegaste a la mitad de la aventura, pero en poco tiempo te volviste un gran amigo, consejero, confidente, y – simplemente – un grande. Eres un ejemplo de óptimismo, buena voluntad y ganas de vivir la vida. Pese a ser el más joven de los dos he aprendido mucho de ti. Te agradezco por tus enseñazas, pero tambíen por acompañarme en los momentos más difíciles: haciendo parecer lo imposible, posible y lo difícil solo una tarea trivial. Estoy convencido que los años venideros nos permitiran escribir juntos muchas aventuras y relatar momentos inolvidables. La historia esta para ser escrita.

Quisiera también agradecer demás mis amigos del *movie night* con quienes la amistad se extiende mucho más allá de las películas. Son compañeros semana a semana: Olivia, Larissa, Kostas, Merve, Mélanie, Esteban, Arelys, Will, et al. Ustedes son geniales. También a mis amigos *de Wisconsin* quienes se han esmerado en hacer estos años una gran experiencia, gracias por todo, Matt, Logan, Erik, Kendra, y otros. Y no puedo olvidar a mi californiana amiga Antonia, ¡gracias!

Muchas gracias a todos.

TABLE OF CONTENTS

LIST OF TABLES

Table Page

LIST OF FIGURES

Figure Page

Figure Page

Figure Page

Appendix
Figure

Chapter 1

Introduction

> *"En aquel Imperio, el Arte de la CartografÍa logró tal Perfección que el Mapa de una sola Provincia ocupaba toda una Ciudad, y el Mapa del Imperio, toda una Provincia. Con el tiempo, estos Mapas Desmesurados no satisficieron y los Colegios de Cartógrafos levantaron un Mapa del Imperio, que tenía el Tamaño del Imperio y coincidía puntualmente con él. Menos Adictas al Estudio de la Cartografía, las Generaciones Siguientes entendieron que ese dilatado Mapa era Inútil y no sin Impiedad lo entregaron a las Inclemencias del Sol y los Inviernos. En los Desiertos del Oeste perduran despedazadas Ruinas del Mapa, habitadas por Animales y por Mendigos; en todo el País no hay otra reliquia de las Disciplinas Geográficas."*
>
> — Jorge Luis Borges, Rigor en la ciencia.[1]

Dear reader, this thesis is not meant to be a self-contained document, but rather a guide through the work I have performed in my years as a PhD. student at the University of Wisconsin-Madison under the guidance

[1] In that Empire, the Art of Cartography attained such Perfection that the map of a single Province occupied the entirety of a City, and the map of the Empire, the entirety of a Province. In time, those Unconscionable Maps no longer satisfied, and the Cartographers Guilds struck a Map of the Empire whose size was that of the Empire, and which coincided point for point with it. The following Generations, who were not so fond of the Study of Cartography as their Forebears had been, saw that that vast Map was Useless, and not without some Pitilessness was it, that they delivered it up to the Inclemencies of Sun and Winters. In the Deserts of the West, still today, there are Tattered Ruins of that Map, inhabited by Animals and Beggars; in all the Land there is no other Relic of the Disciplines of Geography.

of Francis Halzen (FH). This means that this work stands between a thesis and a *mémoire*. Furthermore, knowledge of particle physics at the level of Halzen & Martin [1] is assumed. Experimental and statistical methods will be used without any prejudice; most of them are contained in the Particle Data Group Reviews [2]. Also, through out this text I set, as usual, $c = \hbar = 1$.

That said, the contents of the thesis is as follows. Chapter 2 describes my work on neutrino interactions and oscillations. Most of the material in this Chapter was published in [3] and was done in collaboration with L. Wille, M. Kroll, J. Salvado, M. Hall Reno, and F. Halzen; whom I acknowledge authorship. If you are already familiar with high energy neutrino interactions and oscillations you may freely skip that chapter. Chapter 3 is a brief review of the atmospheric neutrino flux both in its *conventional* and *prompt* component. The results of the conventional component using the AIRS satellite were performed by G. Collins et al. [4]. Work on *prompt* neutrinos mentioned was done in collaboration with L. Wille, M. Kroll, M. Hall Reno, FH, as reported in [3]; their authorship over this chapter cannot be denied. If you are already familiar with the details of the atmospheric neutrino flux, you may also choose to skip this chapter; though I strongly recommend that you read [5, 6, 4]. Chapter 4 describes new physics in neutrino oscillations that can be measured in IceCube. The work presented here was done using the SQuIDS [7] package as well as the yet unpublished ν-SQuIDS [8] extension that was developefd in collaboration with C. Weaver and J. Salvado. The theory on non standard interactions (NSI) follows Kopp [9] and recent work by [10, 11], the sterile neutrino phenomenology is a revisit of [12, 13], and the work on Lorentz Violation (LV) arises from the seminal work by Gonzalez-Garcia et al. [14]. Finally the discussion of the effects of LV on the astrophysical flavor ratio arise from a work with T. Katori and J. Salvado [15]. Of course, again, if you have already read these papers feel free to skip this chapter too. Chapter 5 describes the IceCube-86 sterile search performed with J. Salvado and B. J. P. Jones. The searched is based on the studies performed by C. Weaver [16, 17], thus knowledge of his work, thesis, and corresponding publication is assumed. In particular, IceCube jargon is extensively discussed and defined there. For a more self-contained recollection of the IceCube-86 sterile analysis please read B. J. P. Jones thesis - which is certainly an excellent write up and work. You should not skip this chapter since it is the main result of this thesis and cannot be found in any other reference published to the date; except the B. J. P. Jones thesis which I already mentioned. Chapter 6 concludes the discussion. Finally, dear reader, you will often find yourself feeling *in medias res*, this is normal, and by design. Please enjoy.

Chapter 2

Neutrino interactions and Oscillations

"Los muchos años lo habían reducido y pulido como las aguas a una piedra o las generaciones de los hombres a una sentencia."

— Jorge Luis Borges, El Sur.[2]

2.1 High energy neutrino interactions

At high energies the interactions of neutrinos with matter are given by the exchange of a vector boson with one of partons in the nucleon; this regime is known as deep inelastic scattering (DIS). The interaction can be mediated through either a charge, $W^{\pm}$, or neutral boson, Z^0, which define charge and neutral current interactions respectively. The Feynman diagram corresponding to these processes is shown in Figure 2.1, where for the charge current (CC) process we have $\nu_\alpha \mathrm{N} \to l_\alpha \mathrm{X}$ and for the neutral current (NC) $\nu_\alpha \mathrm{N} \to \nu_\alpha \mathrm{X}$. Furthermore, standard model lepton number conservation implies that if ν_α is incident, then only ν_α or l_α can be produced. And – in the massless lepton limit – the cross section is the same for all neutrino flavors, i.e. lepton flavor universality.

The total neutrino charged (neutral) current cross section for an incident neutrino with energy E_ν is given by

$$\sigma_{\nu p}^{\mathrm{CC/NC}}(E_\nu) = \int_{Q^2_{min}}^{s} dQ^2 \int_{Q^2/s}^{1} dx \left(\frac{\partial^2 \sigma_{\nu p}}{\partial Q^2 \partial x}\right)_{\mathrm{CC/NC}} \tag{2.1}$$

[2] His years had reduced and polished him as water does a stone or the generations of men do a sentence.

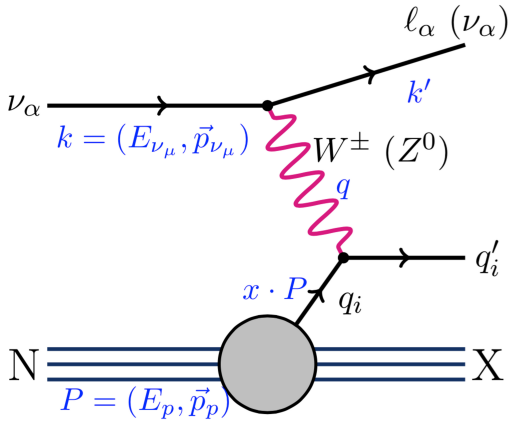

Figure 2.1: Diagram of νp interaction in the deep inelastic regime.

with $Q_{min} = 1$ GeV and

$$\begin{aligned} \frac{\partial^2 \sigma_{\nu N}}{\partial Q^2 \partial x} &= \frac{G_F^2}{4\pi x}\left(\frac{M_i^2}{M_i^2 + Q^2}\right)^2 \\ &\times \left[Y_+ F_T^\nu + 2(1-y)F_L^\nu \pm Y_- x F_3^\nu\right] \end{aligned} \tag{2.2}$$

Here $s \approx 2m_p E_\nu$, $Y_\pm = 1 \pm (1-y)^2$ with $y = Q^2/(xs)$, $M_i = M_W(M_Z)$ for charged (neutral) current interaction, and "$+$" ("$-$") refers to neutrinos (antineutrinos). To leading order in pQCD $F_L^\nu = 0$, while $F_T^\nu(x, Q^2)$ and $F_3^\nu(x, Q^2)$ are functions of the parton distribution functions, e.g., for a neutrino charged (CC) and neutral current (NC) interaction with an isoscalar target nucleon N [18]

$$\text{CC}: \begin{cases} F_T^\nu = x(u + \bar{u} + d + \bar{d} + 2s + 2b + 2\bar{c}) \\ x F_3^\nu = x(u - \bar{u} + d - \bar{d} + 2s + 2b - 2\bar{c}) \end{cases}, \tag{2.3}$$

$$\text{NC}: \begin{cases} F_T^\nu = x\left[\frac{1}{4}(L_u^2 + R_u^2 + L_d^2 + R_d^2))(u + \bar{u} + d + \bar{d})\right. \\ \quad + \frac{1}{2}(L_u^2 + R_u^2)(c + \bar{c}) \\ \quad \left. + \frac{1}{2}(L_d^2 + R_d^2)(s + b + \bar{s} + \bar{b})\right] \\ x F_3^\nu = x\left[\frac{1}{2}(L_u^2 - R_u^2 + L_d^2 - R_d^2)(u - \bar{u} + d - \bar{d})\right] \end{cases} \tag{2.4}$$

where $s_w = \sin(\theta_w)$ is the sine of the weak mixing angle and the weak couplings are given by $L_u = 1 - 4/3s_w^2$, $L_d = -1 + 2/3s_w^2$, $R_u = -4/3s_w^2$ and $R_d = 2/3s_w^2$. The antineutrino structure functions for charged

and neutral current are obtained by replacing $q \to \bar{q}$ and $F_3^{\bar{\nu}} \to -F_3^{\nu}$. For high neutrino energy, i.e. small x, the F_3 term does not contribute.

In Figure 2.2 F_2 for $Q^2 = 10^2, 10^5 \text{GeV}$ was plotted as a function of Bjorken-x using three parton distribution function (PDF) group fits: NNPDF[19], CT10 [20], and HERAPDF [21]. The solid lines correspond to the best fit value of the structure function, while the colored band represents the one sigma error band. The left panel illustrates F_2 dependence on x, namely, the fact that it monotonically increases as a x decreases. The error becomes appreciable for $x < 10^{-5}$, which corresponds to the limit of current experimental measurements. The right panel compares the results from different PDF fitting collaborations by plotting the ratio with respect to HERAPDF, remarking the fact that PDFs are uncertain in the very small x region ($x < 10^{-5}$) and the forward region ($x \sim 1$). In Figure 2.3 xF_3 has been plotted, as in Figure 2.2, three PDF sets fits included with their corresponding error. It is clear, from the left panel, that this structure function is a subleading contribution to the differential cross section and that, again, the error grows as a smaller x value is approached. Furthermore, on the right panel the ratio to the HERAPDF has been plotted with the corresponding error bars.

In the previous calculation the target mass has been neglected, which is an excellent approximation at high energies ($\sqrt{s} \gg M_N$). Nevertheless, a consistent treatment is also possible, in which one introduces the target mass corrected (TMC) structure functions F_i^{TMC} and modify Bjorken x to be

$$\xi = \frac{2x}{1 + \sqrt{1 + \frac{1+4M_N^2 x^2}{Q^2}}}, \tag{2.5}$$

where ξ is known as the Nachtmann variable [22], which satisfies $\xi \to x$ as $Q^2 \gg x^2 M_N^2$. As noted in [23] the TMC corrected structure functions can be written as a function of the usual structure functions as follows

$$F_i^{TMC}(x, Q^2) = \sum_i A^j F_j(\xi, Q^2) + B_i^j(\xi, Q^2) + C_i g_2(\xi, Q^2) \tag{2.6}$$

where the coefficients A^j,B_i^j, and C_i are given in Tables I-III in [23]. The result of this calculation is shown in Figure 2.4 for F_2^{TMC} and F_3^{TMC}. As expected the effect is larger as one decreases Q^2 and is only observable for $Q^2 \sim 1\text{GeV}^2$, being much more important in the forward regime ($x \sim 1$). Furthermore, in the lower panel the effect on F_2 and F_3 is shown and are found to be comparable in size. Thus in the IceCube regime, TMC corrections do not play an important role. However, in future low energy extensions, such as PINGU, it will play a role.

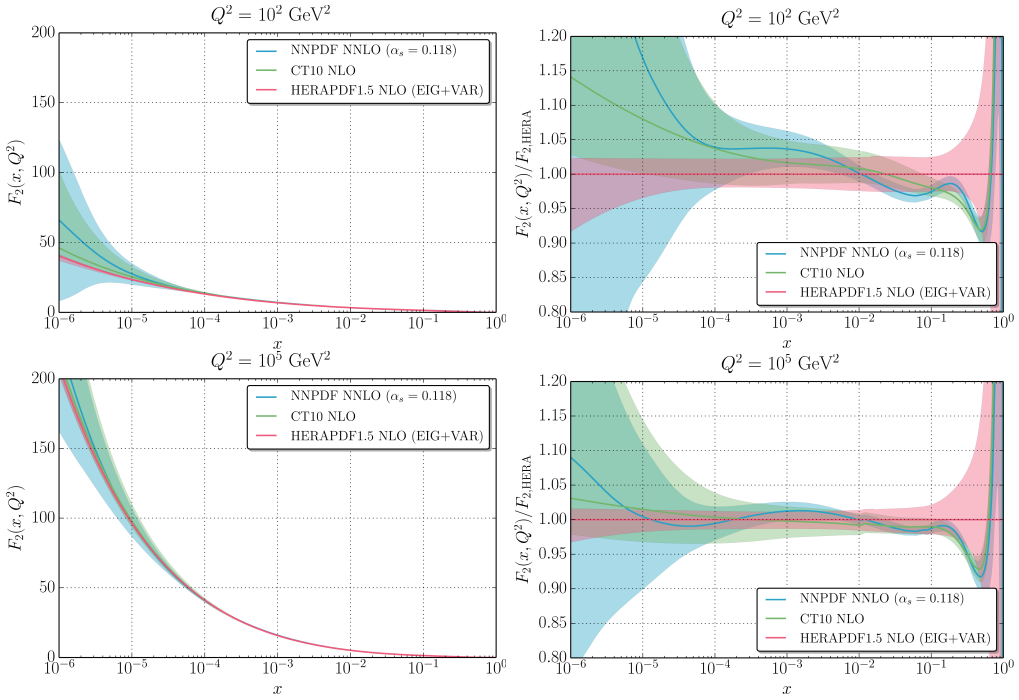

Figure 2.2: $F_2(x, Q^2)$ structure function for $Q^2 = 10^2, 10^5$GeV as a function of x-Bjorken using three PDF group fits: NNPDF, CT10, and HERAPDF. The solid lines in these figures correspond to the best fit value of the structure function, while the color band represents the error band at one sigma. The left panel shows the structure functions, where as the right panel shows the ratio to the HERAPDF fit.

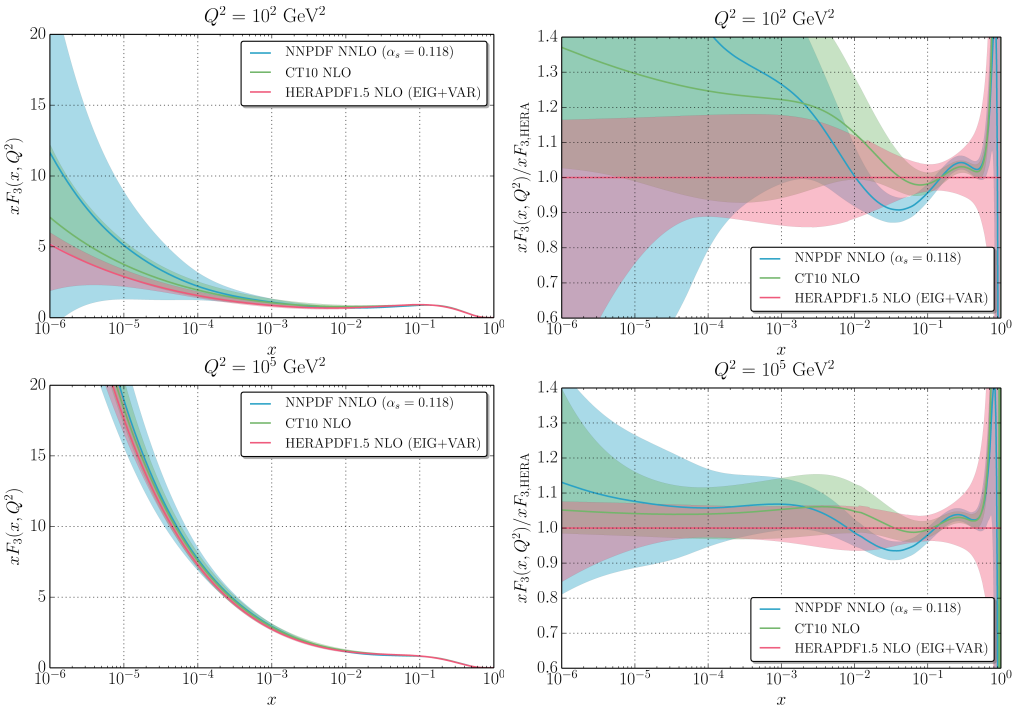

Figure 2.3: $xF_3(x, Q^2)$ structure function for $Q^2 = 10^2, 10^5$GeV as a function of x-Bjorken using three PDF group fits: NNPDF, CT10, and HERAPDF. The solid lines in these figures correspond to the best fit value of the structure function, while the color band represents the one sigma error band. The left panel shows the structure functions, where as the right panel shows the ratio to the HERAPDF fit.

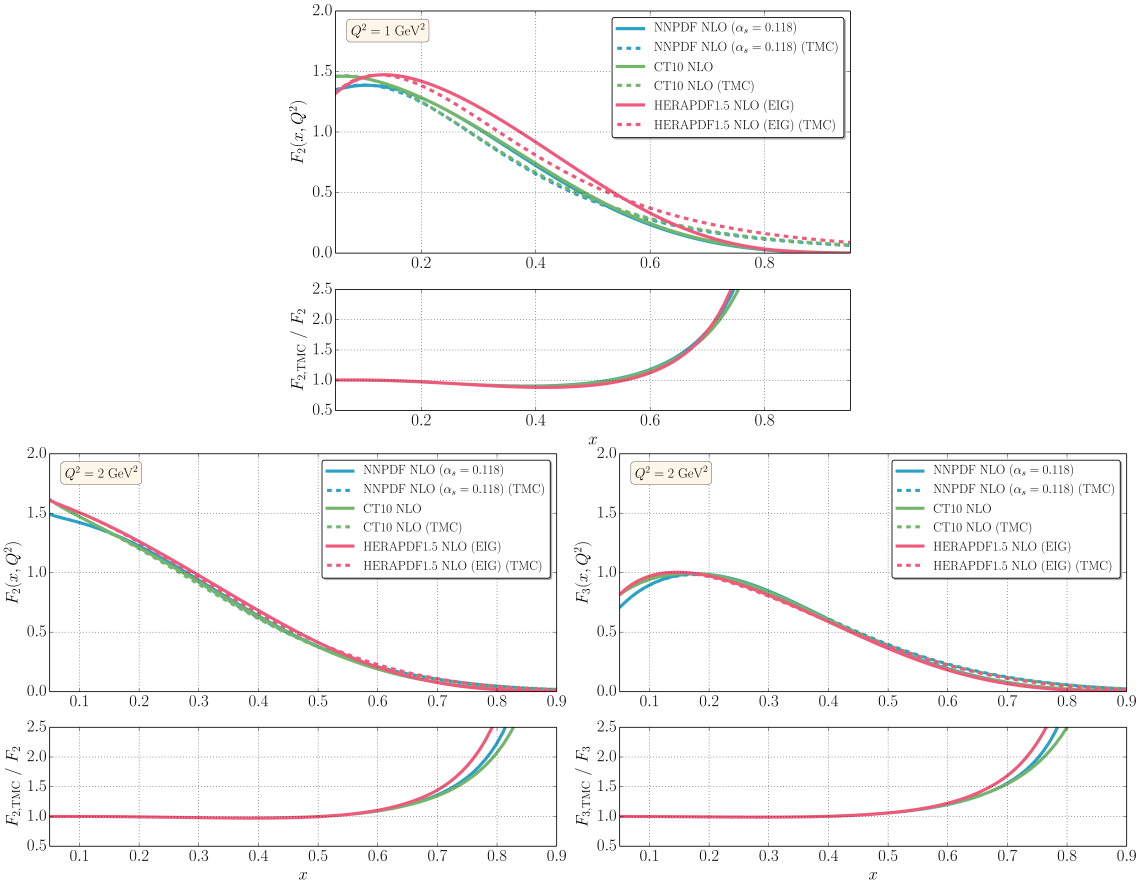

Figure 2.4: Effect of target mass corrections on the cross sections is shown for the F_2 and F_3 structure functions. The solid lines correspond to the structure function without TMC correction and the dashed lines with TMC correction. The upper panel corresponds to $Q^2 = 1\mathrm{GeV}^2$ where as the lower panel correspond to $Q^2 = 2\mathrm{GeV}^2$, thus illustrating that the TMC effect becomes less relevant as one increases Q^2. The panels below the figures show the ratio to the non-TMC corrected structure functions, in which one can see that the effect is more relevant in the forward regime.

The final result of the calculation is the neutrino charge current cross section in the perturbative QCD (pQCD) formalism shown in Figure 2.5. This calculation goes beyond the LO scheme, that has been briefly described here, and is a full NLO calculation performed with the APFEL package [24]. The result is in good agreement with a recent NLO calculation by Cooper-Sarkar et al. [18] with deviations of O(10%) which originate from the updated PDF that now include LHC information. As expected, the cross section increases as a function of the incident neutrino energy and the errors in the IceCube energy range, from different cross section calculations, are no more than $\Delta\sigma_\nu/\sigma_\nu = 15\%$ which implies that predictions of neutrino fluxes from muons are accurate to the same level.

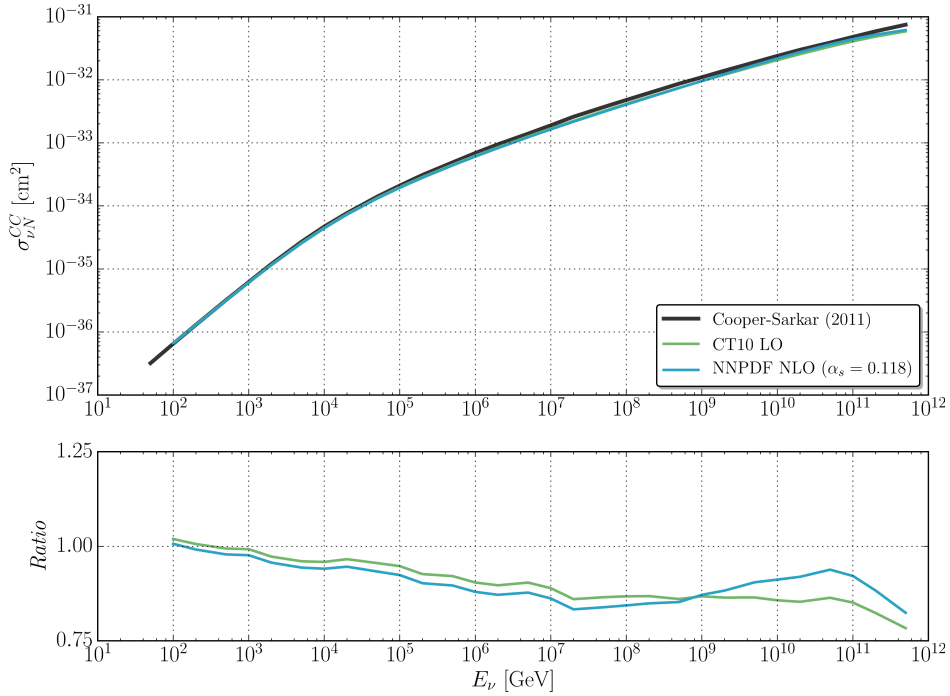

Figure 2.5: Neutrino cross sections calculated using pQCD.

In doing the previous calculation it has been assumed that perturbative QCD is valid to arbitrary small x. However the high-energy behavior of photon, neutrino, and proton cross sections on protons cannot be calculated perturbatively when the fractional momenta x carried by the constituents become vanishingly small [25, 26, 27]. The structure functions develop a $\ln(1/x)$ divergent behavior that results in a violation of unitarity bounds [28]. It has been argued for some time that accelerator and cosmic ray data favor a $\ln^2(s)$ behavior of hadronic cross sections [29]. In fact, a model-independent analytic extrapolation of a $\ln^2(s)$

description of the lower energy data on proton-proton total cross sections correctly anticipated [30, 31, 32] the measurements at the LHC and the Auger cosmic ray observatory [33, 34, 35].

In this section the unified dipole model framework [36, 37, 38, 39, 40, 41] is presented as a description of the behavior of γp, νp, and pp cross sections at high energies and small-x. Perturbative QCD calculations break down at high energy when the proton has an increasing number of partons with small fractional momenta x. In a parton picture, one can simply think of saturation as screening resulting from the fact that the increasing number of small-x partons have to be confined to a high energy proton of finite size. Asymptotically, the proton is a black disk of (mostly) gluons with a radius that increases as $\ln s$.

The $F^{\nu}_{L/T}$ can be evaluated using the dipole formalism with

$$F^{\nu}_{T/L} = \frac{Q^2}{4\pi^2}\sum_q \int_0^1 dz \int d^2\mathbf{r} |\psi^{W,Z}_{T/L,q}(z,\mathbf{r};Q^2)|^2 \sigma_{dip}(x,\mathbf{r}) \ , \tag{2.7}$$

where $\psi^{W,Z}_{T/L,q}(z,\mathbf{r};Q^2)$ corresponds to the wave function for a vector boson (W or Z), of virtual momenta Q^2, to fluctuate into a $q\bar{q}$ pair with fractional longitudinal momentum z and transverse spatial separation r. They are computed from the diagrams in Figure 2.6; in the massless quark limit [42, 43]

$$\begin{aligned}
|\psi^{W}_{T,q}(z,\mathbf{r};Q^2)|^2 &= \frac{2N_c}{\pi^2} Q^2 \left[z\bar{z}\right]\left[z^2+\bar{z}^2\right] K_1^2(\epsilon r), &(2.8)\\
|\psi^{W}_{L,q}(z,\mathbf{r};Q^2)|^2 &= \frac{8N_c}{\pi^2} Q^2 \left[z\bar{z}\right]^2 K_0^2(\epsilon r) \ , &(2.9)\\
|\psi^{Z}_{T,q}(z,\mathbf{r};Q^2)|^2 &= \frac{N_c}{2\pi^2}[L_u^2+L_d^2+R_u^2+R_d^2] \\
&\times \ Q^2 \left[z\bar{z}\right]\left[z^2+\bar{z}^2\right] K_1^2(\epsilon r), &(2.10)\\
|\psi^{Z}_{L,q}(z,\mathbf{r};Q^2)|^2 &= \frac{2N_c}{\pi^2}[L_u^2+L_d^2+R_u^2+R_d^2] \\
&\times \ Q^2 \left[z\bar{z}\right]^2 K_0^2(\epsilon r) \ . &(2.11)
\end{aligned}$$

Following the Henley et al.[44] prescription, the transition from the pQCD parametrization of the structure functions to the high energy dipole formalism is implemented by using Eqns. (2.3) and (2.4) for $x < x_0 = 10^{-5}$ and Eq. (2.7) otherwise.

Our result for the total charged current cross section is shown in Figure 2.7. In this Figure CT10NNLO PDFs [20] and $x_0 = 10^{-5}$ were used. At low energies the calculation agrees with the pQCD calculation, but it incorporates the saturation effect at ultrahigh energies that reduce the neutrino cross section for $E_\nu > 10^9$ GeV. The ultrahigh energy cross section is not very sensitive to the choice of x_0 between $10^{-2} - 10^{-6}$.

The calculation with $x_0 = 10^{-5}$ can be directly compared to the results of Block et al. [45]. As a reference, the Cooper-Sakar et al. [18] calculation without saturation effects is shown; see also [46, 47, 48]. Table 2.1 contains the tabulated charge current cross section for the three calculations shown in Figure 2.7.

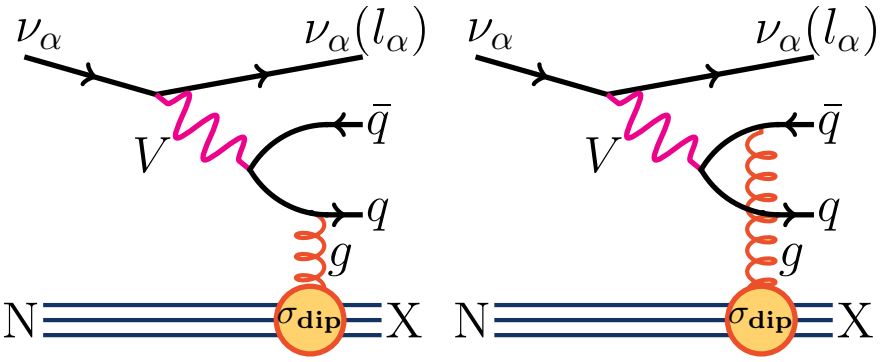

Figure 2.6: Diagram of νp interaction in the dipole picture. In the charge current interaction $V = W^{\pm}$ whereas in the neutral current $V = Z$.

E_ν[GeV]	σ_{CC}[cm^2]		
	Sarkar et al.	Block et al.	**This work**
1×10^8	4.8×10^{-33}	4.31×10^{-33}	4.88×10^{-33}
2×10^8	6.2×10^{-33}	5.46×10^{-33}	6.15×10^{-33}
5×10^8	8.7×10^{-33}	7.25×10^{-33}	8.07×10^{-33}
1×10^9	1.1×10^{-32}	8.87×10^{-33}	9.71×10^{-33}
2×10^9	1.4×10^{-32}	1.07×10^{-32}	1.15×10^{-32}
5×10^9	1.9×10^{-32}	1.36×10^{-32}	1.42×10^{-32}
1×10^{10}	2.4×10^{-32}	1.61×10^{-32}	1.65×10^{-32}
2×10^{10}	3.0×10^{-32}	1.90×10^{-32}	1.90×10^{-32}
5×10^{10}	3.9×10^{-32}	2.33×10^{-32}	2.28×10^{-32}
1×10^{11}	4.8×10^{-32}	2.69×10^{-32}	2.60×10^{-32}
2×10^{11}	5.9×10^{-32}	3.10×10^{-32}	2.96×10^{-32}
5×10^{11}	7.5×10^{-32}	3.69×10^{-32}	3.49×10^{-32}

Table 2.1: Neutrino charge current cross section values for Sarkar et. al [18] pQCD calculation, Block et al. [45], and this work.

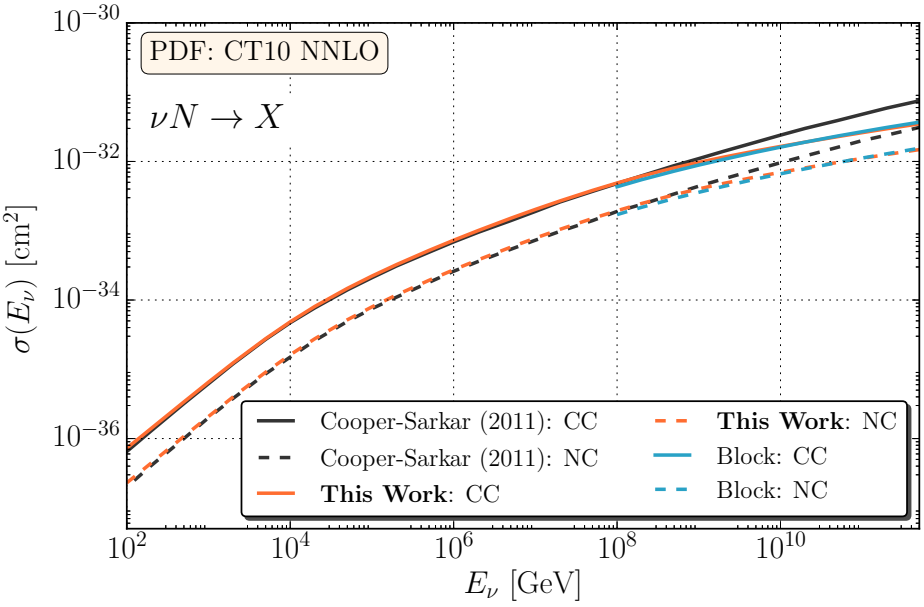

Figure 2.7: Neutrino cross sections calculated using HERAPDF NNLO PDFs [21] and our dipole model (orange). For comparison, a recent calculation done in pQCD by Cooper-Sakar et al. [18] (black), which does not incorporate saturation effects and a similar calculation by Block et al. [45] are showned. The solid lines represent the charge current cross sections, whereas the dashed line portray the neutral current cross section.

2.2 Neutrino oscillations

During the last decades a plethora of evidence that neutrinos change flavor as they propagate macroscopic distances due to the nonalignment of their mass and flavor eigenstates has accumulated from solar, atmospheric, accelerator, and reactor experiments [49, 50]. Thanks to these remarkable experimental results and related theoretical calculations the *neutrino-mass induced flavor oscillation paradigm* [51, 52, 53, 54, 55, 56] has been firmly established and the three mixing angles that parametrize the lepton mixing matrix, together with the two square mass differences have been measured to good precision [57]. Furthermore, it is the task of on-going and future experiments to determine the neutrino mass ordering and the Dirac CP-violating phase [58].

Even though most of the data can be explained in the standard three neutrino framework some puzzling anomalies still remain [59, 60, 61]. These may be explained by introducing new neutrino states, often referred to as light sterile neutrinos [62, 63, 64]; which will be described in detail on 4.1. Moreover, other new physics scenarios such as the possibility of non standard interactions [65, 66] have also been considered and are discussed in 4.2. Also the interplay between cosmology and neutrino oscillation has been widely studied in

the literature as well as a playground for new physics scenarios [67, 68, 69]. In general, neutrino physics constitutes an excellent proof for fundamental physics [58] as further explored in 4.3. In this section only the standard paradigm will be considered.

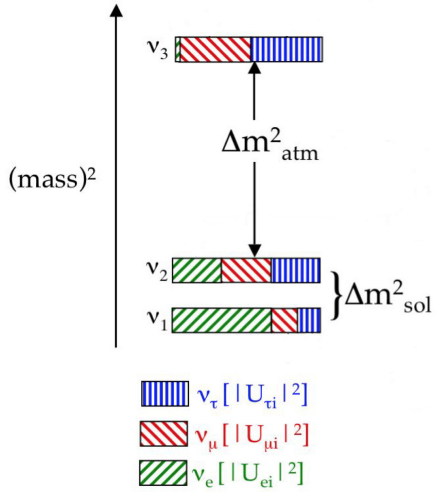

Figure 2.8: Diagram of active neutrinos mass splittings and mixings. The normal ordering is presented ($\Delta m^2_{atm} > 0$) where the colors in each of the bars represent the approximate flavor composition of each of the mass eigenstates.

The state of the neutrino ensemble can be represented using the density matrix formalism, e.g. in the weak-interaction flavor eigenstate basis $\{|\nu_\alpha\rangle\}$ it can be written as

$$\rho = \sum_\alpha \phi_\alpha |\nu_\alpha\rangle\langle\nu_\alpha| \ , \tag{2.12}$$

where ϕ_α specifies the flavor content. Another important basis are the mass eigenstates $\{|\nu_i\rangle\}$, which are the eigenstate of the propagation in vacuum, and are related to the former by

$$|\nu_\alpha\rangle = \sum_i U_{\alpha i} |\nu_i\rangle \ , \tag{2.13}$$

where U is the unitary lepton mixing matrix. An illustration of the relationship between the mass and flavor basis in Figure 2.8. It is customary to parametrize the mixing matrix U with mixing angles, $\{\theta_{ij}\}$, and CP

phases, $\{\delta_{ij}\}$; for example when considering the standard three flavor paradigm the following parametrization is often used

$$U = \begin{pmatrix} c_{12}c_{13} & s_{12}c_{13} & s_{13}e^{-i\delta_{13}} \\ -s_{12}c_{23} - c_{12}s_{23}s_{13}e^{i\delta_{13}} & c_{12}c_{23} - s_{12}s_{23}s_{13}e^{i\delta_{13}} & s_{23}c_{13} \\ s_{12}s_{23} - c_{12}c_{23}s_{13}e^{i\delta_{13}} & -c_{12}s_{23} - s_{12}c_{23}s_{13}e^{i\delta_{13}} & c_{23}c_{13} \end{pmatrix}, \tag{2.14}$$

where $c_{ij} = \cos\theta_{ij}$, $s_{ij} = \sin\theta_{ij}$. In this work, when the three flavor scenario is considered the aforementioned parametrization will be used with values from [57] and when more flavors are considered the prescription given in [70] will be implemented. Furthermore, the neutrino ensemble evolution is described by the following quantum Von Neumann equation

$$\frac{\partial\rho(E)}{\partial x} = -i[H(E,x), \rho(E)] \ . \tag{2.15}$$

In general the Hamiltonian, H, can always be split into a time dependent and independent parts. In particular, for neutrino oscillations the following splitting is convenient

$$H(E,x) = H_0(E) + H_1(E,x) \tag{2.16a}$$

$$H_0(E) = \frac{1}{2E}\text{diag}(0, \Delta m^2_{21}, \Delta m^2_{31}, ..., \Delta m^2_{i1}, ..., \Delta m^2_{n1}) \tag{2.16b}$$

$$H_1(E,x) = \sqrt{2}G_F U^\dagger \text{diag}(N_e(x) - N_{nuc}(x)/2, -N_{nuc}(x)/2, -N_{nuc}(x)/2, 0, ..., 0)U \tag{2.16c}$$

where n is the number of neutrino flavors, G_F is the Fermi constant, Δm^2_{i1} are the neutrino mass splittings, and, finally, $N_e(x)$ and $N_{nuc}(x)$ are the electron and nucleon number densities along the neutrino path. On writing these equations the convention that the first three flavor eigenstates corresponds to ν_e, ν_μ, and ν_τ has been used, while the rest are assumed to be sterile neutrinos. Furthermore, H_0 arrises from the neutrino kinetic term, where as H_1 incorporates the matter potential, i.e. coherent forward scattering interactions [71, 72, 73]. Given this splitting it is convenient to change to the so called interaction picture, generated by H_0, defined by the following transformation for a given operator O

$$O \to \bar{O}(x) = \exp(-iH_0x)O\exp(iH_0x), \tag{2.17}$$

and then the evolution equation is

$$\frac{\partial\bar{\rho}(E)}{\partial x} = -i[\bar{H}_1(E,x), \bar{\rho}(E)] \ . \tag{2.18}$$

It is interesting to consider the case of vacuum only propagation, i.e. $H_1 = 0$, in which the oscillation probability can be solved analytically. Given the Hamiltonian in Eq.(2.16) and solving the evolution of an initial flavor state $|\nu_\alpha\rangle$ over a distance L, the probability of measuring a flavor state $|\nu_\beta\rangle$ is

$$\begin{aligned} P_{\nu_\alpha\to\nu_\beta}(L,E) &= \delta_{\alpha\beta} - 4\sum_{i>j} Re(U^*_{\alpha i}U_{\beta i}U_{\alpha j}U^*_{\beta j})\sin^2\left(\frac{\Delta_{ij}}{2}L\right) \\ &\quad +2\sum_{i>j} Im(U^*_{\alpha i}U_{\beta i}U_{\alpha j}U^*_{\beta j})\sin\left(\Delta_{ij}L\right), \end{aligned} \tag{2.19}$$

where $\Delta_{ij} = \Delta_i - \Delta_j$ are the Hamiltonian eigenvalue difference, which in this case correspond to $\Delta m^2_{i,j}/(2E)$. Further simplification can be obtained in the two neutrino scenario, in which the oscillation probability is

$$P_{\nu_\alpha\to\nu_\beta}(L,E) = \delta_{\alpha\beta} - \sin^2 2\theta \sin^2\left(\frac{\Delta m^2 L}{4E}\right) \ . \tag{2.20}$$

where θ is the mixing angle that parametrizes mixing angle between the two flavor and mass eigenstates and Δm^2 is the square mass difference between the two levels considered. In Figure 2.9 the neutrino survival probability ($\alpha = \beta$) for $\sin^2\theta = 1$ and $\Delta m^2 = \Delta m^2_{atm} = 2.47\times10^{-3}\text{eV}^2$ has been plotted.

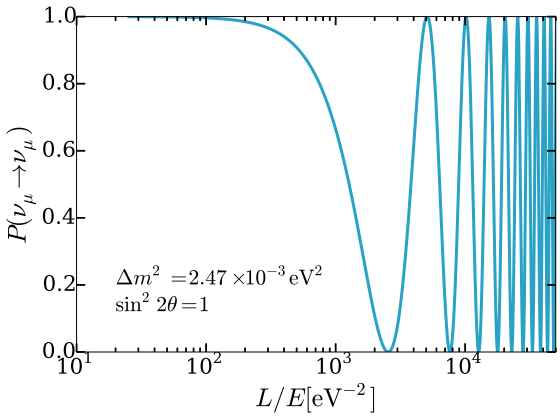

Figure 2.9: Simple two neutrino oscillations illustrates the three regimes that neutrino oscillation experiments can encounter. If $\Delta m^2\frac{L}{E} \ll 1$ no oscillations, then if $\Delta m^2\frac{L}{E} \sim 1$ first oscillations, and finally $\Delta m^2\frac{L}{E} \gg 1$ fast oscillations.

It is clear from Equation 2.20 that the mixing angle controls the amplitude of the oscillation and Δm^2 the frequency with the maximum oscillation length $L_n = 2(2n+1)\pi E/\Delta m^2$. The oscillation phenomenology can be classified in three distinct categories. First, when $\Delta m^2 L/E \ll 1$, then $P_{\nu_\alpha \to \nu_\beta}(L, E) \approx \delta_{\alpha\beta}$ and no oscillations are observed. Second, when $\Delta m^2 L/E \sim 1$, then the oscillations are observed and can be resolved by the experiment. Finally, when $\Delta m^2 L/E \gg 1$ and one encounters a fast oscillation regime that cannot be experimentally resolved and the oscillation probability averages out to $P_{\nu_\alpha \to \nu_\beta}(L, E) \approx \delta_{\alpha\beta} - \frac{1}{2}\sin^2 2\theta$. The transition between these regimes depends on the particular experiment, e.g. the experiment statistics, systematics, and background will set the minimum oscillation amplitude that can be measured setting the transition between seing no oscillations and observing disapperance (appearance). On the other hand, for example, the energy resolution will set the transition between *fast* oscillations and *slow* oscillations.

In Figure 2.10 the neutrino oscillation experiments performed in the last decades have been plotted as a function of the neutrino energy and baseline. The energy range extents from a few MeV to hundreds of TeV and the baselines range from tenths of meters to the Earth diameter. The black dashed line corresponds to the first oscillation maximum given by the solar scale, $L_\odot$, and the black dashed-dotted line to the atmospheric scale, L_{atm}. Solar neutrino experiments and medium baseline reactor experiments such a KamLAND have measured solar neutrino oscillation given precise measurements of Δm^2_{21} and θ_{12}. On the other hand, atmospheric neutrino experiments such as Super-Kamiokande and IceCube-DeepCore have observed oscillations on atmospheric neutrinos. This oscillation scale, has being further confirmed by long baseline oscillations experiments, e.g. MINOS and T2K. These experiments have contributed to the measurement of $|\Delta m^2_{32}|$ and θ_{23}. More recently, reactor experiments such as Daya Bay and RENO, have measure the only remaining mixing angle, θ_{13}. The sign of the atmospheric mass-square difference, which determines the neutrino ordering, is still unknown; as well as the value of the CP-phase. It is interesting to note that the experiments colored in pink have claimed evidence of neutrino oscillation, which would point to a new oscillation scale. If these anomalies were due to a sterile neutrino, i.e. a line in Figure 2.10, then it should be observable in IceCube-DeepCore. Moreover, IceCube-DeepCore is in a previously uncharted regime in the L-E plane, since previous high energy experiments were only possible at short baselines. In Chapter 4 we will return to this discussion and figure by illustrating different new physics scenarios.

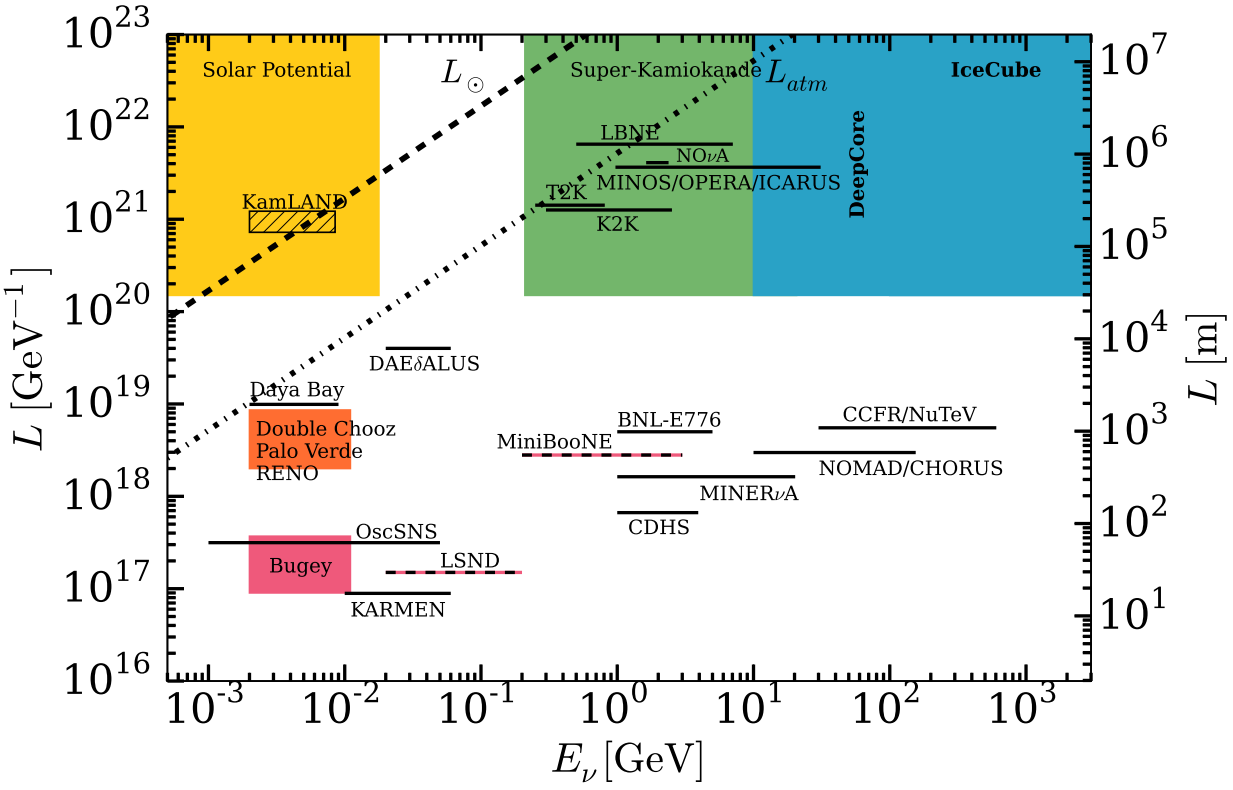

Figure 2.10: Summary of neutrino oscillation experiments performed in the last decades as a function of their baseline, L, and the energy range E_ν. The dashed lined corresponds to the first oscillation maximum given by the so called solar mass splitting $\Delta m^2_\odot$, where the dashed-dotted line is given by the atmospheric mass splitting Δm^2_{atm}. Experiments which incorporate a large range in mass an energy, e.g. Super-Kamiokande, are shown as colored regions. Finally, experiments with evidence for an extra oscillation scale are colored pink.

2.3 Neutrino propagation: interactions and oscillations

So far only neutrino oscillation and matter effects through coherent interactions have been incorporated, but we will consider an extended formalism in order to treat non-coherent interactions and collective neutrino behavior. This problem has been extensively discussed in the literature, in particular in [74, 75, 76] and [77, 78, 79], for definiteness the formalism given in [80] will be followed. To simplify the notation, in what follows the *bar* symbol – introduced in Eq. 2.17 – will be suppressed and all operators, unless specified, are on the interaction basis generated by H_0. The formalism shown here aims to calculate the neutrino density matrix $\rho(E,t)$ at every time and energy given some initial condition $\rho_0(E)$, in what follows independent variables t and x will be used interchangeably, since, for the cases of interest, the neutrinos are always relativistic. In principle the problem can be solved continuously in energy and time, but such analytical treatment is only possible in trivial contexts, e.g. vacuum; in practice discretization in time and energy need to be introduced, for which the notion of *energy nodes* and correspondingly label the neutrino state $\rho_i(t)$ needs to be introduced: the neutrino state at an energy E_i and time t. Given these considerations the neutrino ensemble evolution is given by

$$\frac{\partial \rho_i}{\partial x} = -i[H_1(E_i,x),\rho_i] - \{\Gamma(E_i,x),\rho_i\} + F(\Omega,L;E_i,x) \tag{2.21a}$$

$$\frac{\partial l_i}{\partial x} = -\gamma(E_i,x)l_i + G(\Omega;E_i,x) \tag{2.21b}$$

where E_i is the energy corresponding to the i-node and we have introduced $\Omega = \{\rho_i | i = 1,...,m\}$ and $L = \{l_i^\alpha |\ \alpha = \{e,\mu,\tau\}, i = 1,...,m\}$ the neutrino and lepton ensembles respectively with m the number of energy nodes. Γ incorporates the effect of attenuation due to non-coherent interactions in neutrinos. The F term contains the interactions between the neutrino ensemble and the leptons, similarly the G term incorporates the effects of neutrinos into leptons. In most scenarios the e and μ leptons lose energy too fast to contribute significantly into the latter neutrino flux, thus we shall only consider the τ leptons since they have a very short decay time [81]. Thus, we write the right hand side terms of Eq. (2.21) explicitly as follows

$$\Gamma(E,x) = \sum_{\alpha} \frac{\Pi_\alpha}{2\lambda^\alpha_{\text{total}}} \tag{2.22a}$$

$$\gamma(E,x) = -\frac{1}{\lambda^\tau_{\text{dec}}(E,x)} \tag{2.22b}$$

$$\begin{aligned} F(\Omega,L;E,x) = &\int_E^\infty d\tilde{E} \sum_\alpha \frac{1}{2} \left\{ \frac{\Pi_\alpha}{\lambda^\alpha_{\text{NC}}(\tilde{E},x)}, \rho(\tilde{E},x) \right\} \frac{\partial N_{\text{NC}}(\tilde{E},E)}{\partial E} \\ &+ \int_E^\infty d\tilde{E} \frac{1}{\lambda^\tau(\tilde{E},x)} \tau(\tilde{E},x) \frac{\partial N_{\text{dec}}(\tilde{E},E)}{\partial E} \Pi_\tau \\ &+ \text{Br}_{\text{lep}} \int_E^\infty d\tilde{E} \frac{1}{\lambda^\tau(\tilde{E},x)} \tilde{\tau}(\tilde{E},x) \frac{\partial \tilde{N}_{\text{dec}}(\tilde{E},E)}{\partial E} \Pi_\tau \end{aligned} \tag{2.22c}$$

$$G(\Omega;E,x) = \int_E^\infty d\tilde{E} \frac{1}{\lambda^\tau_{CC}(\tilde{E},x)} \text{Tr}\left[\Pi_\tau, \rho(\tilde{E},x)\right] \frac{\partial N_{\text{CC}}(\tilde{E},E)}{\partial E} \tag{2.22d}$$

where we have introduced the flavor projectors Π_α and the sums run over the active neutrino flavors. Furthermore, λ_{CC}, λ_{NC}, and $\lambda_{\text{total}} = \lambda_{\text{CC}} + \lambda_{\text{NC}}$ are the charge, neutral and total neutrino interactions lengths respectively. Moreover, $\frac{\partial N}{\partial E}$ represents the outgoing neutrino (or τ lepton) spectral distribution for charge, neutral neutrino interactions and τ decay. Finally, λ^τ_{dec} is the τ decay length, which is assumed to be much smaller than the relevant neutrino oscillation and interaction scales. In order to compute the integrals that appear in Eq. 2.22 we use a numerical finite difference algorithm.

In Figure 2.11 we have plotted the transfer function for ν_μ and $\bar{\nu}_\mu$ calculated using Equation 2.22 as a function of the zenith angle and neutrino energy at the end of the trajectory. Two important features can be observed in these plots. First, at energies of $O(100\text{GeV})$ the ν_μ transfer function is dominated by the $P(\nu_\mu \to \nu_\mu)$ neutrino disappearance which at $\cos\theta_z \sim -1$ is $\sim 10\%$. Second ,at high energies and high $\cos\theta_z$ (Earth core crossing trajectories) the Earth is opaque to neutrinos; regarding this also note that the antineutrino Earth opacity is slightly less than the neutrino, this is just due to the antineutrino cross section being smaller than the neutrino one.

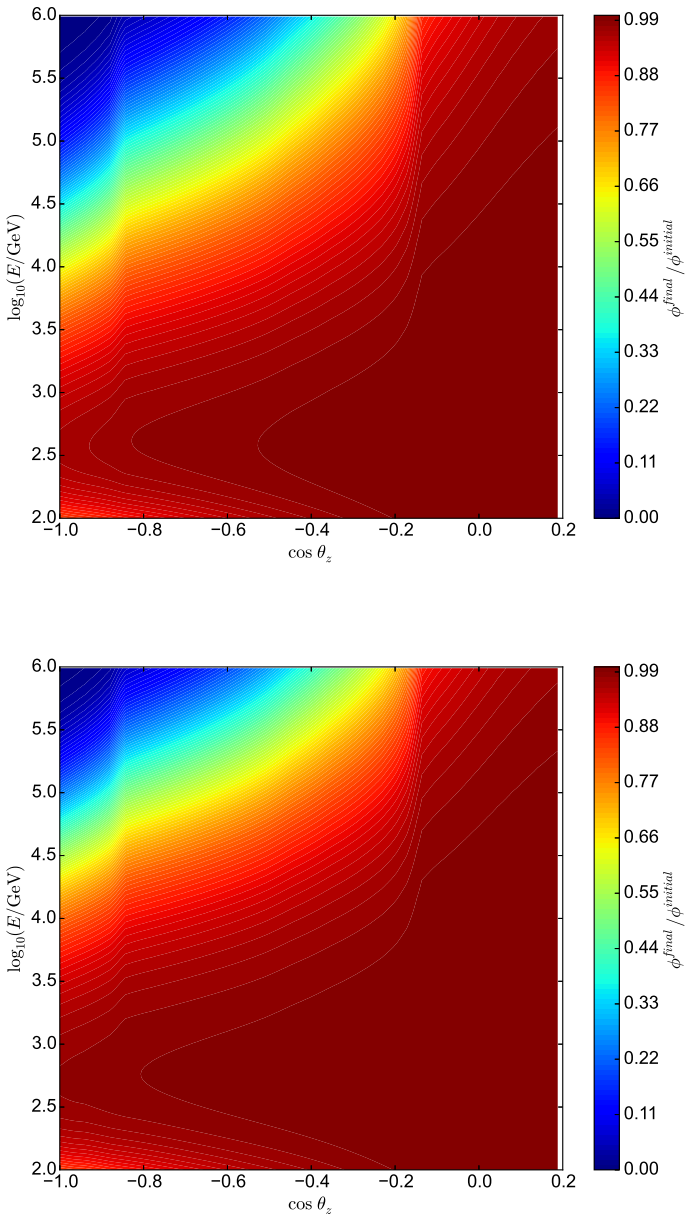

Figure 2.11: Muon neutrino Earth transfer function for neutrinos (top) and antineutrinos (bottom) calculated using Eqs. 2.22 as a function of zenith angle and neutrino energy; the color scale shows the ratio of final flux (ϕ^{final}) to initial flux ($\phi^{initial}$). In most of the energy range and baseline the transfer function is ~ 1, i.e. the initial flux is unaltered. Effects of Earth absorption at high energies and oscillation at low energies can be seen for $\cos\theta_z \sim -1$.

Chapter 3

Atmospheric Neutrinos

"Esas ambigüedades, redundancias y deficiencias recuerdan las que el doctor Franz Kuhn atribuye a cierta enciclopedia china que se titula 'Emporio celestial de conocimientos benévolos'. En sus remotas páginas está escrito que los animales se dividen en a) pertenecientes al Emperador, b) embalsamados, c) amaestrados, d) lechones, e) sirenas, f) fabulosos, g) perros sueltos, h) incluidos en esta clasificación, i) que se agitan como locos, j) innumerables, k) dibujados con un pincel finísimo de pelo de camello, l) etcétera, m) que acaban de romper el jarrón, n) que de lejos parecen moscas."

— Jorge Luis Borges, Otras inquisiciones.[3]

When cosmic rays interact in the upper atmosphere they produce hadronic showers which develop over several kilometers in the atmosphere. These showers are meson rich, in particular, they contain large amounts of light mesons such as pions and kaons. As the pions and kaons cascade down there is an interplay between their energy loss and their decay length. Light meson decay produces the bulk of atmospheric neutrinos and muons, e.g. *via* $\pi \to \mu + \nu_\mu$, the neutrinos arising from light meson decay make up the *conventional* component. This process is nicely illustrated in Figure 3.1. Neutrinos from higher than 10^5GeV are increasingly produced from charmed meson decay in the atmosphere. For those mesons the decay length is much shorter than the interaction length up to 10^7GeV, so no competition between decay and interaction exist,

[5] These ambiguities, redundancies, and deficiencies remind us of those which doctor Franz Kuhn attributes to a certain Chinese encyclopaedia entitled 'Celestial Empire of benevolent Knowledge'. In its remote pages it is written that the animals are divided into: (a) belonging to the emperor, (b) embalmed, (c) tame, (d) sucking pigs, (e) sirens, (f) fabulous, (g) stray dogs, (h) included in the present classification, (i) frenzied, (j) innumerable, (k) drawn with a very fine camelhair brush, (l) et cetera, (m) having just broken the water pitcher, (n) that from a long way off look like flies.

unlike in the conventional component. Thus, to good approximation, charmed meson decay instantly, and the neutrino product of their decay conform the so called *prompt* neutrino flux. The different contributions can be seen in Figure 3.2 from Feydinitch et al. [6].

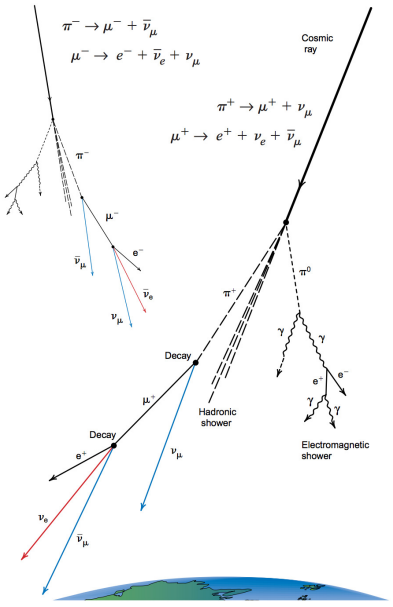

Figure 3.1: Diagram of a shower.

Furthermore, $\pi^\pm$ has $\Gamma(e^\pm {}^{(-)}\!\nu_e)/\Gamma(\mu^\pm {}^{(-)}\!\nu_\mu) = O(10^{-4})$, while for $K^\pm$ the corresponding fraction is $\Gamma(e^\pm {}^{(-)}\!\nu_e X)/\Gamma(\mu^\pm {}^{(-)}\!\nu_\mu) = O(10^{-2})$ [2]. Which means that the conventional atmospheric flux is dominated by the ν_μ neutrinos. The prompt component, on the other hand, is dominated by the $D^\pm$ mesons for which $\Gamma(e^\pm {}^{(-)}\!\nu_e X)/\Gamma(\mu^\pm {}^{(-)}\!\nu_\mu X) = O(1)$ and can decay to ν_τ with a branching ratio $\Gamma(\tau^\pm {}^{(-)}\!\nu_\tau) < 1.2 \times 10^{-3}$ [2]. Thus, as can be seen in Figure 3.2, at low energies, the atmospheric flux is dominated by the conventional ν_μ and at the highest energies by the prompt component which has almost equal ν_μ and ν_e; finally the ν_τ content is highly suppressed.

From the previous discussion it follows that prediction of the atmospheric neutrino fluxes requires three main ingredients: incident cosmic ray spectrum, hadronic interaction models, and the atmospheric density profile on which the shower develops. The initial cosmic ray spectrum is illustrated in Figure 3.3 and for proton energies less than 10^6GeV, it can be approximated by a power law $E^{-\gamma}$ with $\gamma \sim 2.75$. It is important to note that there is an approximate linear relation between the mean cosmic ray energy that produces a shower and the resulting neutrino mean energy, such that $< E_\nu > \sim < E_p > /10$, see [4]. Since special attention will be placed to the conventional component due to its larger statistics. This implies that details

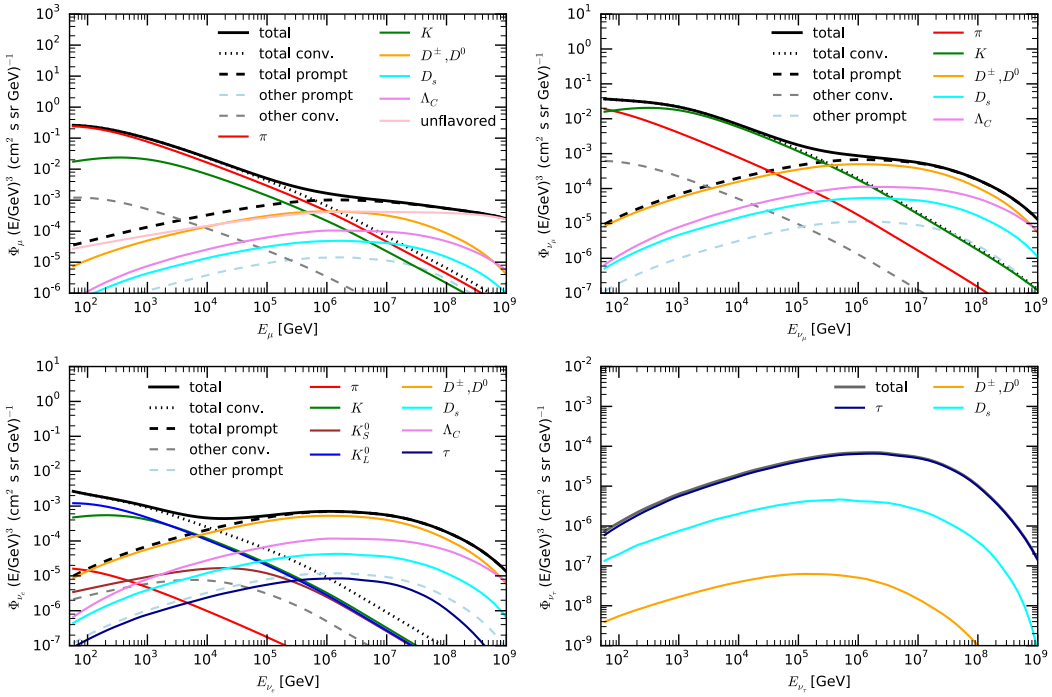

Figure 3.2: Partial contribution of intermediate particles to the flux of atmospheric muons $\mu^+ + \mu^-$ (top left), muon neutrinos $\nu_\mu + \bar{\nu}_\mu$ (top right), electron neutrinos $\nu_e + \bar{\nu}_e$ (bottom left) and tau neutrinos $\nu_\tau + \bar{\nu}_\tau$ (bottom right). The primary spectrum is Thunman et al. (TIG) [82] and the interaction model is SIBYLL-2.3 RC1.

of the cosmic rays spectrum above 10^6GeV are not relevant to the search of new physics in the conventional spectrum.

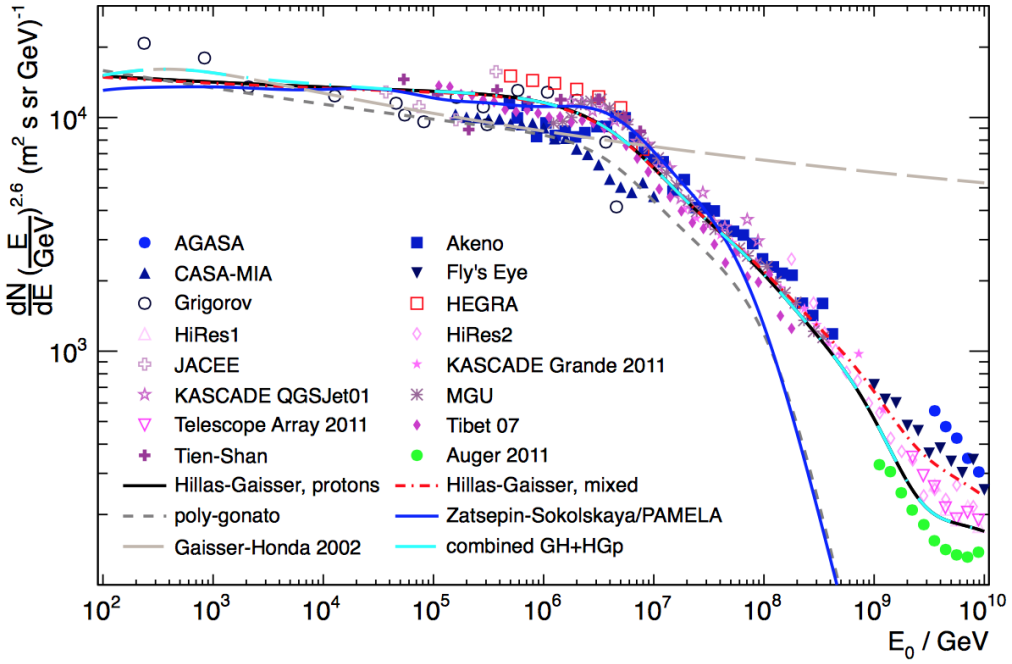

Figure 3.3: Cosmic ray fluxes models and data from [5].

For the work on this thesis, three cosmic ray spectrum models will be considered: the Honda-Gaisser model with Gaisser-Hillas H3a correction [83], the Zatespkin Sokolskaya [84], and the Polygonato model [85]; the latter two are disfavored by the data at high energies – as can be see in Figure 3.3 –, but are in reasonable agreement in the region of interest $E_p < 10^5$GeV. For hadronic models the following will be used: QGSJET-II-4 [86] and SIBYILL2.3 [87]. Finally, for the atmospheric density we will use data from the NASA AIRS satellite [88]. AIRS orbits the Earth in a heliosynchronous orbit and measures the temperature profile of the atmosphere. These temperature profiles are converted to density profiles, using the ideal gas law. Which are a function of atmospheric depth, latitude, longitude, and time. We use the package MCeq [89] to solve the cascade equations under these assumptions.

In Figure 3.4 the result of this calculation is shown as a function of energy for neutrinos and antineutrinos for two zenith values in which yearly average has been performed when considering different combinations of cosmic ray and interaction models. For comparison the HKKM model [90, 91] (a.k.a. the *Honda model*) is

also shown as solid black line. It can be seen that the different models differ by no more than O(10%) from the HKKM model.

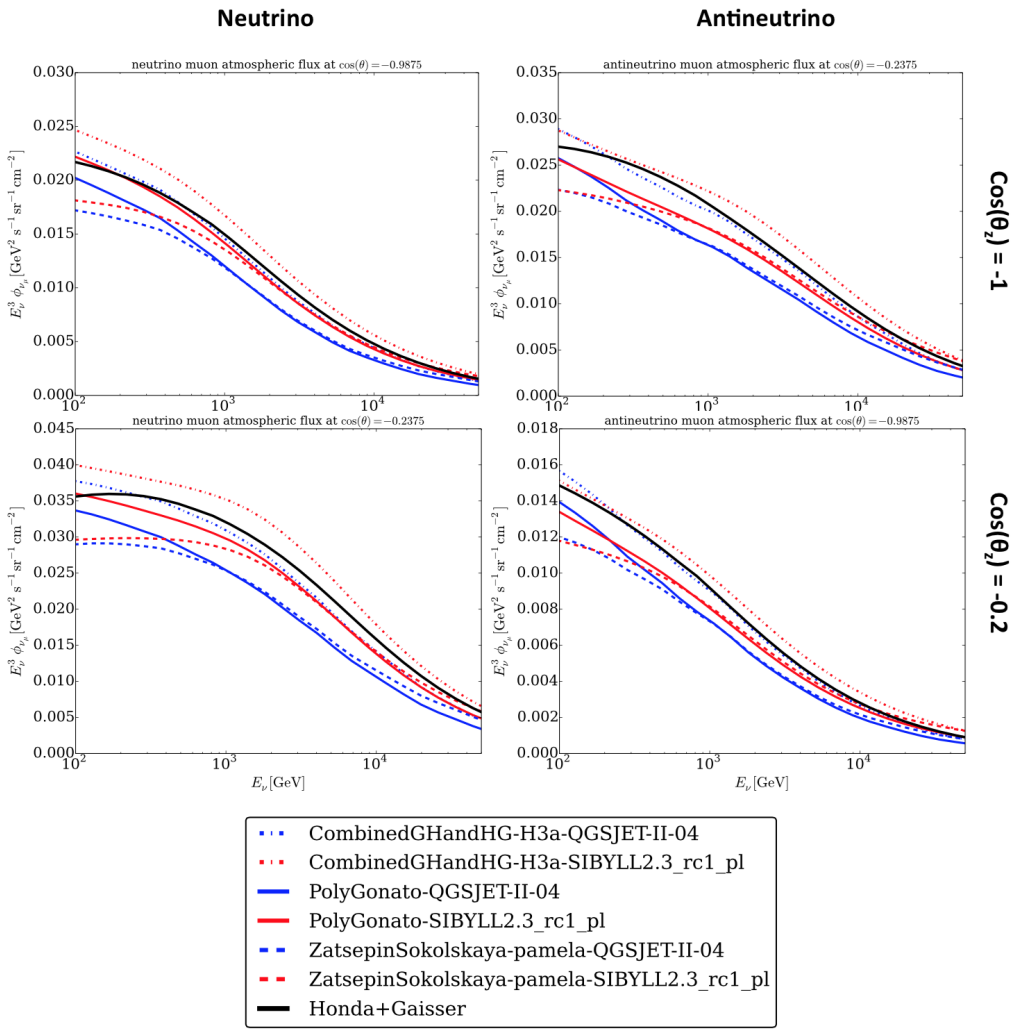

Figure 3.4: Atmospheric neutrino models.

Furthermore, in Figure 3.5 the effect of seasonal density variation as measured by the AIRS satellite is shown. It is important to note that the yearly average with respect to a calculation using the US-standard [92] does not deviate in more than 10% from the exact monthly calculation.

So far only the *conventional* component has been discussed, lets briefly talk about the *prompt* contribution. Estimation of the prompt flux has an increased difficulty since cosmic ray energies greater than 10^6GeV need to be considered, where features like the cosmic ray knee and cosmic ray composition – which are not well known – appear, see Figure 3.3. Furthermore, even though the total charmed production cross section has

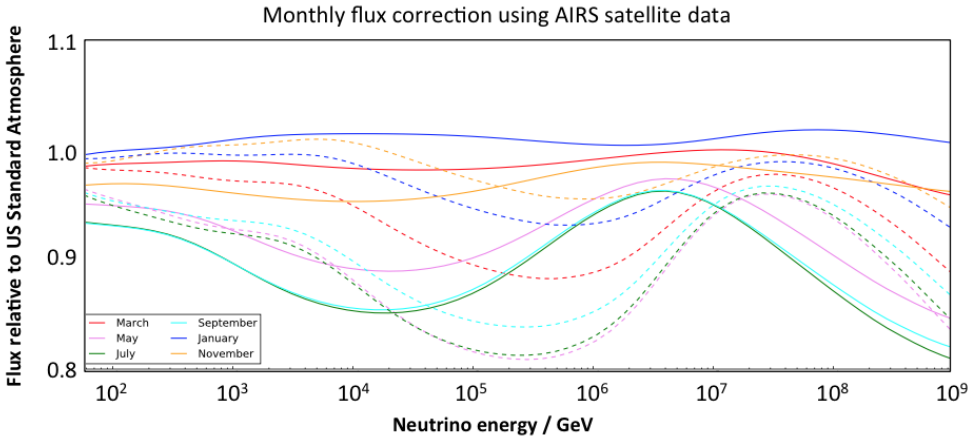

Figure 3.5: Atmospheric neutrino yearly variation due to the change in atmospheric density. The solid lines correspond to vertical neutrinos and the dashed to horizontal ones. The region of interest of the this work is between 10^3 to 10^4 GeV.

been measured in colliders, the differential cross section in the forward region still has significant uncertainties, due to the fact that very small x region is proved.

The dipole formalism, that was introduced in Sec. 2.1, can be used to estimate the charm production cross section in this regime. In the dipole model, the proton-proton to charm production cross section is given by [93, 37]

$$\begin{aligned} \sigma_{pp\to q\bar{q}+X} &= 2\int_0^{-\ln(2m_q/\sqrt{s})} dy\; x_1 g(x_1,\mu) \\ &\times \sigma_{gN\to q\bar{q}+X}(x_2;Q^2)\;, \end{aligned} \tag{3.1}$$

where $g(x_1,\mu)$ is the gluon distribution function at the scale μ, and $x_{1,2}$ satisfy $x_1 x_2 \simeq (2m_q)^2/s$ with

$$x_1 \simeq \frac{2m_q}{\sqrt{s}}\exp(y) \tag{3.2}$$

$$x_2 \simeq \frac{2m_q}{\sqrt{s}}\exp(-y); \tag{3.3}$$

see Figure 3.6. Here $\sigma_{gN\to q\bar{q}+X}$ is the partonic cross section, which in the dipole picture is given by

$$\begin{aligned} \sigma_{gN\to q\bar{q}+X}(x_2;Q^2) &= \int dz\; d^2\mathbf{r}\; |\psi^g_{T,q}(z,\mathbf{r};Q^2)|^2 \\ &\times \sigma_{gq\bar{q}}(x_2,z,\mathbf{r}) \end{aligned} \tag{3.4}$$

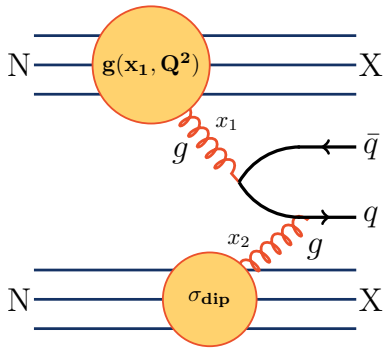

Figure 3.6: Diagram of $pp \to q\bar{q}X$ for one dipole interaction topology, the remainder are shown in Figure 3.7 . In this picture the gluon from the projectile proton has fractional parton momenta x_1 and it is modeled through PDF, while the target proton gluon has fractional parton momenta $x_2 \ll 1$ and it is modeled through a dipole interaction.

The partonic cross section is directly related to the dipole cross section [93, 37]:

$$\begin{aligned} \hat{\sigma}_{gq\bar{q}}(x_2, z, \mathbf{r}) &= \frac{9}{8}\left[\sigma_{dip}(x_2, z\mathbf{r}) + \sigma_{dip}(x_2, \bar{z}\mathbf{r})\right] \\ &- \frac{1}{8}\sigma_{dip}(x_2, \mathbf{r}) \end{aligned} \tag{3.5}$$

where the different terms correspond to the superposition of the diagrams shown in Figure 3.7.

The gluon wave function is related to the photon wave function, given in Eq. (3.6) by [94]

$$|\psi^{\gamma}_{T,q}|^2 = e_q^2 N_c \frac{\alpha_{em}}{2\pi^2}\left[(z^2 + \bar{z}^2)\epsilon^2 K_1^2(\epsilon r) + m_q^2 K_0^2(\epsilon r)\right], \tag{3.6}$$

$$|\psi^{g}_{T,q}(z, \mathbf{r}; Q^2)|^2 = \frac{\alpha_s}{N_c \alpha_{em}} |\psi^{\gamma}_{T,q}(z, \mathbf{r}; Q^2)|^2, \tag{3.7}$$

where e_q is the quark charge, N_c the number of colors, $\epsilon^2 = z\bar{z}Q^2 + m_q^2$, $\bar{z} = 1 - z$, and K_0 and K_1 the modified Bessel functions. In Figure 3.8 the total proton-proton charm production cross section has been

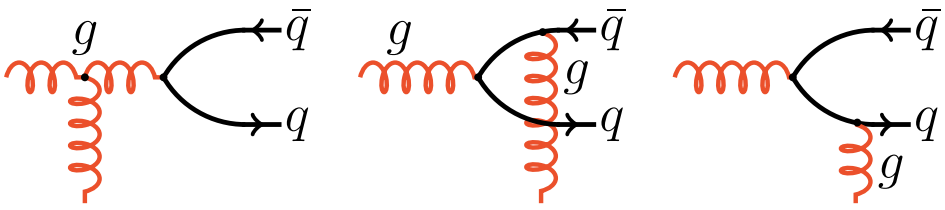

Figure 3.7: Possible $g \to q\bar{q}$ interactions with a gluon in the dipole picture.

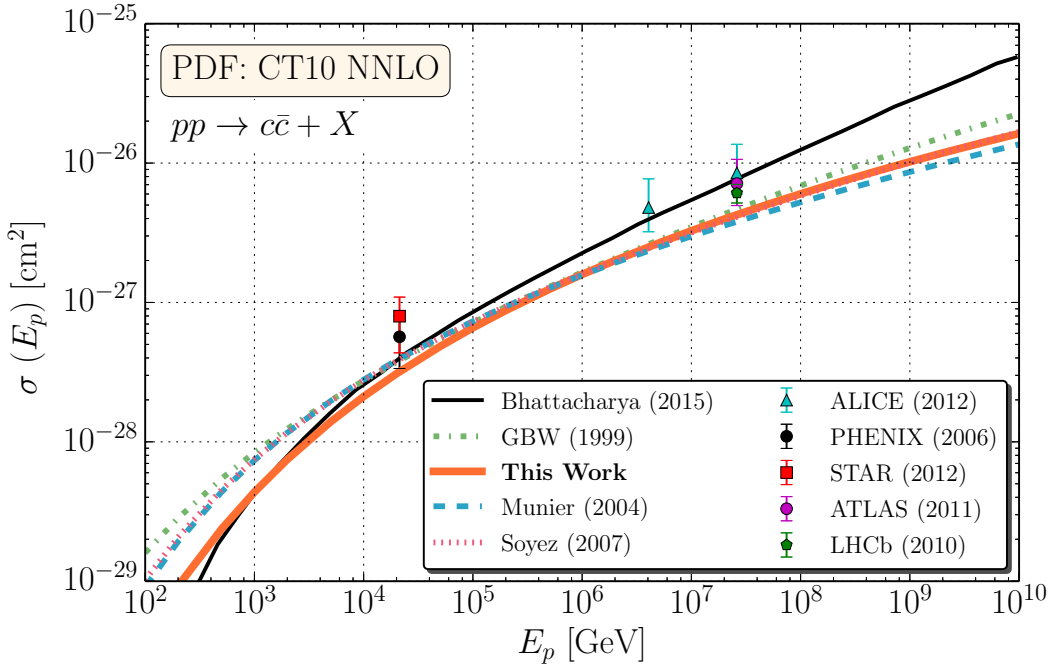

Figure 3.8: Charm production cross section in the dipole formalism.

plotted for different dipole models using the CT10nnLO gluon PDF with $\mu = \sqrt{4m_c^2}$ and $\alpha_s = 0.33$. The high energy dipole model evaluations of $\sigma(pp \to c\bar{c}X)$ are lower than the central perturbative evaluation of the charm pair cross section shown in, e.g. [95]. The perturbative calculation has large uncertainties associated with the scale dependence and for $E_p = 10^{10}$ GeV and scales dependent on factors of m_c, the uncertainty band drops to $\sigma \sim 10^{-26}$ cm^2, the level of the dipole prediction.

Chapter 4

Exploring New Physics with Neutrinos

"La duda es uno de los nombres de la inteligencia."
— Jorge Luis Borges, Diccionario privado de Jorge Luis Borges.[3]

In this chapter three new physics extensions that can be proved by performing precise measurements of atmospheric neutrinos with IceCube will be discussed; the three scenarios under consideration will be: eV sterile neutrinos 4.1, non standard neutrino interactions 4.2, and Lorentz violation 4.3.

4.1 Sterile neutrinos

Measurements of the Z^0 invisible width at LEP have established the number of *active* neutrinos, with masses less than half the Z^0 mass, to be three [96]; in this context *active* means that it participates in electroweak interaction i.e. it is charged under $SU(2) \times U(1)$. On the other hand, the LSND short baseline neutrino experiment has measured $P(\bar{\nu}_\mu \rightarrow \bar{\nu}_e)$, on a pion decay at rest experiment, finding oscillation compatible with $\Delta m^2_{LSND} \sim 1eV^2$ and $\sin^2\theta_{e\mu} \sim 0.003$ [97]. Since the existence of two other mass differences has already been established, it follows, that to accommodate this result, a new mass eigenstate needs to be introduced, which is called *sterile neutrino*. It is defined as: *a (light) sterile neutrino to be a neutral lepton*

[3] Doubt is one of the names of intelligence.

with no ordinary weak interactions except those induced by (mass) mixing [98]. This means that the lepton mixing matrix is extended so that

$$\begin{pmatrix} \nu_e \\ \nu_\mu \\ \nu_\tau \\ \nu_s \end{pmatrix} = \begin{pmatrix} & \tilde{U}_{PMNS} & & U_{e4} \\ & & & U_{\mu 4} \\ & & & U_{\tau 4} \\ U^*_{e4} & U^*_{\mu 4} & U^*_{\tau 4} & U_{s4} \end{pmatrix} \begin{pmatrix} \nu_1 \\ \nu_2 \\ \nu_3 \\ \nu_4 \end{pmatrix} \tag{4.1}$$

where new matrix elements $U_{\alpha 4}$ have been introduced. In principle, the measurements that has been performed on combinations of elements of U_{PMNS} should be revisited by the presence of the new elements, but in what follows it is assumed that the correction to the standard mixing angles, due to the existence of sterile neutrino, is smaller than their current error; thus $\tilde{U}_{PMNS} \approx U_{PMNS}$. The extended lepton mixing matrix can be parametrized in the following way

$$U(\theta_{ij}\delta_{ij}) = R_{34}R_{24}R_{14}R_{23}R_{13}R_{12}, \tag{4.2}$$

where each matrix R_{ij} is a rotation in the ij plane with rotation angle θ_{ij} and complex phase δ_{ij}, namely

$$R_{ij} = \begin{pmatrix} \ddots & & & & \\ & \cos\theta_{ij} & \cdots & \sin\theta_{ij}e^{-i\delta_{ij}} & \\ & \vdots & & \vdots & \\ & -\sin\theta_{ij}e^{i\delta_{ij}} & \cdots & \cos\theta_{ij} & \\ & & & & \ddots \end{pmatrix}. \tag{4.3}$$

In a minimal description only a subset of the δ_{ij} are required to be allowed to be non-zero; it is customary to place the standard three flavor complex phase in the 1-3 rotation. Furthermore, two new non-reducible phase are introduced, which in this work - for definiteness - are placed in the 3-4 and 2-4 rotations. The short baseline neutrino experiment that motivates the existence of a sterile neutrino are not sensitive to the sign of Δm^2_{41}, thus two possible sterile orderings exist. In the first one, the sterile neutrino is more massive than the active neutrinos, $\Delta m^2_{41} > 0$, which is commonly called the 3+1 scenario. In the second one the sterile neutrino is lighter than the active neutrinos, $\Delta m^2_{41} < 0$, which correspondingly is known as the 1+3 scenario; see Figure 4.1. Finally, strong bounds from cosmology on the sum of neutrino masses exist, namely

$\sum_i \nu_i < 0.23$eV[99]. This bound disfavor the 1+3 scenario: in what follows only the 3+1 scenario will be considered.

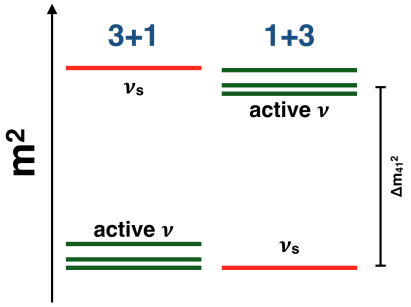

Figure 4.1: Sterile neutrino mass schemes. In the left diagram the sterile neutrino is more massive than the active ones (3+1 scheme), in the right diagram the sterile neutrino is lighter than the active ones (1+3 scheme). In both cases we have plot the active neutrinos in normal ordering.

Since the LSND anomaly was first published numerous experiments have tried to confirm the existence of eV-sterile neutrinos. These experiments can be classified as either disappearance experiments which measure either $P(\overset{(-)}{\nu}_\mu \to \overset{(-)}{\nu}_\mu)$ or $P(\overset{(-)}{\nu}_e \to \overset{(-)}{\nu}_e)$ or appearance experiments which have measured $P(\overset{(-)}{\nu}_\mu \to \overset{(-)}{\nu}_e)$. Detailed analysis of all neutrino experiments and channels in the presence of a sterile neutrinos has being performed [100, 101] finding a tension between appearance and disappearance experiments. In order to understand this tension, it is important to note that short baseline experiments studying $P(\bar{\nu}_e \to \bar{\nu}_e)$, e.g. reactor experiments, are sensitive to the effective disappearance amplitude $\sin^2 2\theta_{ee} \equiv 4|U_{e4}|^2(1 - |U_{e4}|^2)$, whereas long baseline experiments measuring $P(\overset{(-)}{\nu}_\mu \to \overset{(-)}{\nu}_\mu)$, e.g. MINOS, MiniBoone, SuperKamiokande, are sensitive to $\sin^2 2\theta_{\mu\mu} \equiv 4|U_{\mu4}|^2(1 - |U_{\mu4}|^2)$; finally, apperance experiments, e.g. LSND, MiniBoone, KARMEN, NOMAD, measure $\sin^2 2\theta_{\mu e} \equiv 4|U_{\mu4}|^2|U_{e4}|^2$. Appearance experiments, such as LSND and MiniBoone antineutrino channel, imply $|U_{\mu4}U_{e4}|^2 \neq 0$ [97, 102], which means that ν_μ and ν_e disappearance must be observed. Recent evaluation of the short baseline reactor experiments in light of a new reactor flux calculation point to 3-6% disappearance [103] which is compatible with a sterile neutrino solution. Also, gallium experiments such as GALLEX [104] and SAGE [105] point to a deficit of the same order [106, 107]. On the other hand, ν_μ disappearance in the sterile neutrino scale has never being found, but rather strong constrains have been placed on $|U_{\mu4}|^2$ [108, 109, 110]. Thus, in order to confirm the existence of sterile neutrinos ν_μ disappearance must be observed.

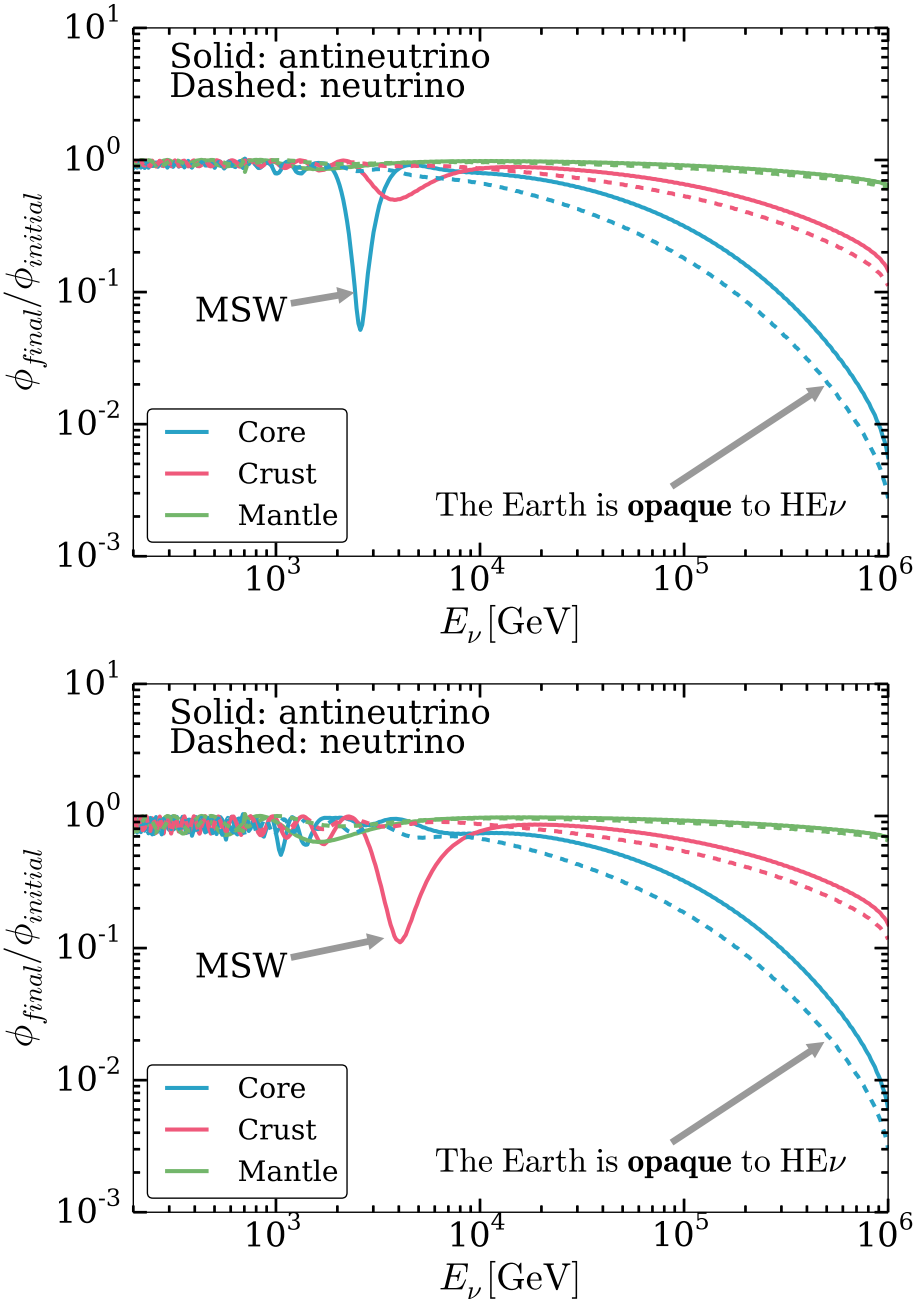

Figure 4.2: This figures illustrate the MSW effect. In the left figure the resonance is produced mainly in the core, whereas in the right figure on the crust. Furthermore, in both cases the effect of Earth absorption is illustrated.

Given the discussion above the role of IceCube is now clear: it must look for ν_μ disappearance induced by the $\Delta m^2 \sim 1eV^2$ scale. In order to understand the sterile neutrino phenomenology in IceCube, it is useful to consider a two level system between ν_μ and ν_s, whose Hamiltonian in the flavor basis is

$$H = \frac{1}{2}\tilde{U}^\dagger \begin{pmatrix} 0 & 0 \\ 0 & \Delta m^2_{41} \end{pmatrix} \tilde{U} \mp \frac{G_F}{\sqrt{2}} \begin{pmatrix} N_{nuc} & 0 \\ 0 & 0 \end{pmatrix} \tag{4.4}$$

where $\tilde{U}$ is a 2x2 matrix that has the effective sterile-active mixing angle, θ, and the "$-$" sign correspond to neutrino while the "+" sign corresponds to antineutrinos. It can be further written as

$$H = \begin{pmatrix} \sin^2\theta \frac{\Delta m^2}{2E} \mp \frac{G_F}{\sqrt{2}} N_{nuc} & \sin\theta\cos\theta\frac{\Delta m^2}{2E} \\ \sin\theta\cos\theta\frac{\Delta m^2}{2E} & \cos^2\theta\frac{\Delta m^2}{2E} \end{pmatrix} = \begin{pmatrix} -\cos 2\theta \frac{\Delta m^2}{2E} \mp \frac{G_F}{\sqrt{2}} N_{nuc} & \sin 2\theta\frac{\Delta m^2}{4E} \\ \sin 2\theta\frac{\Delta m^2}{4E} & 0 \end{pmatrix} + \cos^2\theta\frac{\Delta m^2}{2E}\mathbb{I}\,, \tag{4.5}$$

it is clear that resonant enhancement will occur when the off diagonal terms are greater than the diagonal contribution, which will happen when the diagonal terms are equal. Thus the resonant energy is [111, 72]

$$E_{res} = \mp \frac{\cos 2\theta \Delta m^2}{\sqrt{2} G_F N_{nuc}}\,. \tag{4.6}$$

An immediate conclusion from (4.6) is that if $\Delta m^2 > 0$ then the resonant conversion only happens in antineutrinos, obviously when the opposite happens it is in neutrinos. If the numbers $\Delta m^2 \sim 1eV^2$ and $N_{nuc} \sim N_{Earth}$ are plugged in this formulae, then $E_r \sim$ TeV! In order words, resonant antineutrino-sterile conversion happens on the region where IceCube has a myriad of atmospheric neutrinos. This is shown in Figure 4.2 for two sterile neutrino parameters such that in one case the resonant is triggered at the core and in the other at the mantle; in performing the calculations to create this figures we have use the full formalism described in Sec.2.3 in 3+1 neutrinos including interactions in the Earth. Furthermore, to illustrate the $E_r \sim \Delta m^2$ behavior let's consider the zenith average ratio of final to initial flux, $< \phi^{3+1}/\phi^{ini} >$, which we plot in Figure 4.3 for $\sin^2 2\theta = 0.1$.

It is interesting to note that for $\Delta m^2 > 5$ eV^2 the resonance occurs in the regime where neutrinos are absorbed in the Earth; i.e. Earth opacity is O(10%) for $\cos\theta_z = -1$. It has already been pointed out in the literature that when sterile neutrinos are included in the propagation on dense environments, the active neutrino transparency changes, e.g. in supernova, Sun [79]. In order to estimate this effect, the interaction

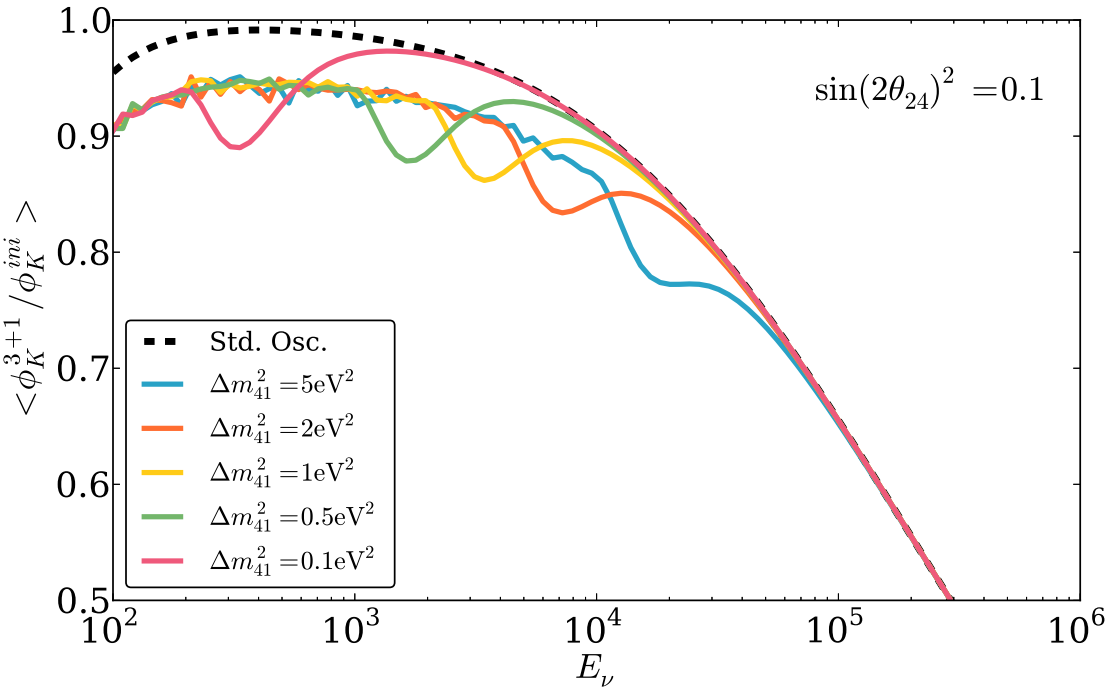

Figure 4.3: MSW effect dependence on the sterile mass splitting. This illustrates the relationship between the resonant energy and Δm^2, see 4.6.The vertical axis is the ratio of final to initial fluxes averages over zenith angle in the presence of sterile neutrino.

and oscillation scales need to be compared, see Figure 4.4. The aforementioned figure contains the three oscillation scales of which the only relevant scale for $E_\nu > 100$ GeV is the sterile scale, $L_{osc-sterile}$. The corresponding interaction length as a band, whose width correspond to the change in Earth density, has also been plotted. One can observe that the scales match at $O(10^5$ GeV), where the number of events are expected to be small.

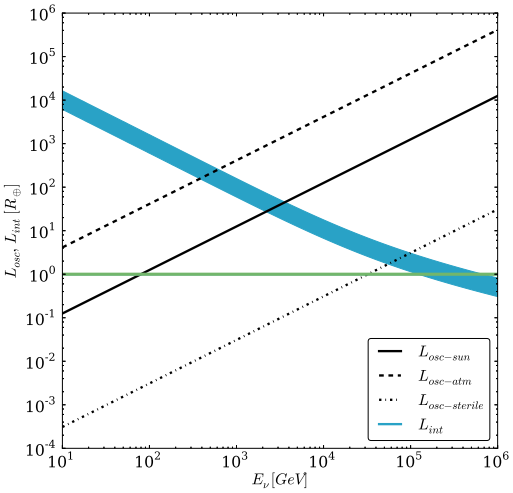

Figure 4.4: Comparison of interaction and oscillations scales as a function of neutrino energy. The solid green line corresponds to the Earth radius, the blue band is the interaction scale where the width of the band is due to the varying Earth density, and the black lines correspond to the first oscillation distance.

In order to quantify the error in separating oscillations and interactions it is useful to define

$$\phi^{fact}_{\nu_\mu}(E_\nu, x) \doteq P_{\nu_\mu \to \nu_\mu}(E_\nu, x) * e^{-\int_x \sigma(E_\nu) N(x) dx}, \tag{4.7}$$

where $P_{\nu_\mu \to \nu_\mu}$ is the oscillation probability calculated considering only forward coherent interactions and the exponential accounts for the Earth opacity. The difference between the factorizing and full solution for a large Δm^2_{41} and close to maximal mixing angle is plotted in Figure 4.5.

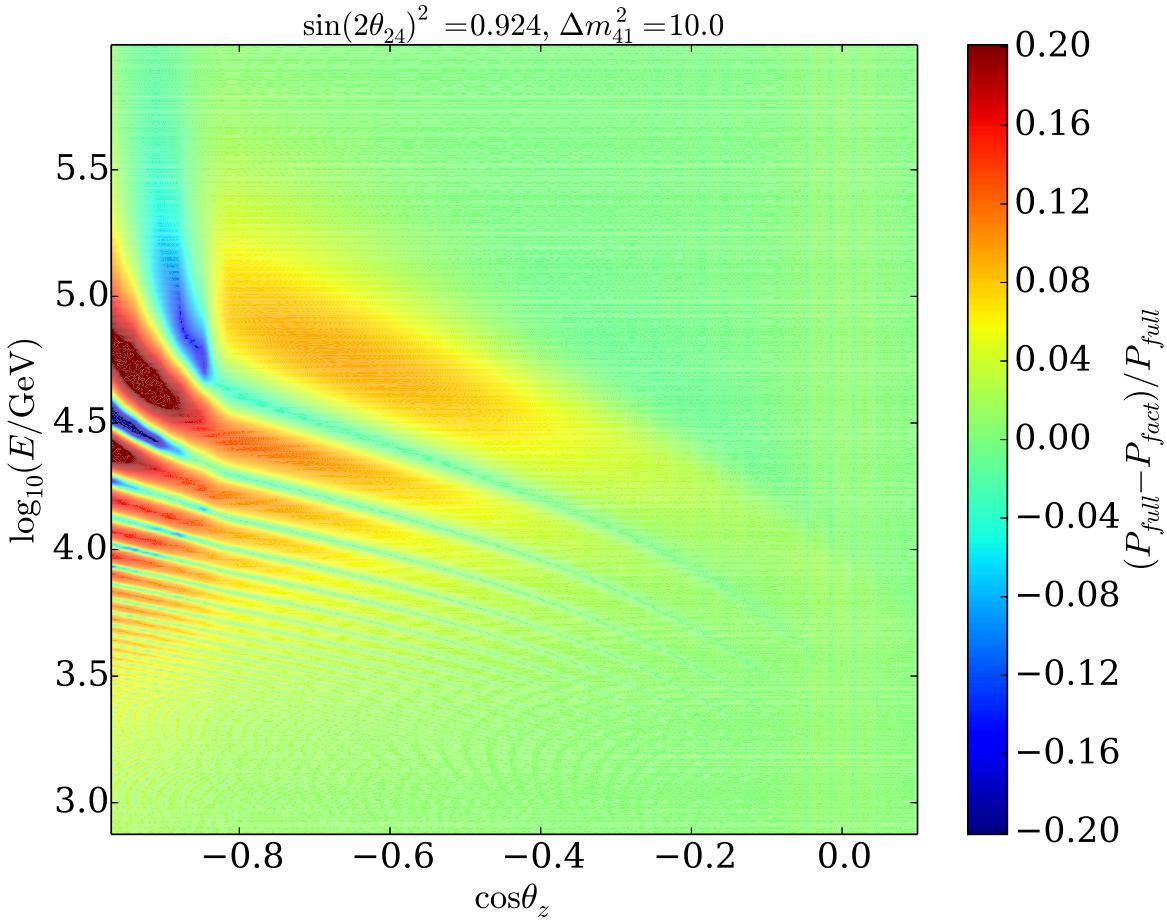

Figure 4.5: Comparison between full solution with respect to factorization approximation defined in Eq. 4.7.

4.2 Nonstandard Neutrino Interactions

In this section the standard neutrino interactions formalism will be extended. Let's first recall the standard model interactions. The charged current (CC) and neutral current (NC) interactions, which that were discussed in Sec. 2.1, arise from the Lagrangian operators

$$\mathcal{L}_{\mathrm{CC}} = \frac{g}{\sqrt{2}}\left[\ell_\alpha \gamma^\mu \frac{1-\gamma_5}{2}\nu_\alpha W_\mu^+ + h.c.\right], \tag{4.8}$$

and

$$\mathcal{L}_{\mathrm{NC}} = \frac{g}{2\cos\theta_w}\left[\nu_\alpha \gamma^\mu \frac{1-\gamma_5}{2}\bar{\nu}_\alpha Z_\mu^0\right]; \tag{4.9}$$

where g is the weak coupling constant, θ_w the weak mixing angle, ν_α the neutrino field of flavor α, and ℓ_α the charged lepton field. When the neutrino energy is much below the W mass, M_W, the interaction can be described via the Fermi effective dimension six operator

$$\mathcal{L}_{\mathrm{CC}}^{eff} = \frac{G_F}{\sqrt{2}}\left[\bar{\nu}_\alpha \gamma^\eta (1-\gamma_5)\ell_\alpha\right]\left[\bar{f}\gamma_\eta(1-\gamma^5)f\prime\right] + h.c., \tag{4.10}$$

and

$$\mathcal{L}_{\mathrm{NC}}^{eff} = \frac{G_F}{\sqrt{2}}\left[\bar{\nu}_\alpha \gamma^\eta (1-\gamma_5)\nu_\alpha\right]\left[\bar{f}\gamma_\eta(g_V^f - g_A^f)f\right]; \tag{4.11}$$

where $G_F = \sqrt{2}g^2 8M_W^2$ is the Fermi constant. The fermions f and $f\prime$ that appear on the effective CC lagragian are part of the same weak double, while in the NC lagrangian they can also be an iso-singlet. The coefficients g_V^f and g_A^f are the vector and axial vector couplings of the fermion f.

If it is assumed that new physics exists beyond the standard electro-weak interactions, then the new physics is most likely mediated by some heavy particle, or equivalently, can be realized by a similar effective six dimensional operator. Then, in analogy to the standard scenario, the new operators are of the form

$$\begin{aligned}\mathcal{L}_{\mathrm{NSI}}^{eff} =& \frac{G_F}{\sqrt{2}}\sum_{f,f\prime}\epsilon_{\alpha\beta}^{\mathrm{CC},f,f\prime}\left[\bar{\nu}_\alpha \gamma^\eta (1-\gamma_5)\ell_\alpha\right]\left[\bar{f}\gamma_\eta(1-\gamma^5)f\prime\right] + h.c. \\ &+ \frac{G_F}{\sqrt{2}}\sum_{f}\epsilon_{\alpha\beta}^{\mathrm{NC},f}\left[\bar{\nu}_\alpha \gamma^\eta (1-\gamma_5)\nu_\alpha\right]\left[\bar{f}\gamma_\eta(1-\gamma^5)f\right] + h.c.,\end{aligned} \tag{4.12}$$

where the ϵ parameters give the flavor structure as well as the strength relative to the standard weak interaction; i.e.

$$G_F|\epsilon| \sim \frac{g^2}{M^2_{\rm NSI}}, \tag{4.13}$$

which means that

$$|\epsilon| \sim \frac{M^2_W}{M^2_{\rm NSI}}. \tag{4.14}$$

It is further interesting to note that if a constraint on $|\epsilon|$ to the $O(10^{-3})$ level is placed, then masses $M_{\rm NSI}$ of $O(1\text{TeV})$ are being probed. Prospects of measurements of NSI in IceCube and PINGU have been recently studied in [12, 112]. Ohlsson et al. [112] claim that three years of PINGU can put bounds on $|\epsilon_{\mu\tau}| < 4.7\times10^{-3}$ and on $|\epsilon_{\tau\tau}| < O(10^{-2})$, while Smirnov et al. [13] state that one year of IceCube-79 with DeepCore can constrain $|\epsilon_{\mu\tau}|$ to 6×10^{-3}. Thus, if the IceCube collaboration were to perform these measurements it would start to probe the TeV scale: exciting!

The Hamiltonian of interest, in flavor, is given by

$$H = \frac{1}{2E}UM^2U^\dagger + H_{\rm std.matter} + \sum_f V_f\epsilon_f, \tag{4.15}$$

where V_f is the potential contribution arising from fermion f, namely $V_f \equiv \sqrt{2}G_F n_f$ where n_f is the fermion number density; and ϵ_f is a matrix that gives the flavor structure. Following Alexei Yu. Smirnov et al. **??**, the NSI parameter can be normalized relative to the d-quark density by introducing the matrix

$$(\epsilon)_{\alpha\beta} \equiv= \sum_f \frac{n_f}{n_d}(\epsilon^f)_{\alpha\beta}. \tag{4.16}$$

Then, for the Earth where $n_p \approx n_n$ the following equation holds

$$H_{\rm NSI} = V_{CC}\begin{pmatrix} \epsilon_{ee} & \epsilon_{e\mu} & \epsilon_{e\tau} \\ \epsilon^*_{e\mu} & \epsilon_{\mu\mu} & \epsilon_{\mu\tau} \\ \epsilon^*_{e\tau} & \epsilon^*_{\mu\tau} & \epsilon_{\tau\tau} \end{pmatrix} \tag{4.17}$$

where $V_{\rm CC}$ is the standard charge current potential strength. Finally, it is important to point out that the previous discussion was valid for neutrinos. For antineutrinos the transformations $V \to -V$ and $U \to U^\dagger$ need to be applied. Using the formalism in Sec. 2.3 and including this new term the neutrino muon survival probabilities are calculated for $\cos\theta_z = -1$, i.e. Earth core through going neutrinos, for $\epsilon_{\mu\tau} = 10^{-2}$ and

$\epsilon_{\mu\mu} = \epsilon_{\tau\tau}$. In the left panel of Figure 4.6 the result for neutrinos is shown, while on the right panel we illustrate the antineutrino scenario. For comparison the standard oscillation calculation is included. As can be seen, the location of the first oscillation maximum is modified by the NSI as well as O(20%) change in normalization at higher energies.

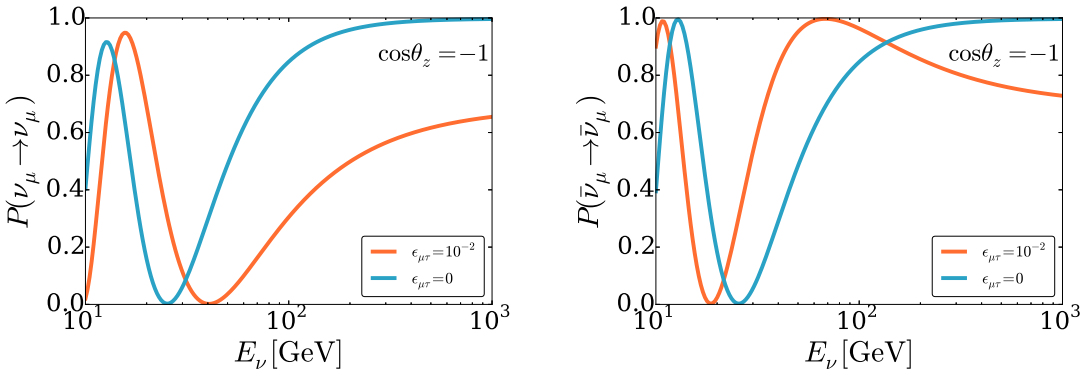

Figure 4.6: This figures illustrate the NSI effect in the IceCube-DeepCore range for $\epsilon_{\mu\tau} = 10^{-2}$. The right plot is for neutrinos while the left one is for antineutrinos.

4.3 Lorentz Violation and the Astrophysical Flavor Content

In section 4.1 we introduced new physics by incorporating a new neutrino state, in section 4.2 we included a new interaction between regular matter and neutrinos; in this section we will introduce generic new physics that scale like E^n. An effective way of introducing it in neutrino oscillations is by introducing new operators $\hat{H}_n$ of the form

$$\hat{H}_n = \left(\frac{E}{\Lambda_n}\right)^n \hat{O}_n. \tag{4.18}$$

The full Hamiltonian that incorporates the new physics operators, in the flavor basis, can be expressed as

$$H = \frac{1}{2E} U^\dagger M^2 U + \sum_n \left(\frac{E}{\Lambda_n}\right)^n \tilde{U}_n^\dagger O_n \tilde{U}_n = V^\dagger \Delta V, \tag{4.19}$$

where $M^2 = \mathrm{diag}(0, \Delta m^2_{21}, \Delta m^2_{31})$, $O_n = \mathrm{diag}(O_{n,1}, O_{n,2}, O_{n,3})$, and $\Delta = \mathrm{diag}(\Delta_1, \Delta_2, \Delta_3)$. O_n and Λ_n set the scale of the new physics and $\tilde{U}_n$ is the mixing matrix that describes the new physics flavor structure. Since we expect new physics to be suppressed at low energies the first terms in the expansion should be more relevant, thus in this work we will study $n = 0$ and $n = 1$.

These new operators can be interpreted in different new physics contexts. Some examples for $n = 0$ new physics are couplings between neutrinos and space time torsion [113] or CPT-odd Lorenz violation [114, 115, 116]. As for $n = 1$ new physics operators, CPT-even Lorentz violation and equivalence principle violation [117, 118, 119] are possible examples.

There are some constraints from neutrino oscillation experiments to these effective operators in the context of Lorentz and CPT violation [120]. The most stringent limits on certain parameters are obtained from Super-Kamiokande and IceCube atmospheric neutrino analyses [121, 122]. In this context the CPT-odd and CPT-even Lorentz violation coefficients are constrained to be $O(10^{-23}$ GeV) and $O(10^{-27})$ depending on the flavor structure $\tilde{U}_0$. These constraints can be used to set the scales of $n = 0$ and $n = 1$ operators introduced in this paper. For example, we set $O_0 \sim 1 \times 10^{-23}$ GeV as a current limit of the $n = 0$ operator, and $O_1 \sim 1 \times 10^{-23}$ GeV with $\Lambda_1 = 1$ TeV as a current limit of $n = 1$ operators, where $\frac{O_1}{\Lambda_1} = 10^{-27}$. Through this paper we have assumed the scale of O_1 is of the order of O_0 without loss of generality.

We can easily understand the scale given by the Super-Kamiokande and IceCube bounds. Note that the general expression for the neutrino oscillation probability in vacuum is given by Eq. (2.19), so that if the new mixing matrix is real then $P(\nu_\mu \to \nu_\mu) = 1 - \sum_{i>j} \sin^2\left(\frac{\Delta_{ij}}{2} L\right) [\cdots]_{i,j,\mu}$, which will only be significant if $\Delta_{ij} = O(\frac{1}{L})$. As noted in Figure 2.10 the Earth diameter is 10^{23}GeV^{-1}, which means that the constrains on the O_0 should be of order 10^{-23} GeV; just as we quote. Then a claim of a bound of 10^{-25}GeV on that operator just means that the amplitude is constrained to a precision of 10^{-2}. For the $n = 1$ case, we can write, $O_1 = \bar{c}E$ and constrained it to the same level. For the later, at SuperKamiokande higher energies of $E_\nu = O(10^2)$ GeV, translate to a constrain on $\bar{c}$ of order 10^{-25}, on the other hand for IceCube $E_\nu = O(10^4)$ GeV provides a constraint as high as 10^{-27} GeV. These simple considerations explain the strength of the limits quoted. If follows that IceCube would provide the best limits, from neutrino oscillation, to these operators. Finally, it is interesting to note that the non-standard interaction and these operators have indistinguishable effects in constant density environments as noted by Diaz[123]; thus to really differentiate between this two cases varying densities are required which makes the IceCube case stronger.

We use the formalism introduced in Sec. 2.3 to calculate the effect of these operators on the atmospheric neutrino flux. Since we are interested in the effect on ν_μ, we further consider the following flavor structure: for the O_0 operator,

$$\hat{O}_0 = \begin{pmatrix} 0 & 0 & 0 \\ 0 & 0 & a \\ 0 & a^* & 0 \end{pmatrix} , \tag{4.20}$$

and for O_1

$$\hat{O}_1 = \begin{pmatrix} 0 & 0 & 0 \\ 0 & 0 & c \\ 0 & c^* & 0 \end{pmatrix} E \, . \tag{4.21}$$

When considering these flavor structures the ν_μ survival probability is very close to an effective two level system. In this case the effect of these operators was studied by Halzen et al.[14] using the full formalism of oscillation and interactions that we have implemented. The result of their calculation is shown in Figure 4.7 for an initial power law spectrums of E^{-1} and E^{-3}; and $n = 1$ operator, since this is the more dominant one at high energies, for real $c = 10^{-23}$. It is interesting to see that since $\nu_\mu - \nu_\tau$ oscillations are induced the effect of tau regeneration needs to be taken into account specially if the spectrum is hard.

Since the operators grow with energy it is interesting to consider the effect in the IceCube astrophysical neutrinos. An operator O_0 with strength of $O(10^{-23}$ GeV) will be the dominant term in the Hamiltonian at neutrino energies of $O(1$ TeV), well below the energies of the IceCube astrophysical neutrino events. Equivalently for a neutrino energy higher than 35 TeV the neutrino oscillation is dominated by the new physics operators with scale of $O(10^{-26}$ GeV). Thus, the flavor content of the IceCube astrophysical neutrinos has the potential of probing scales much smaller than the current bounds.

To assess the impact of the operators in the astrophysical flavor ratio let's first consider the standard scenario expectation. In astrophysics charged pion decay from proton-proton collisions is one of the preferred neutrino production channels. In this scenario the initial flavor composition is $(\phi_e : \phi_\mu : \phi_\tau) = (1 : 2 : 0)$. Other scenarios such as rapid muon energy loss produce $(0 : 1 : 0)$, neutron decay dominated sources produce $(1 : 0 : 0)$ are of interest, while compositions such as $(0 : 0 : 1)$ are not expected in the standard particle astrophysics scenarios.

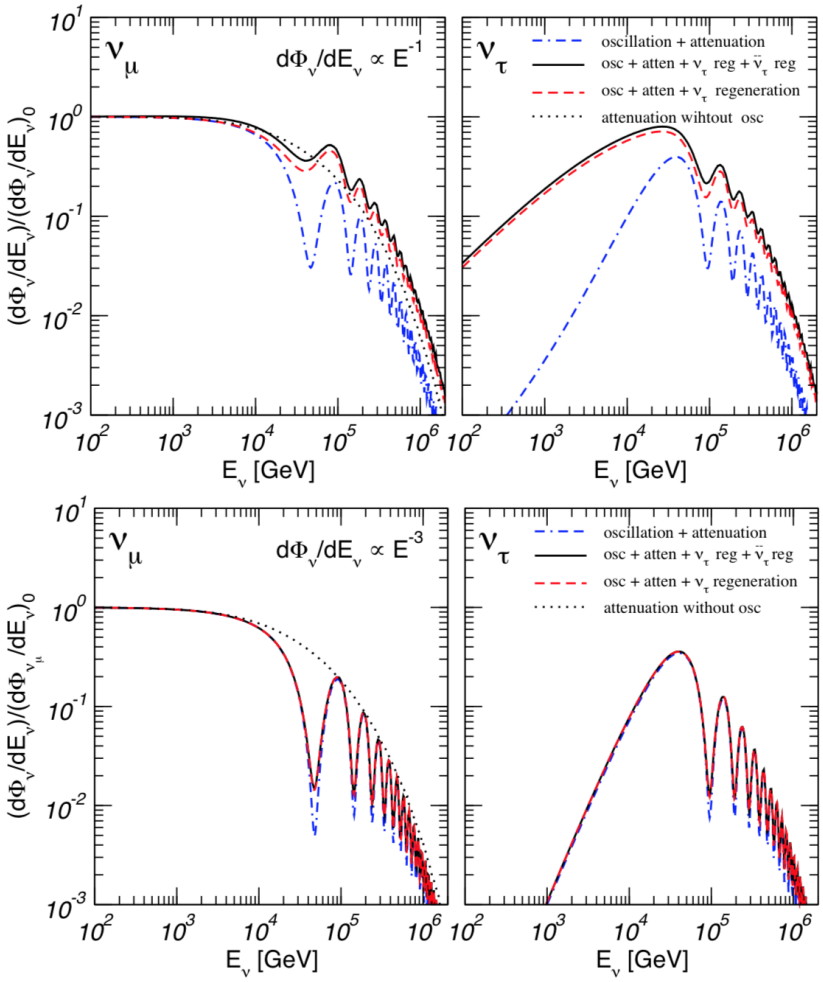

Figure 4.7: This figures illustrate the LV effect in the IceCube range for new physics operator O_1 with $c_{\mu\tau} = 10^{-23}$.

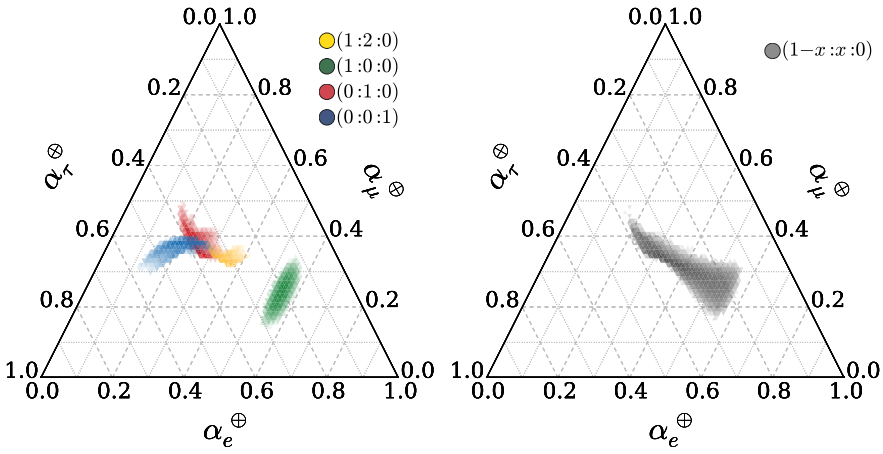

Figure 4.8: Allowed regions of the flavor content at Earth using the priors on the mixing angles and errors given from the current neutrino oscillation measurements. In the left plot, the different colors correspond to different assumptions on flavor content at the production. The color intensity is proportional to the probability density. In the right plot, we further sample the initial flavor content as $(x : 1 - x : 0)$.

The current measurements of the standard neutrino oscillation experiments allows us to determine the astrophysical neutrino flavor content at detection given an assumption of the neutrino production. In Fig. 4.8 we show allowed regions of the flavor content at Earth, where we use the standard mixing angles and their errors from the global fits [124] in order to produce density probability distributions for the flavor content. Since the CP-phase is not strongly constrained, we assume a flat distribution from 0 to 2π. Note that for simplicity we use the larger of the asymmetric errors and implement them as Gaussian. In the left plot, we assume four different production flavor composition hypotheses. We observe that all the allowed regions of astrophysical neutrino flavor content at Earth are close to $(1 : 1 : 1)$, except when the initial flavor content is $(1 : 0 : 0)$. In the right plot, we show the allowed region of the flavor content of the astrophysical neutrinos with all possible astrophysical production mechanisms, *i.e.*, the production flavor composition is sampled with $(x : 1 - x : 0)$ uniformly on x. Therefore, this rather narrow band covers all possible scenarios of the standard neutrino oscillations with the standard astrophysical neutrino production mechanisms.

In order to predict the flavor composition at Earth in the presence of new physics, the values of the mixing matrices $\tilde{U}_n$ should be specified. In order to show a prediction with new physics operators, we have to account for all the free parameters in the mixing matrix; we use a random sampling scheme to construct

the mixing matrix. A well established schema is the anarchic sampling [125, 126, 127, 128], which samples a flat distribution given by the Haar measure

$$d\tilde{U}_n = d\tilde{s}_{12}^2 \wedge d\tilde{c}_{13}^4 \wedge d\tilde{s}_{23}^2 \wedge d\tilde{\delta} \ , \tag{4.22}$$

where, $\tilde{s}_{ij}$, $\tilde{c}_{ij}$ and $\tilde{\delta}$ are the corresponding sines and cosines and phase respectively for the new physics n-operator mixing angles. We omit the Majorana phases since they do not affect neutrino oscillations.

In Fig.4.9 we show the allowed regions using anarchic sampling in the case where $H = \left(\frac{E}{\Lambda_n}\right)^n \tilde{U}_n^\dagger O_n \tilde{U}_n$. Notice that in this case, we neglect the mass term and we are considering that the Hamiltonian has only one operator, *i.e.*, $V = \tilde{U}_n$, so the result does not depend on n. Each plot in this figure correspond to a different production flavor composition. We show the pion decay production $(1:2:0)$, beta decay $(1:0:0)$, muon cooling $(0:1:0)$ and for completeness we show the exotic ν_τ dominant model $(0:0:1)$. The color density in these plots is a representation of the probability given by the anarchic sampling.

In Fig.4.10 we show the case where we have a mass term and the $n = 0$ operators. In the top left plot, we set $O_0 = 1.0 \times 10^{-23}$ GeV, corresponding to the order of the current best limit on this operator. On the top right plot we set $O_0 = 3.6 \times 10^{-26}$ GeV and the bottom plot we set $O_0 = 6.3 \times 10^{-28}$ GeV. These values are chosen because they have the same magnitude as the mass term with neutrino energy of $E_\nu = 35$ TeV and $E_\nu = 2$ PeV respectively. In this plot, the colors represent the different assumptions in the production flavor content, and the color intensity is the probability given by the anarchic sampling as in Fig.4.9.

In Fig.4.11 we show the case for the $n = 1$ operators. As before, the top left plot we set the new physics operator to the current best limit $\frac{O_1}{\Lambda_1} \sim 10^{-27}$. This is achieved by choosing $O_1 \sim O_0 \sim 1.0 \times 10^{-23}$ GeV and $\Lambda_1 = 1$ TeV. In the top right plot, $O_1 = 3.6 \times 10^{-26}$ GeV and $\Lambda_1 = 35$ TeV are used, and in the bottom plot the parameters are $O_1 \sim 6.3 \times 10^{-28}$ GeV and $\Lambda_1 = 2$ PeV. These choices make new physics to be the same magnitude as the mass term with neutrino energy of $E_\nu = 35$ TeV and $E_\nu = 2$ PeV, respectively. In other words, these choices explore new physics down to $\frac{O_1}{\Lambda_1} = 1.0 \times 10^{-30}$ and $\frac{O_1}{\Lambda_1} = 3.2 \times 10^{-34}$, well beyond what terrestrial neutrino experiments can achieve. The color notations and their intensities have equivalent meaning as Fig.4.10.

From Fig.4.10 and Fig.4.11 we observe that the allowed regions in the flavor triangle change in a similar way as a function of the energy scale. Comparing Fig.4.10 and Fig.4.11 with respect to the right plot in Fig.4.9, where the allowed regions are more symmetric, there is a preferred region along the vacuum oscillation triangle shown in Fig.4.8. It is interesting to notice that due to the unitary evolution and the fact

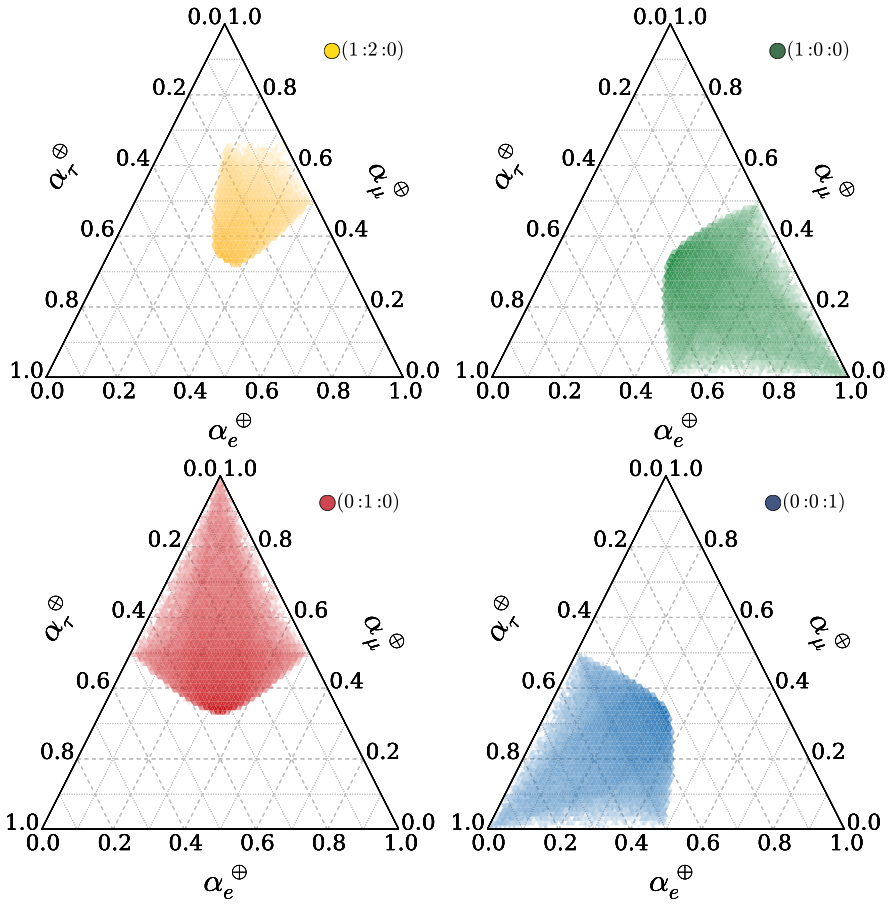

Figure 4.9: Allowed region using anarchic sampling on the mixing angles for the new physics operator when the mass term in the Hamiltonian is neglected. The different plots correspond to different assumption on flavor content at production. The color intensity is proportional to the probability predicted by anarchic sampling.

that the oscillations are averaged, for a given production flavor content, only a subset of the flavor triangle is accessible.

The pion decay production mechanism $(1 : 2 : 0)$ is one of the most natural astrophysical scenarios for high energy neutrino production. From Fig.4.10 and Fig.4.11 the allowed region for this case is the smallest, which means that if future measurements exclude this region, the pion production dominant mechanism is excluded regardless of the presence of new oscillation physics.

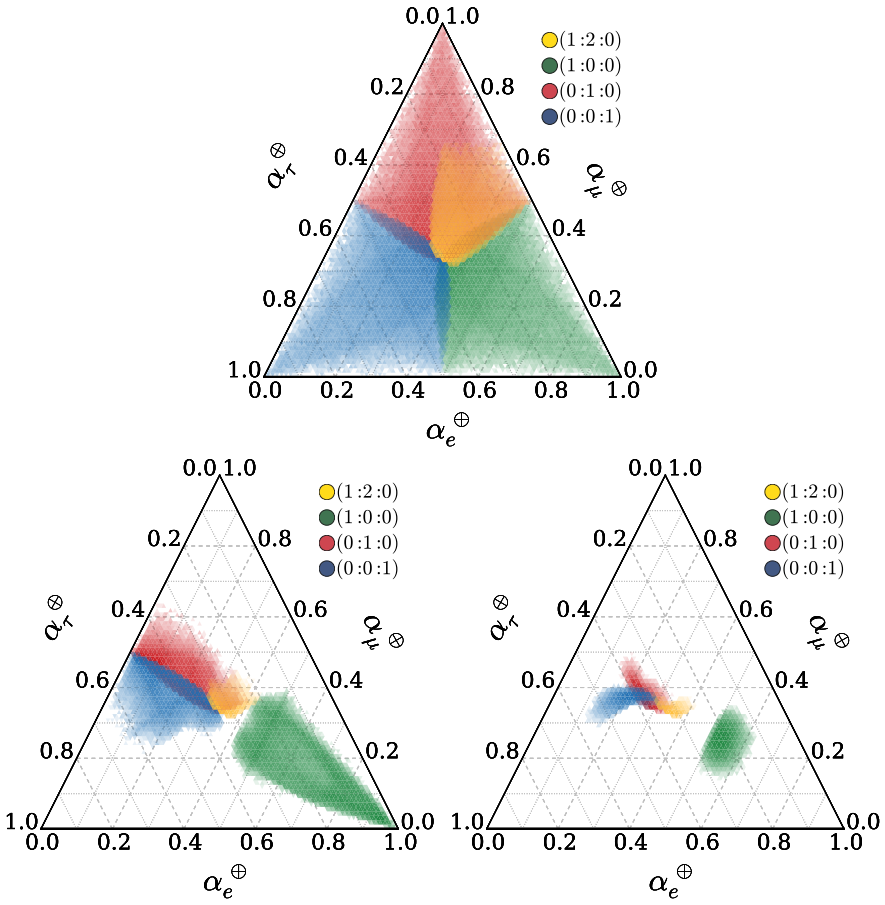

Figure 4.10: Allowed region using anarchic sampling on the mixing angles for the new physics $n = 0$ operators. The top plot corresponds to the current limits on $n = 0$ operator; the bottom left middle plot corresponds to $O_0 = 3.6 \times 10^{-26}$ GeV, while the bottom right plot corresponds to $O_0 = 6.3 \times 10^{-28}$ GeV.

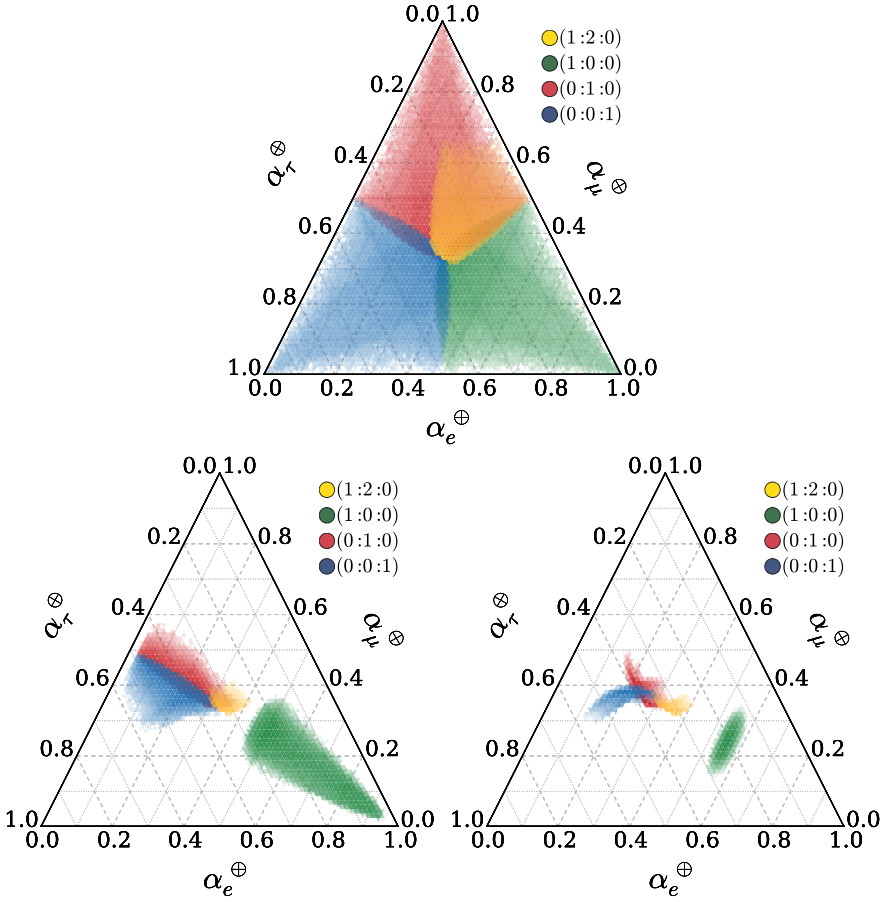

Figure 4.11: Allowed region using anarchic sampling on the mixing angles for the new physics $n = 1$ operators. The top plot corresponds to the current limits on $n = 1$ operator; the bottom left plot corresponds to $O_1 = 3.6 \times 10^{-26}$ GeV and $\Lambda_1 = 35$ TeV ($\frac{O_1}{\Lambda_1} = 1.0 \times 10^{-30}$), while the bottom right plot corresponds to $O_1 = 6.3 \times 10^{-28}$ GeV and $\Lambda_1 = 2$ PeV ($\frac{O_1}{\Lambda_1} = 3.2 \times 10^{-34}$).

Chapter 5

Constraints on Sterile Neutrinos With IceCube

"Arribo, ahora, al inefable centro de mi relato, empieza aquí, mi desesperación de escritor. Todo lenguaje es un alfabeto de símbolos cuyo ejercicio presupone un pasado que los interlocutores comparten; ¿cómo transmitir a los otros el infinito Aleph, que mi temerosa memoria apenas abarca?"

— Jorge Luis Borges, El Aleph.[5]

In Chapter 2 the properties of neutrinos and neutrino oscillations have been reviewed, in Chapter 3 an overview of the atmospheric neutrino flux was given, and in Chapter 4 new physics scenarios that can be studied using IceCube atmospheric data were presented. Finally, in this chapter, the moment of truth has come: Are there sterile neutrinos signatures in the IceCube atmospheric neutrino energy and zenith distributions?

5.1 Signature and Model

First let's revisit the sterile neutrino signature in IceCube. The effect of sterile neutrinos in the ν_μ survival probability was already discussed in Section 4.1. The most important feature is the MSW conversion of $\bar{\nu}_\mu$ to $\bar{\nu}_s$. IceCube measures the survival probability as a function of $\cos\theta_z$ and E_ν. In what follows a simplified sterile neutrino model will be considered in which the only new mixing angle that is allowed to be non-zero is θ_{24}; thus in this chapter when θ is used it always refers to this angle. The effect of the sterile neutrinos is

[5] I arrive now at the ineffable core of my story. And here begins my despair as a writer. All language is a set of symbols whose use among its speakers assumes a shared past. How, then, can I translate into words the limitless Aleph, which my floundering mind can scarcely encompass?

illustrated in Figure 5.1 for the global best fit sterile parameter space, under the assumption that only θ_{24} is non-zero.

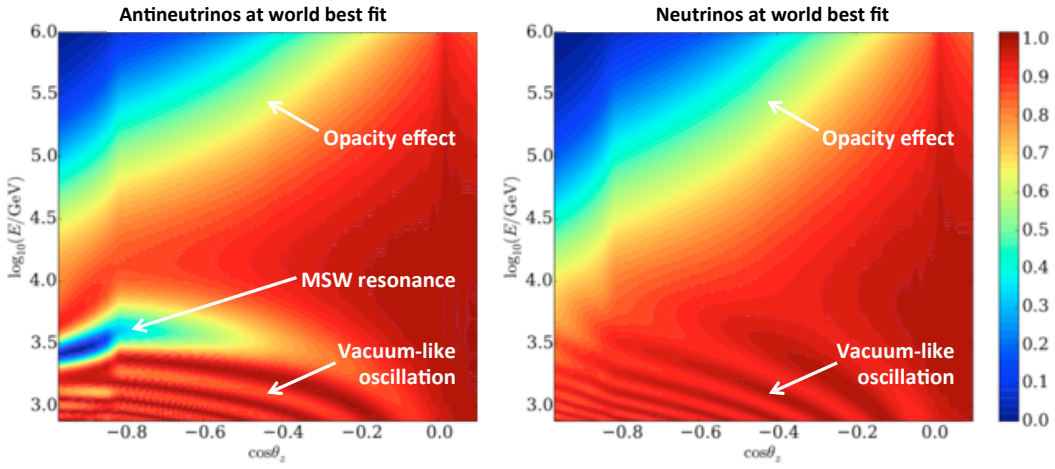

Figure 5.1: ν_μ disappearance probability in neutrino and antineutrinos as a function of energy and zenith with $\sin 22\theta = 0.15$ and $\Delta m^2_{41} = 1eV^2$.

Of course, the IceCube neutrino observatory does not directly observe neutrinos, but rather the products of neutrino interaction: muons and showers. Muon reconstruction at energies greater than 500GeV is based on the muon energy loss and is described in [129]. It is more meaningful to *see* the sterile neutrino signatures in reconstructed quantities. In Figure 5.2, the effect of sterile neutrino as a function of reconstructed zenith and muon energy proxy is shown. It is clear that there is not a one-to-one correspondence between the proxy and the incident muon energy, and further there is not a one-to-one map between that energy and the incident neutrino energy. From the most strict point of view the only thing we know is that the muon started where its first light is detected; of course then we can assign probabilities of it starting at earlier times. From these educated estimations we can obtain neutrino energy distributions, but not *a* neutrino energy. Thus, the stronger the correlation between proxy, muon, and neutrino energy the better.

From Figure 5.2 we can note that the sterile neutrino signature has a characteristic energy-proxy/zenith signal and that we are looking for effects at the 10% level. Furthermore, the fact that the parameter space, which are shown on the upper left corner, covers several orders of magnitude: in Δm^2_{41} from 10^{-2} to 10 and in $\sin^2 2\theta_{24}$ from 10^{-2} to 1 means that the sterile neutrino signature can have effects in all the energy-proxy/zenith plane, which implies that we do not have control regions.

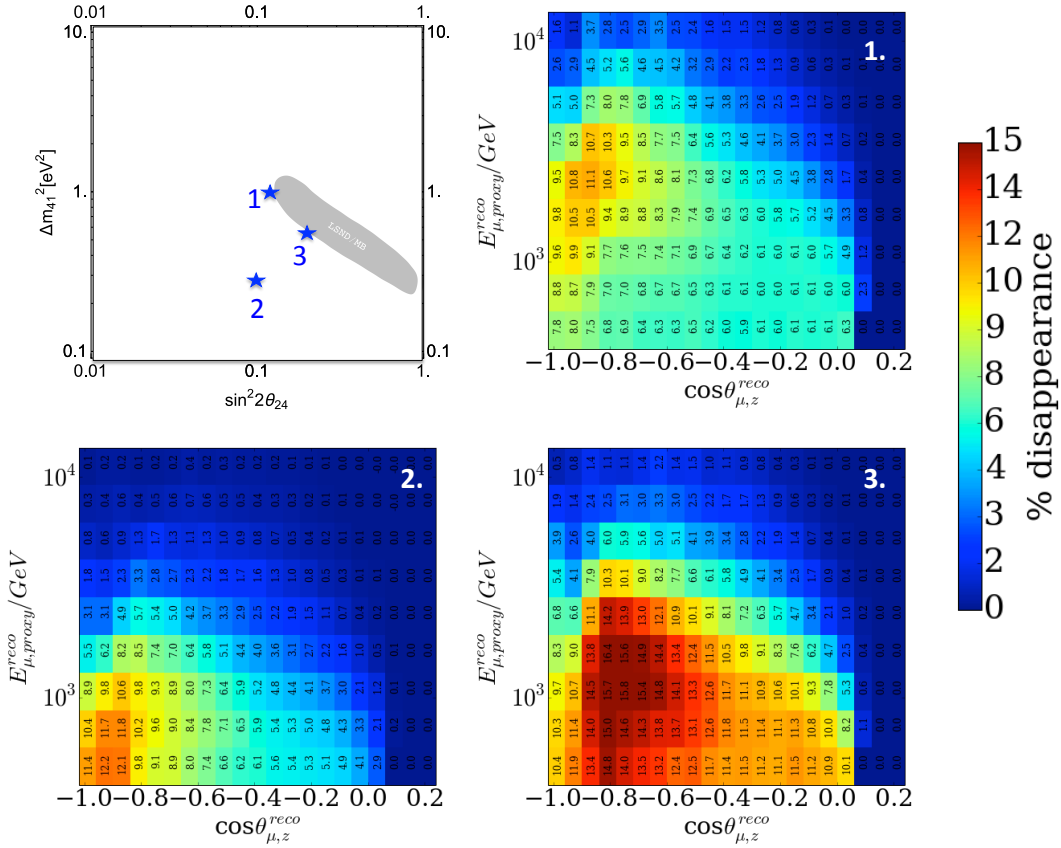

Figure 5.2: The effect of the sterile neutrino in reconstructed quantities. The upper left diagram illustrates the sterile neutrino parameter space; three parameter points are mark for illustration. The upper right Figure corresponds to parameter point one, while the lower left and right to two and three respectively. The color scale gives the disappearance percentage in each bin.

5.2 Event Selection

The event selection was performed by C. Weaver [16, 17] and consists of a high purity cut based on the up going muon set. It is now worthwhile to introduce the *analysis binning* which corresponds to ten logarithmically spaced bins in the muon energy proxy and twenty bins linearly spaced in $\cos\theta_z$. The binning has not been optimized for the analysis, but rather arises from IceCube energy and direction reconstruction properties as well as to try to maintain large Monte Carlo statistics per bin in order to guaranty an accurate prediction. The event distribution in the analysis space is shown in Figure 5.3. With respect to the original C. Weaver selection we have reduced the event selection by cutting events above $E_{proxy} = 4 \times 10^4$ in order to avoid the astrophysical background as well as reducing potential prompt contamination. Furthermore, we have also introduced a low energy proxy cut in order to avoid the standard oscillation energy range as well as to avoid increasing detector effects that become more important at low proxy, e.g. hole ice, ice models, etc. As noted on the work of C. Weaver on the behavior of the energy proxy in this event selection the correlation between the incident muon energy is lost for values of the proxy less than 400 due to the nature of the proxy which is based on muon energy loss. This defines the lower bound on the energy proxy.

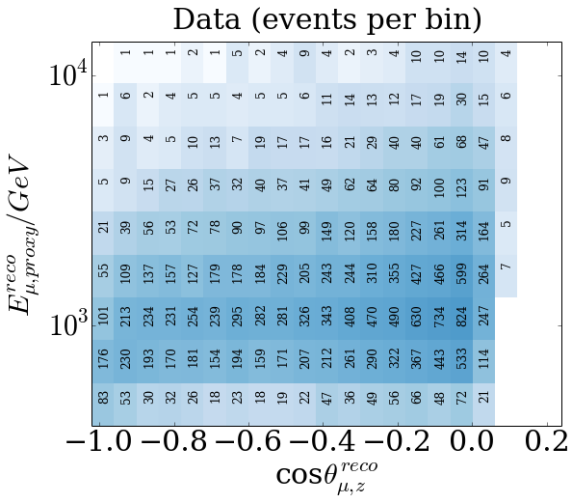

Figure 5.3: Event distribution as a function of energy proxy and reconstructed $\cos\theta_z$.

It is important to note that most of the events are around energy proxy $O(10^3)$, which translates to muon energies of $O(10^3\text{GeV})$; see appendix on [17]. This is the energy range in which we expect sterile neutrino effects to be significant as noted on Section 4.1.

As we saw in Section 4.1 the sterile neutrino effect is an $O(10\%)$ effect on the LSND based fix point, being considerably larger as $\sin^2 2\theta$ increases. In Figure 5.4 the statistical errors on the analysis binning is shown in reconstructed and true quantities. What is important to note here is that the statistical error when the muon energy proxy is $O(10^3)$ is between $5-7\%$), which implies that the statistics are just enough to perform the analysis. Note, though, that what gives the analysis sensitivity, as explained in Section 4.1, is a very specific energy-zenith correlation, which will allow us to go further than simple statistics arguments would suggest. An improved version on this analysis could be performed on the the already collected four years of IceCube-86, which would then reduce the statistical errors to about 3%.

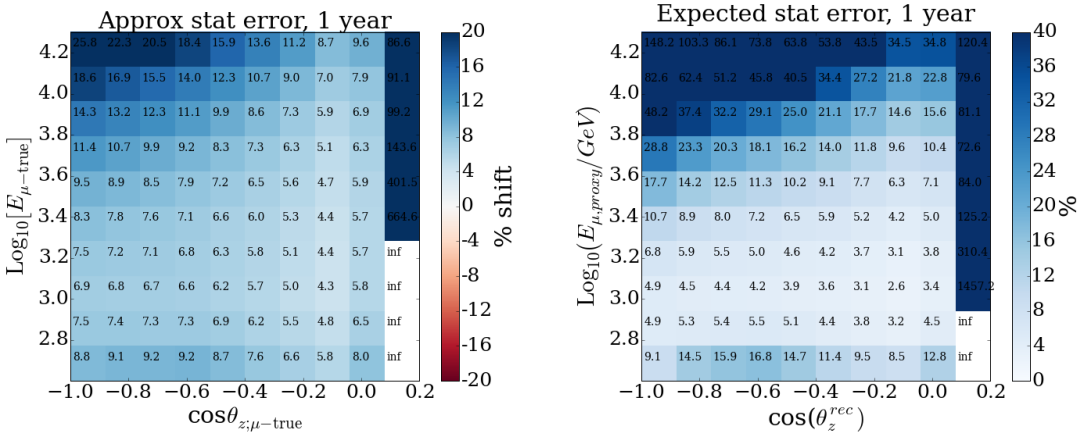

Figure 5.4: Statistical errors on the final selection in true and reconstructed quantities.

5.3 The analysis

In this section the main features of the analysis will be described. The analysis, performed and designed in collaboration with Benjamin J. P. Jones and Jordi Salvado, is a blind analysis. In this section the pronoun *we* refers to those two gentlemen and myself. Thus the analysis had three stages: the pre-unblinding checks, the box opening, and the post unblinding discussion.

5.3.1 First Stage: preunblinding

The first stage, after recognizing C. Weaver's event selection as idoneous for this analysis, was to identify the main systematics and decide on the analysis' statistical procedure. Weaver had already included several systematics regarding atmospheric neutrino uncertainties and some detector effects. The original continuous

Continuous parameter	Central value	Gaussian prior width
normalization (N_0)	1	no prior
DOM Efficiency (ϵ)	0.99	no prior
cosmic ray spectral shift ($\Delta\gamma$)	0	0.05
π/K ratio	1	0.1
$\nu/\overline{\nu}$ ratio	1	0.025
atmospheric density shift (δ)	0	tuned per-model

Table 5.1: Continuous nuisance parameters used in the fit. The central values are with respect to each flux model, while the errors quoted are assumed the same in all models.

systematics considered by C. Weaver were: normalization of the atmospheric spectrum (N_0), ratio of pion and kaon contributions ($R_{\pi/K}$), uncertainty in the cosmic ray spectral index ($\Delta\gamma$), and DOM efficiency (ϵ). We can compactly write the initial atmospheric ν_μ flux when considering these nuisance parameters as

$$\phi_{atm}(\cos\theta, E_\nu) = N_0\Big(\phi_K(\cos\theta, E_\nu) + R_{\pi/K}\phi_\pi(\cos\theta, E_\nu)\Big) \times E_\nu^{-\Delta\gamma} \tag{5.1}$$

where these were included as nuisance parameters in a maximum likelihood problem with priors given in Table 5.1. It was promptly realized that we needed to include the $\nu/\bar{\nu}$ ratio since the sterile neutrino MSW effect only occurs, for the $3+1$ model, on antineutrinos. The use of only the Honda model as an atmospheric neutrino prediction was a concern from the early on the analysis since this model was tuned for sub 10TeV energies and later patched to higher energies, and further it was the main origin of the atmospheric priors. This problem was not solved until A. Fedynitch [6] released the MCeq package [89] which allowed the solution of the cascade equations which predict the atmospheric fluxes. Using this package G. Collins et al. [4] used the AIRS satellite data to construct the atmospheric models which I described in Chapter 3. We could now predict the atmospheric flux. This allowed us to confirm the parameters given in Table 5.1.

It was further realized that we needed to include the effect of atmospheric density uncertainty, which has an energy and zenith dependency and is much greater as one approaches the horizon, since there is less data from the AIRS satellite in the south pole atmosphere. The deviations are small, so we decided to use a linear correction $\cos\theta$ and E, and constructed a function whose effect was predominantly around the horizon where the uncertainties were larger; the following parametrization was used[1]

$$\epsilon(\cos\theta, E_\nu; \delta) = 1 + (\cos\theta + \cos\theta_0)\delta\left[1 + \frac{(E_\nu - E_0)}{E_1}\frac{1}{1 + \mathrm{Exp}\left(-\kappa(\cos\theta + \cos\theta_0)\right)}\right]. \tag{5.2}$$

[1] In some IceCube internal documentation you may find this parametrization named as the Jordi-δ construction.

where the parameters E_0, E_1, κ, and $\cos\theta_0$ were fitted and fixed from the atmospheric model variations[2]. Then the error on the atmospheric uncertainty is controlled by the dimensionless parameter δ, whose prior we change for each model and is of O(0.05). This finalizes all the atmospheric neutrino nuisance parameters.

Even though the atmospheric uncertainties dominate this analysis, we – of course – studied all the detector systematics. C. Weaver had already included the effect of changing the Digital Optical Module (DOM) efficiency by generating MC data sets for five DOM efficiency values and then constructing a spline **??**, which gave the effect of changing the DOM efficiency in final reconstructed quantities; analysis space. As I already mentioned the goal of this analysis was to have systematic control on the detector side of O(10%). The detector systematics that we decided to include and study were the following: DOM efficiency, DOM oversizing, Ice model variations, and hole ice effect. We promptly realized that we had a serious problem. The existing IceCube MC statistical uncertainties for the default configuration of the detector on the analysis space had errors of O(30%), and the systematic variations available had errors of O(100%). Even more, the IceCube MC was designed to start in the upper atmosphere and was designed in such a way that the effect of Earth propagation could not be disentangled after the fact. There was only one solution: we needed a new MC system that started in the vicinity of the detector and had titanic statistics for the default configuration and all systematic variants. The designed of this new *system*, which we called NuFSGen – NeUtrino Final State Generator –, was a process that took O(1year); I briefly sketch this MC approach on Appendix A. Obviously, the production and extensive testing of this Monte Carlo was only possible through great collaborative effort, of whom I would specially like to thank P. Desiati, G. Merino, J.C. Diaz-Velez, C. Weaver, J. van Santen, D. Chirkin, D. Schultz, C. Kopper, and many others.

With the NuFSGen Monte Carlo in place we were ready to assess the effect of all systematics. First, let's see the effect of the original Weaver systematics in the analysis space. Those are shown in Figure 5.5. As expected changing the spectral index changes the event count at the tail of the distribution. Changing the DOM efficiency changes the position of the peak of the distribution and distorts the low energy tail. Increasing the Kaon fraction increases the overall rate above 700 energy proxy units and reduces it below it. From the effect of the one dimensional distribution one might get the impression that the π/K ratio, for example, is degenerate with the effect of the DOM efficiency change. There is some truth in that statement, when performing a fit on the nuisance parameters there exist correlation between the different nuisance parameters. But it is important to remember that the fit is performed in muon energy proxy and zenith,

[2] We use $E_0 = 360$GeV, $E_1 = 11279$GeV, $\kappa = 200$, and $\cos\theta_0 = 0.4$.

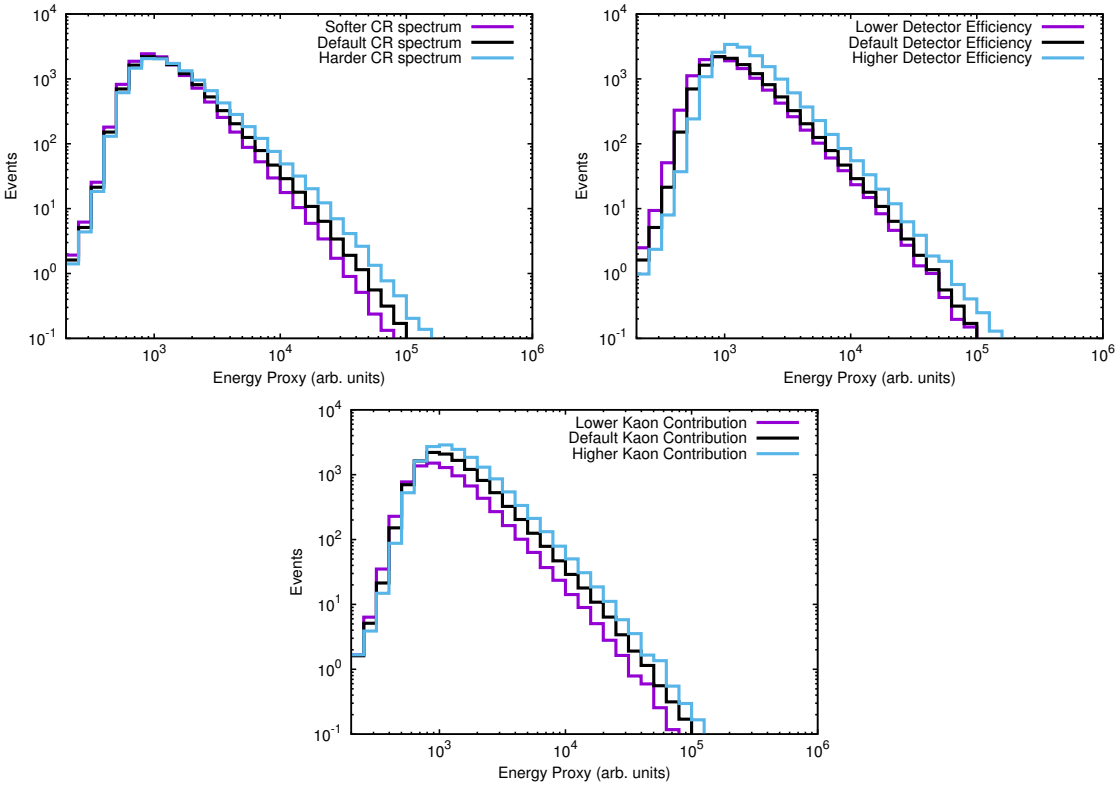

Figure 5.5: Effects of continuous systematics on the event distribution. The upper right plot shows the effect of changing the cosmic ray spectral index and the upper left shoes the effect of changing the DOM efficiency. Finally, the lower panel shows the effect of increasing the Kaon component normalization.

not only in one or the other; thus e.g. the zenith effect of the DOM efficiency is different from the π/K one breaking degeneracies. Figure 5.6 shows the effect of changing the DOM efficiency from its nominal value, 0.99, to 0.9, 0.95 in the upper panels and to 1.089, 1.1979 in the lower ones. This Figure illustrates why the DOM efficiency is such an important systematic, it has distinct energy effect that is of O(10%). Our spline allows us to calculate the effect of the DOM efficiency variation for intermediate values than those shown in these panels.

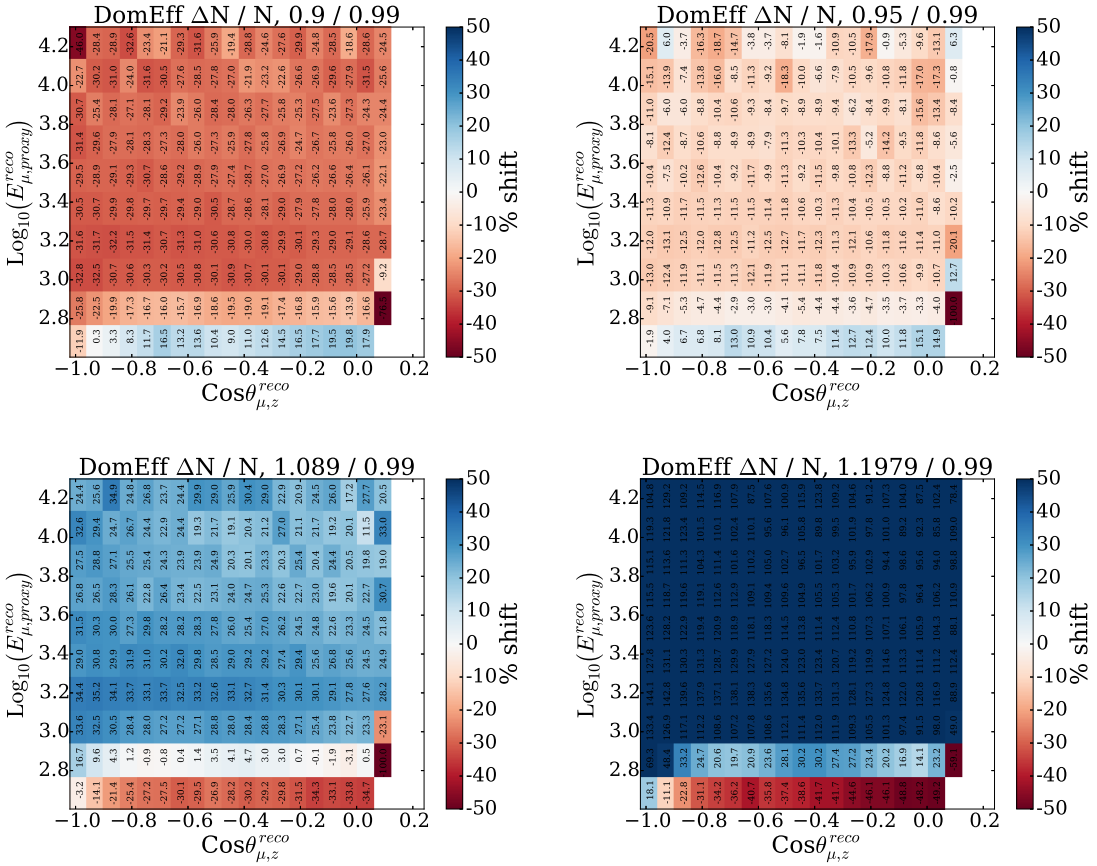

Figure 5.6: Effects of the DOM efficiency change on the final event selection.

Another important effect in the MC generation is the DOM oversizing, which is an approximation that is done in the conventional IceCube MC which assumes that the DOM is bigger than its physical size in order to reduce MC generation time. Commonly, an oversizing of factor five is used, i.e. the DOM area is a factor 25 larger in the simulation. It turns out that for muon energy proxy less than 10^3 the DOM oversizing approximation breaks down causing mismodeling in the MC. This effect is shown in Figure 5.7 where in the

right panel we illustrate the DOM oversizing approximation and on the right panel we show its effect on the analysis space. The reason that DOM oversizing rescaling works at higher energies is that the average DOM to event distance is larger, so the ratio of the area oversized disk and the photon surface area is close to one. On the other hand, when the events happen close to DOMs, as depicted on the second diagram, then the ratio of the surface of a sphere to that of a plane is not close to one. This is why the NuFSGen MC does not use oversizing.

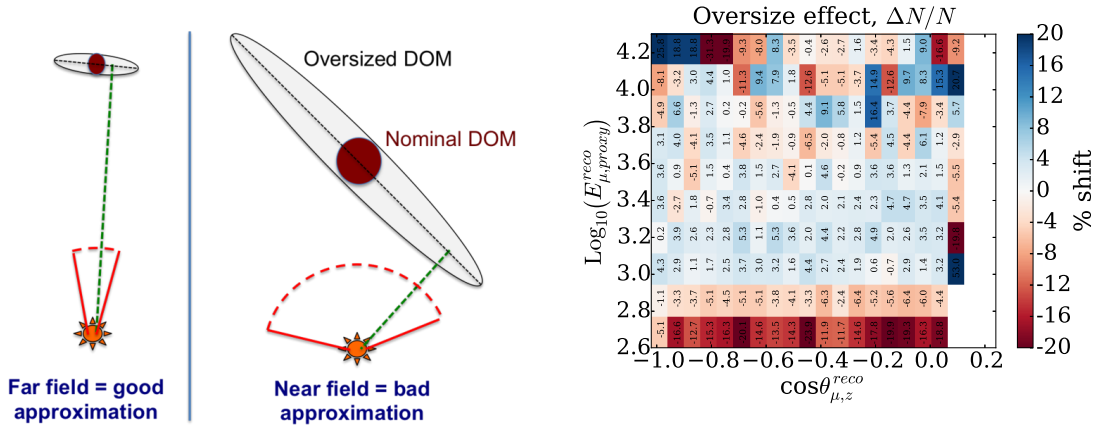

Figure 5.7: Left panel illustrates the oversizing approximation. Right panel shows the effect of DOM oversizing on the final distribution.

The next important detector effect is the hole ice effect which is shown in Figure 5.8. The hole ice effect arises from the fact that, when the hot water drill deploys the IceCube DOMs in chains and the water refreezes it behaves differently than the unperturbed bulk ice. It turns out that the hole ice effect is subdominant with respect to those previously discussed, more over the effect of changing the ice model has a comparable size.

This motivated the following analysis strategy. Large effects, such as the flux systematics, we will address as continuous variations when doing the fit. Smaller effects, such as hole ice, ice model variations, and cross sections, we will treat as discrete variations. This invites the following definition for the log-likelihood

$$\log \mathcal{L}(\sin^2 2\theta_{24}, \Delta m^2_{41}) = \min_{\vec{\theta},\{d\}} \left(\sum_{i=1}^{N_{bins}} \Big[x_i \log \lambda_i(\vec{\theta}, d) - \lambda_i(\vec{\theta}, d) \Big] + \sum_{\eta} \frac{(\theta_\eta - \Theta_\eta)^2}{\sigma^2_\eta} \right), \tag{5.3}$$

where $\vec{\theta}$ corresponds to the continuous nuisance parameter vectors, d the set of discrete systematic parameters, and $\lambda_i(\vec{\theta}, d) = \lambda_i(\vec{\theta}, d; \sin^2 2\theta_{24}, \Delta m^2_{24})$. In practice for each sterile neutrino parameter point,

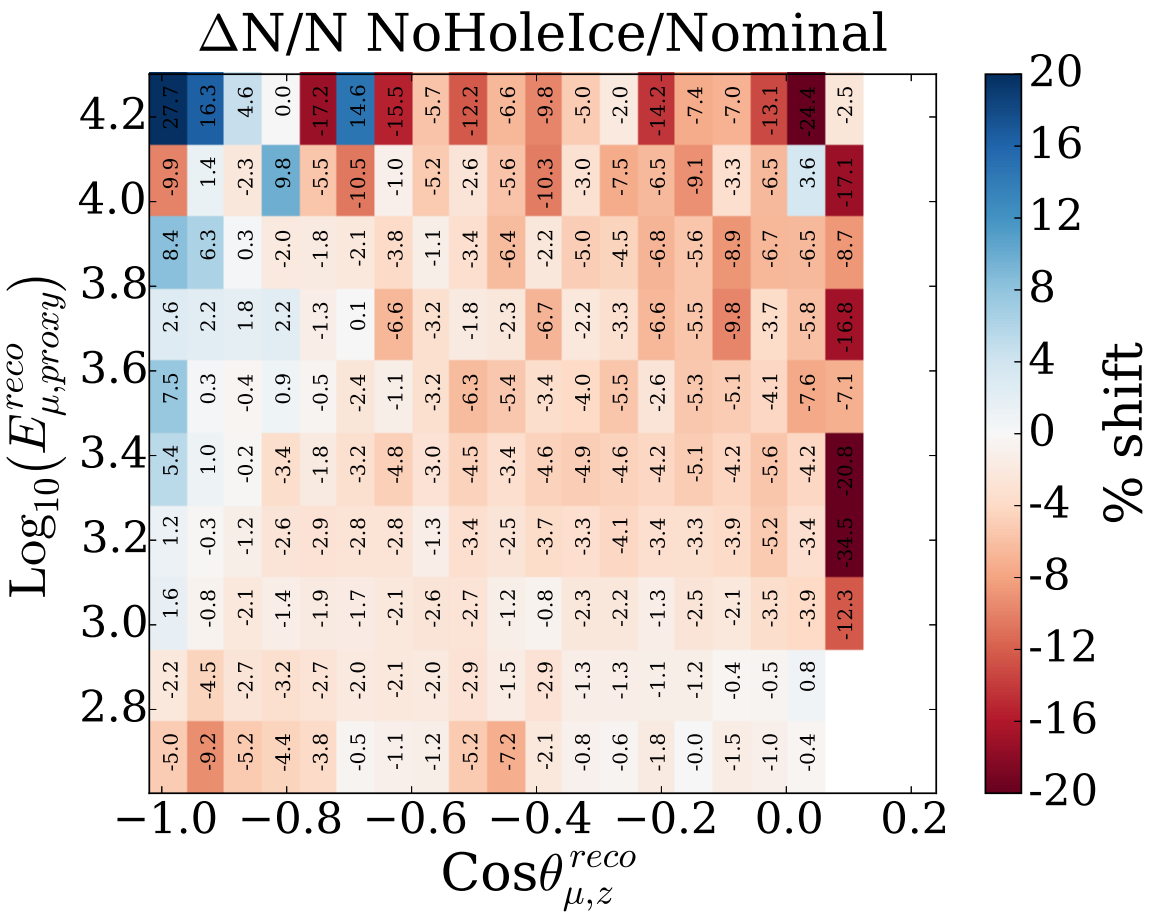

Figure 5.8: Effects of hole ice on the final distribution.

$(\sin^2 2\theta_{24}, \Delta m^2_{24})$, and fixed d we minimized on $\vec{\theta}$, and then, at the end, we minimized on $\{d\}$. For computational reasons we could not minimize on $\{d\} = \{\text{flux variant}\} \times \{\text{detector variant}\}$, but rather we just did $\{d\} = \{\text{flux variant}, \text{detector variant}\}$, i.e. when a detector variant was used we used the Honda flux, while when a flux variant was used we used the default detector configuration. After defining the statistical procedure, we then performed data challenges for the null hypothesis and signal points and found that within expected errors we recovered the injected hypothesis. Another important procedure to agree on prior to unblinding was how the significance was going to be calculated. Due to computational limitation a full Feldman-Cousins (FC) [130] could not be performed. We decided that we would unblind and quote initial significances using Wilk's [131] theorem and then validate it adding several points through the FC method.

We calculated the estimated sensitivity which we shown in the *brazilian* plot in Figure **??**. In this Figure the dashed line represents the mean sensitivity, while the yellow and green regions corresponds to the bands that encompass 68% and 95% of the null hypothesis injected 90% confidence levels from one thousand simulated pseudoexperiments, respectively.

Parameter	**Expectation**	**Our prior**	**From [17]**	**This work**
normalization	1	no prior	0.93	1.045
DOM Efficiency	0.99	no prior	1.09	0.990
cosmic ray spectral shift	0	0±0.05	-0.023	0.051
π/K ratio	1	1±0.1	1.15	1.064
$\nu/\overline{\nu}$ ratio	1	1±0.05	not used	1.00
atmospheric density shift	0	0±0.035	not used	-0.043

Table 5.2: Best fit values for the null hypothesis

Finally, before unblinding, we performed preunblinding tests which consisted on using the null hypothesis, i.e. no sterile neutrino, and perform various tests. There were some important rules: the fit could be formed in the full analysis space, but we could only see either the projected zenith or muon energy proxy distributions and – obviously – no sterile neutrino hypothesis could be tested. The reason for using only the projections was that in the MC test we realized that one could not see the sterile neutrino effect if one would look only at the projection, this guarded us against potential bias. The best fit parameters for the null hypothesis on the pre unblinding test is reported on Table 5.2; no nuisance parameter was found to be in tension with the priors. The one dimensional projections in zenith and energy (see Figure 5.10) were also found to be in good agreement. We further decided to perform other tests. First we split the detector in four azimuthal regions: $[0, \pi]\left[\frac{\pi}{4}, \frac{5\pi}{4}\right]$,$\left[\frac{3\pi}{4}, \frac{7\pi}{4}\right]$,$\left[\frac{\pi}{2}, \frac{3\pi}{2}\right]$, and $\left[\frac{3\pi}{4}, 2\pi\right]$. Then we split the detector into lower and upper parts. For each

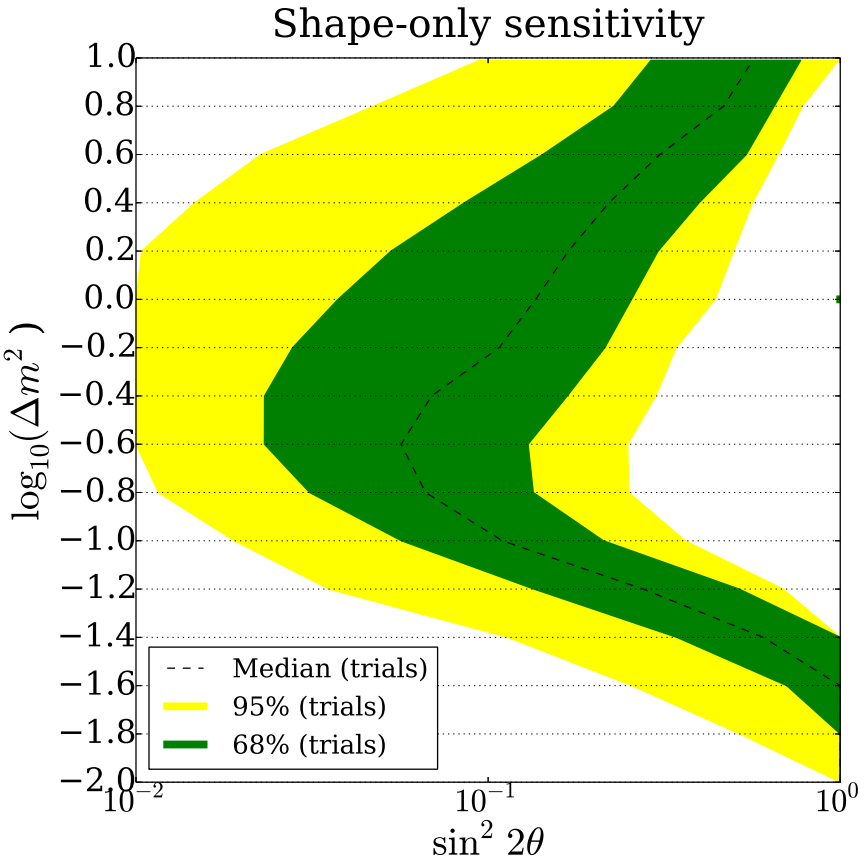

Figure 5.9: IceCube-86 sterile neutrino search 90% C.L. *brazilian* plot sensitivity. The yellow band corresponds to the 95% range, while the green to the 68%. The median sensitivity is shown as a dashed black line.

of these splittings we used the null hypothesis with its full detector nuisance fit values and looked at the event distribution. No significant deviations were observed. After these tests were shown to the collaboration we asked for unblinded permission. Unblinding permission was granted on Thursday, 19^{th} of March, 2015.

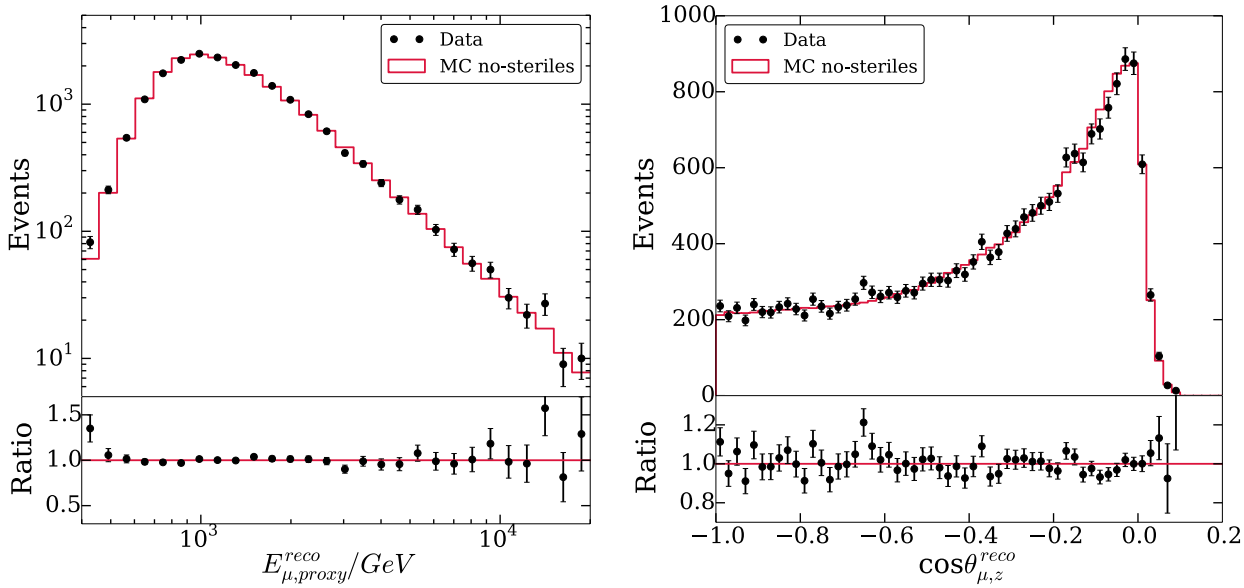

Figure 5.10: One dimensional event distribution prior to unblinding.

5.3.2 Second Stage: opening the box

After been granted permission to unblind we proceeded to make the fit on entire sterile neutrino parameter space: this was a very computationally intense process. We unblinded on Wednesday, 29^{th} of April, 2015 and showed the results to the collaboration, in the upmost secrecy, on the Madison IceCube Collaboration meeting on Friday, 1^{st} of May, 2015. Figure 5.11 shows us on that day.

Figure 5.11: Upper left shows from left to right: Francis Halzen, Gabriel Collins, Janet Conrad, Ben Jones, Carlos Argüelles, and Jordi Salvado. Upper right shows the core of the sterile neutrino search team: Ben Jones, Carlos Argüelles, and Jordi Salvado. Lower panel shows the commemorative champagne bottle of this analysis.

5.3.3 Third Stage: post unblinding discussion

The result of unblinding, assuming Wilk's theorem, is shown in Figure 5.13. The best fit is at $\Delta m^2_{41} = 10$ eV^2 and $\sin^2 2\theta_{24} = 0.56$, with $\Delta \log \mathcal{L}$ from the no sterile hypothesis of 1.91 corresponding to a p-value of 19.4% with respect to the no-sterile hypothesis; the pulls for the later are shown in Figure 5.12. In other words this result is compatible to the null hypothesis within 2σ. It is interesting, though, to ask: where would the minima be located in case the null hypothesis would be true? In Figure 5.14 we show the location of the minima when the null hypothesis is injected in the left panel. The right panel shows the likelihood distribution when the null hypothesis is injected; it is remarkable that Wilk's theorem holds very well when

the null hypothesis is true. The location of the minima in the left panel is not really surprising given the phenomenology of sterile neutrinos.

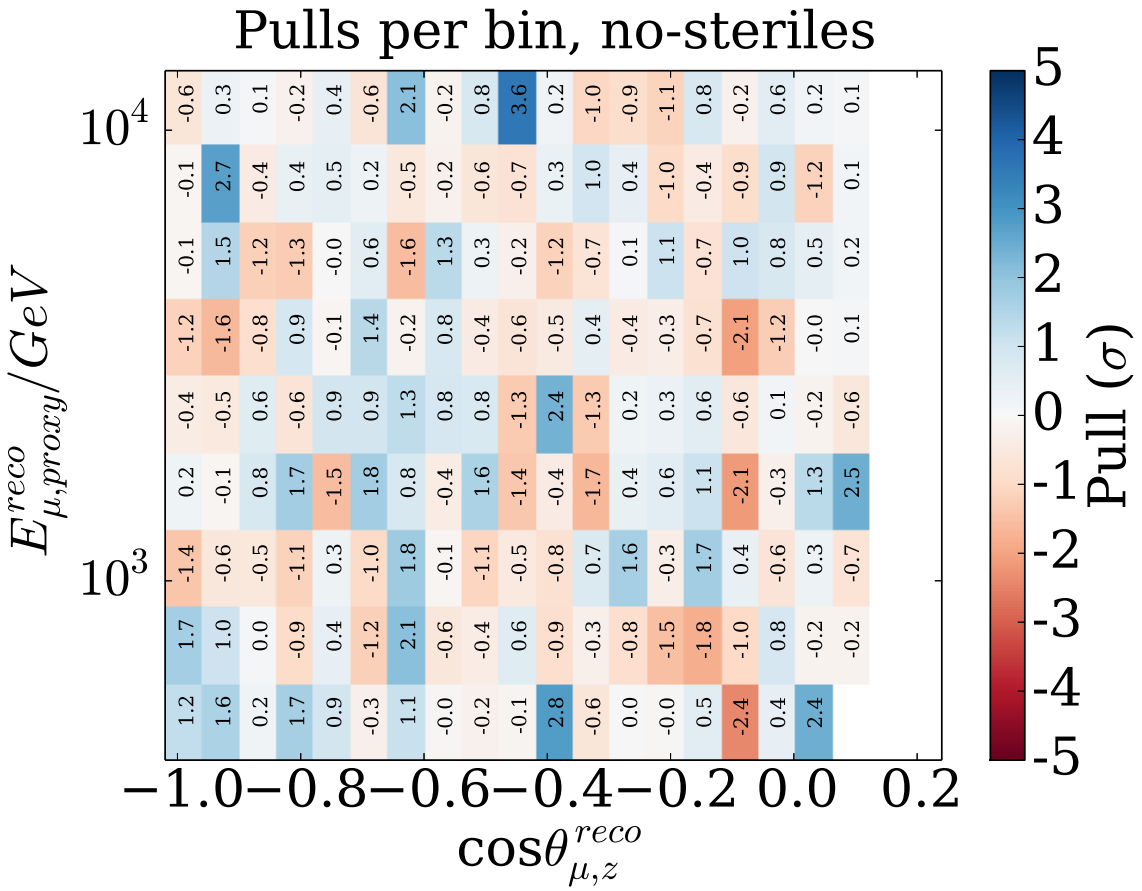

Figure 5.12: The pulls for the null hypothesis are shown as a function of reconstructed quantities.

There are three distinct regions in this space. In the lower right region the sterile neutrino effect is suppress by $\sin^2\left(\Delta m^2_{41} L/E\right)$ so no oscillation effect occurs, i.e. indistinguishable from the null hypothesis. The middle region of the plot, where the *nose* sticks out, is where the MSW resonance happens: this region is disfavored by the data. The upper region is when the resonance condition is no longer met, but fast oscillations are in play. In this later region, given the fast oscillation, it is possible that the fluctuations given by the MC expectation under the sterile hypothesis easily match the data. This is precisely what we see when we inject the data and recover the best fit when using MC, this is shown in Figure 5.14 where we plot the distribution of the location of the likelihood minima when the null hypothesis is injected.

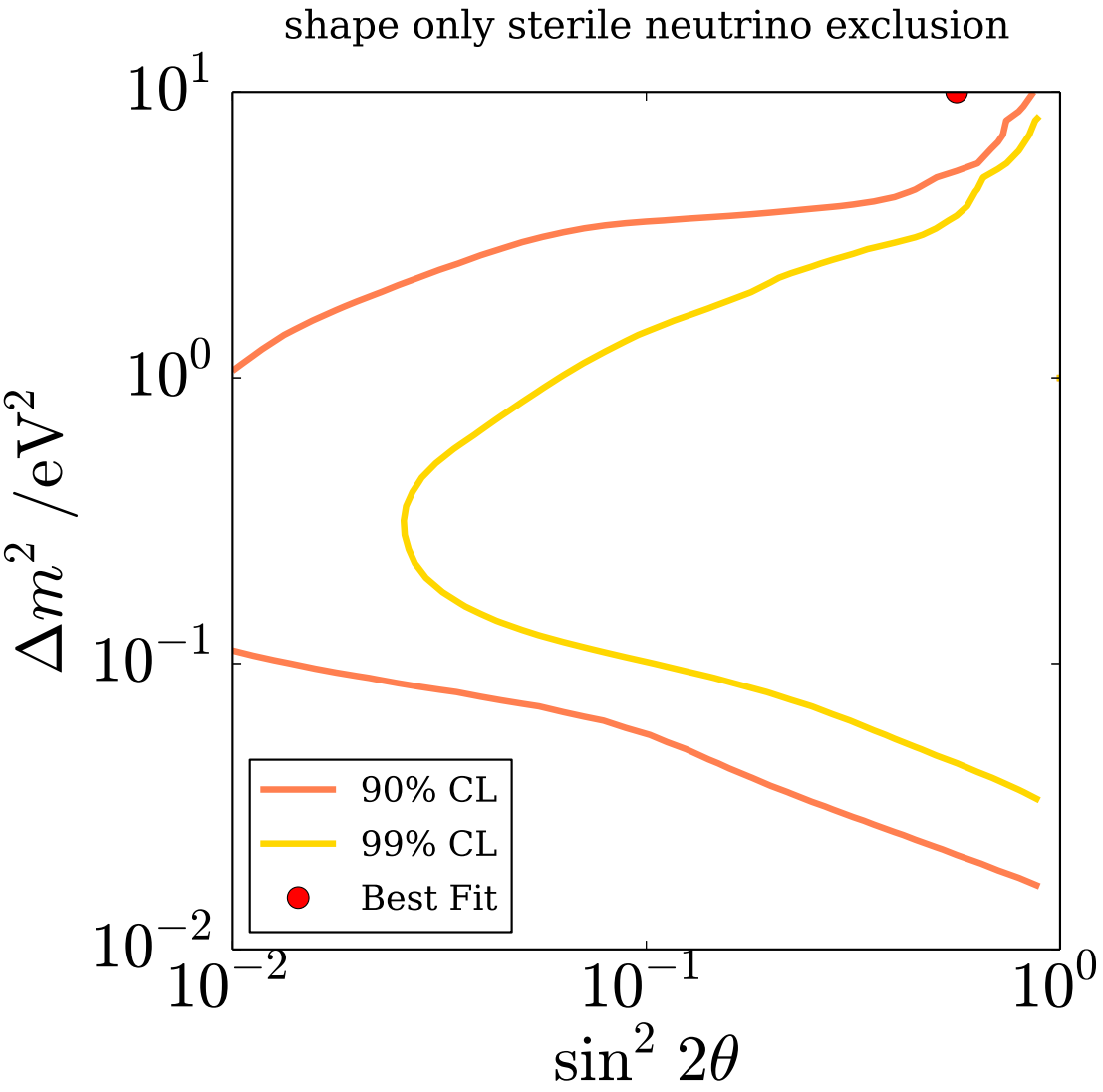

Figure 5.13: Result for the shape only analysis is shown as a function of Δm^2 and $\sin^2 2\theta$. The best fit point is marked with a red dot ($\Delta m^2_{41} = 10$ eV^2 and $\sin^2 2\theta_{24} = 0.56$) with a p-value of 19.4% for the no-sterile hypothesis . The orange (yellow) line corresponds to the 90(99)% C.L. exclusion obtained using Wilk's theorem.

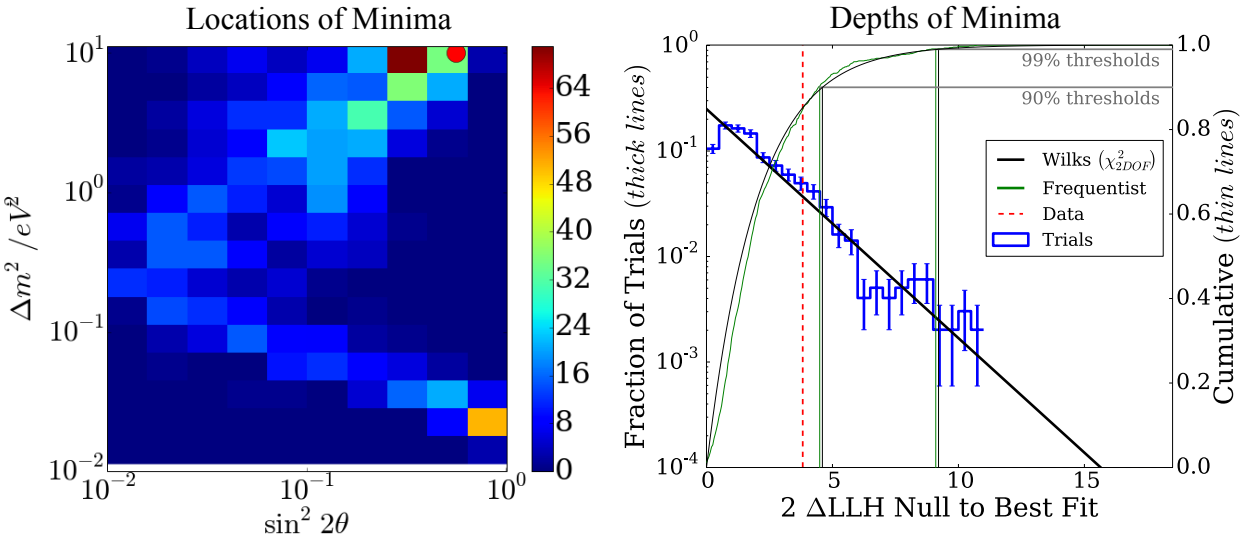

Figure 5.14: The left plot shows the the best fit point location from data challenges in which the null hypothesis is assumed. It can be seen that the region of high mass difference and large mixing angle is often the outcome of minimizing the likelihood problem when the null hypothesis holds. The right plot shows the distribution of log-likelihood differences between the null hypothesis and the best fit in the same data challenges. The solid black line shows Wilk's theorem expectation and the blue data points the data challenge realizations distribution. The green lines mark the likelihood values that correspond to 90% and 99% C.L. obtained from the trials. Finally, the dashed red line corresponds to the log-likelihood value obtained for the data, which translates to a Wilk's p-value of 19.4%.

The previous reasoning implies that at high Δm^2 there is a degeneracy between the null and the alternative hypothesis. The way to break this degeneracy is to introduce a prior in the normalization since the main effect in the high Δm^2 would be to change the survival probability proportional to $\sin^2 2\theta$. It is natural to introduce this post unblinding prior, namely what is the constrain due to the normalization of the atmospheric flux, since for the most extreme values of the mixing angle the normalization nuisance parameter approaches two. Thus we, post unblinding, introduced a prior on the normalization which is gaussian with a spread of 40%. After introducing this prior we obtained the result shown in Figure 5.15, in which the best fit point is now at $\Delta m^2_{41} = 10$ eV^2 and $\sin^2 2\theta_{24} = 0.5$ – rather close to the shape only analysis – with a log-likelihood difference from the null hypothesis of $\Delta \log \mathcal{L} = 0.75$ which corresponds to a p-value of 47.2% from the no-sterile hypothesis. It is easy to notice by comparing Figures 5.13 and 5.15 that the introduction of the normalization prior has reduced the strength of the result. This is to be expected, since the normalization prior and the shape only result best fit point nuisance parameters are in *tension* between each other – namely the normalization on the best fit point is far away from the prior –; this tension in the likelihood problem reduces the significance of the result.

It is interesting to note that if we restrain to the regime of *only* the MSW effect, namely $\Delta m^2 \lesssim 5\text{eV}^2$, a result very close to the rate+shape analysis is obtained, a similar result is obtained if one constructs the likelihood differences with respect to the null hypothesis and rejects negative values on $\Delta\mathcal{L}$, i.e. a Wilk's exclusion limit. All of this reinforces the claim that no MSW inducing sterile neutrino has being found on the IceCube neutrino data. Of course no claims can be performed, as expected from the sensitivity in Figure 5.15, on the higher or lower square mass differences. It is important to point out that restricting the sterile parameter space is not justified and is a severe violation of blindness; also making Wilk's exclusion limits is not an appropriate statistical procedure in this case since one is in a flip-flopping scenario.

Finally, let's go back to the nuisance parameters that we discussed in the previous section. After performing the analysis and corresponding fit, these are shown in Figures 5.16 and 5.17. The left column in this Figure corresponds to the continuos nuisance parameters when constrained to a single model, while the right column contains the nuisance parameters minimized over the discrete models. An important point to make here is that the normalization nuisance parameter goes to very high values in the upper right corner of the plot. This is explained by the degeneracy between the normalization and the fast oscillations amplitude. This plots helps to motivate the introduction of the normalization prior.

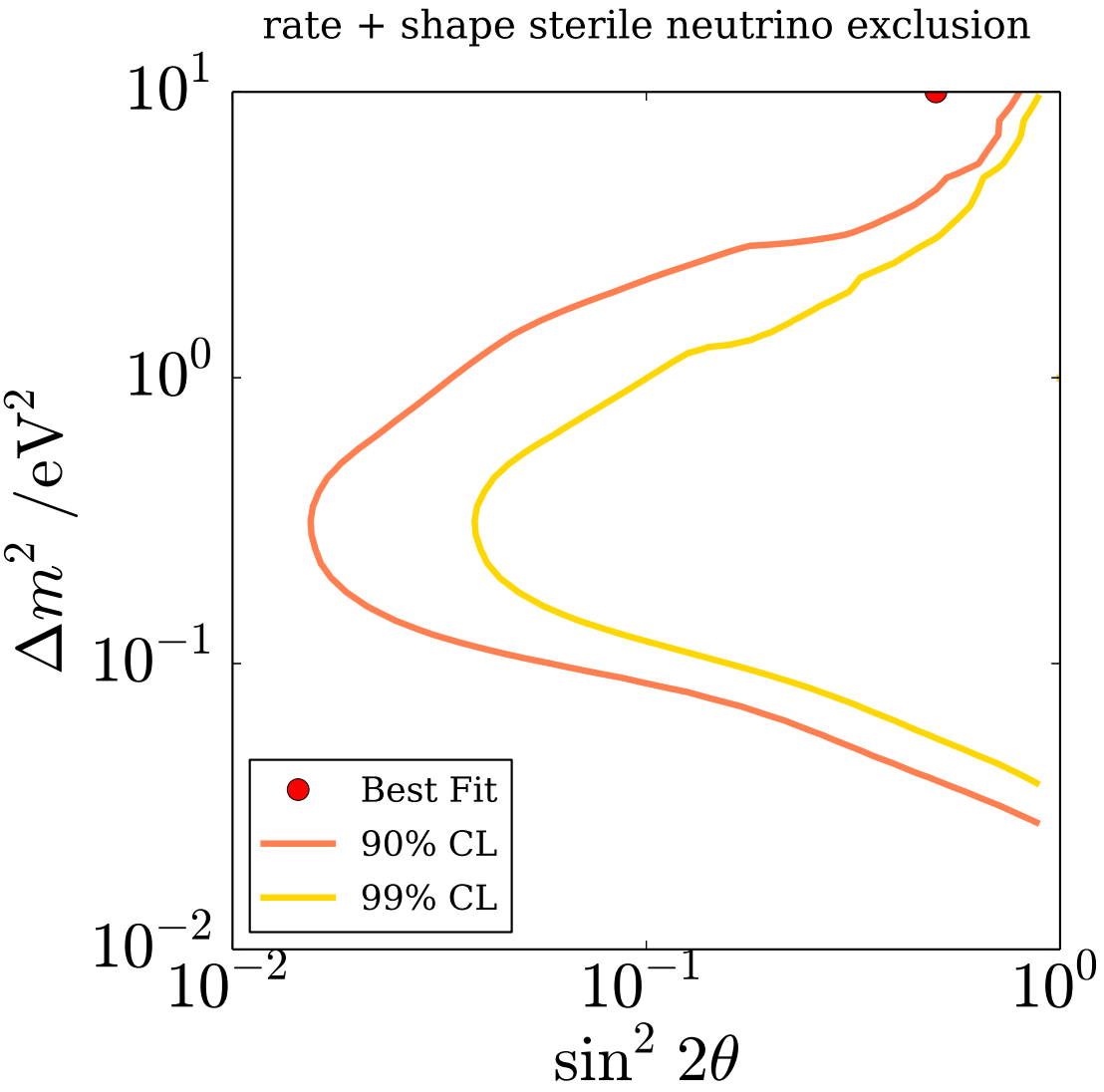

Figure 5.15: Result for the rate + shape analysis is shown as a function of Δm^2 and $\sin^2 2\theta$. The best fit point is marked with a red dot ($\Delta m^2_{41} = 10$ eV^2 and $\sin^2 2\theta_{24} = 0.5$) with a p-value of 47.2% for the no-sterile hypothesis. The orange (yellow) line corresponds to the 90(99)% C.L. exclusion obtained using Wilk's theorem.

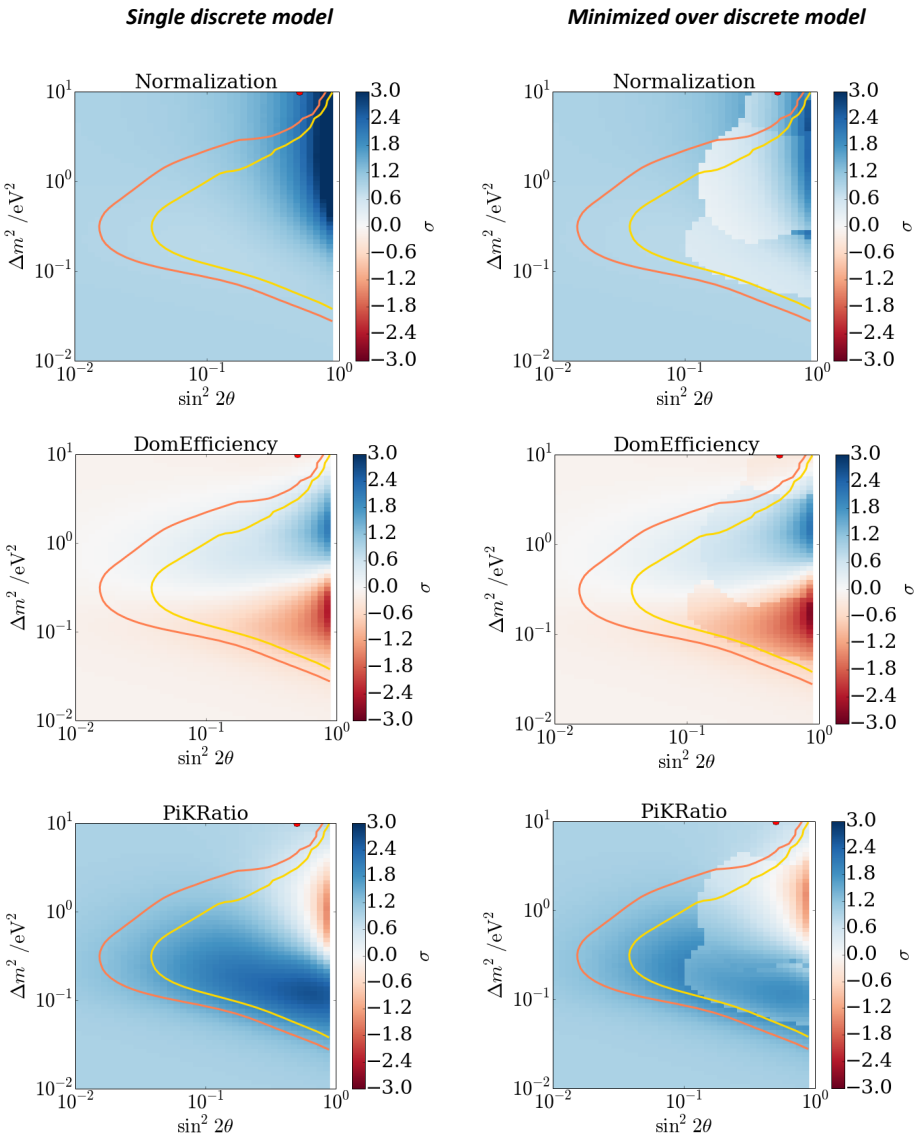

Figure 5.16: Plots shows the pulls of the nuisance parameters as a function of the sterile neutrino parameter space; as a reference the solid orange (yellow) line corresponds to the 90(99)%C.L. shape+rate Wilk's exclusion. In the case of the DOMefficiency, since it does not have a prior, we have plotted the percentage change. Strong deviations from the prior centers can be observed in the region where the MSW signal is strong, and the effect decreases in the parameter space that is compatible with the null hypothesis. The left plots corresponds to the default discrete variation, while the right plots are minimized over the discrete variations. The abrupt changes in value seen in the right plots arises from the sudden change of discrete parameters.

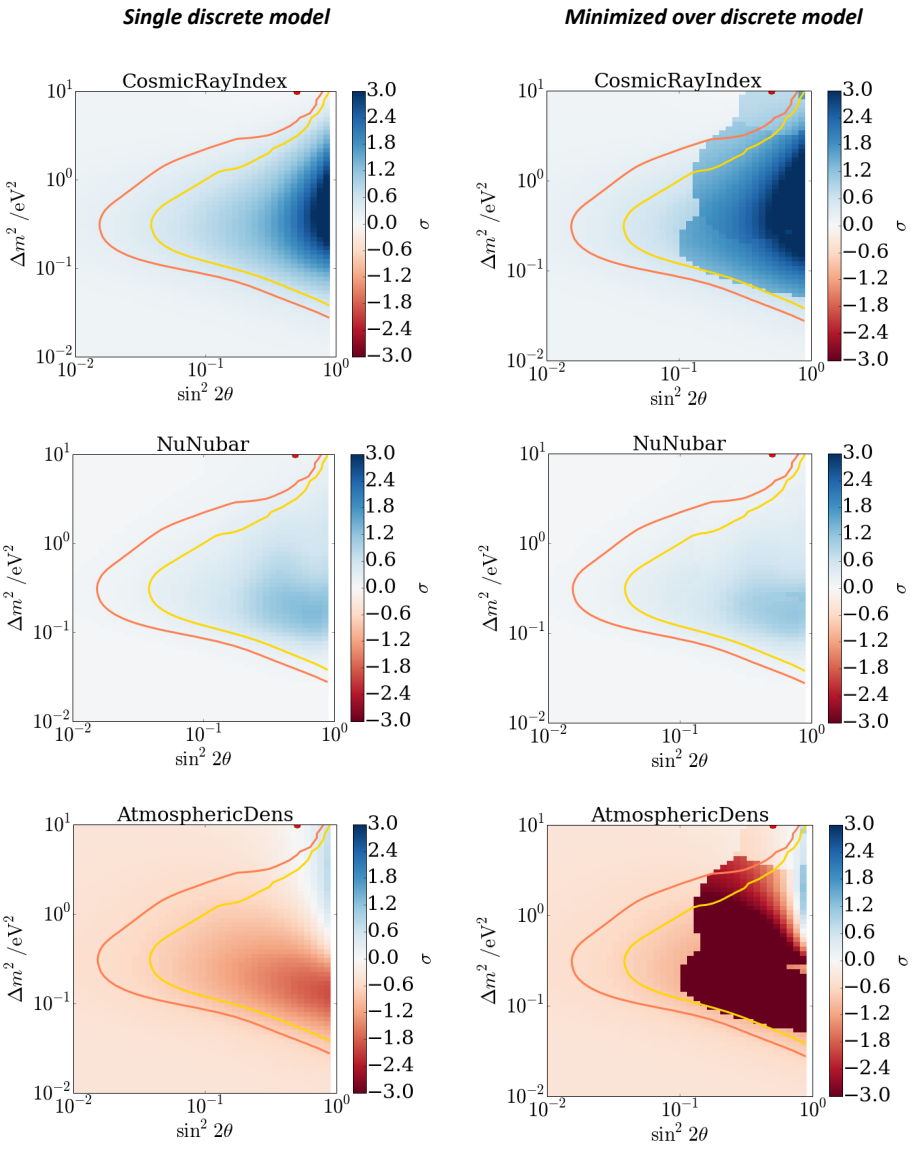

Figure 5.17: Same as Figure 5.16 for the cosmic ray index, nu/nubar, and atmospheric density uncertainty nuisance parameters.

Chapter 6

Conclusion

'Posible, pero no interesante' – respondió Lönnrot–. 'Usted replicará que la realidad no tiene la menor obligación de ser interesante. Yo le replicaré que la realidad puede prescindir de esa obligación, pero no las hipótesis.'

— Jorge Luis Borges, La Muerte y la Brújula.[6]

This work has not concluded. There is still several years more of data to analyze under the sterile neutrino scenario, and we have not even studied the NSI and LV hypothesis. This is the next task. In these next analysis we will reduce significantly statistical errors and further improvements on detector systematics could be included such as precise determination of DOM efficiency and hole ice. Figure 6.1 compares our result with the current appearance and disappearance bounds. It is clear from this image that we have improved the constraints on sterile neutrinos due to neutrino muon survival probability substantially: this increases the tension, see the discussion on 4.1. In essence, as discussed in Section 4.1, we have placed constrains on $|U_{\mu 4}|$, but we need to remember the right panel on that same Figure on which we have ploted the limit on appearance experiments under the assumption $|U_{e4}|^2 = 0.023$ [100]. In this panel Conrad et al. [101] global best fit as well as the Kopp et al. [100] are in tension with this result. An obvious interplay is relaxing $|U_{e4}|^2$, but perhaps a not so obvious possibility is to introduce other angles into the IceCube sterile neutrino fix, in particular it has been noted that θ_{34} and the sterile CP phases may play an important role, see [13]. It is very interesting to consider the case of θ_{34} which, according to the references previously mentioned, diminishes the sterile neutrino resonance at the expense of modifying the atmospheric neutrino measurements. What this tells us is that to properly use the IceCube result we need to perform a global fit

[6] "It's possible, but not interesting," Lönnrot answered. "You will reply that reality hasn't the slightest need to be of interest. And I'll answer you that reality may avoid the obligation to be interesting, but that hypotheses may not."

on the sterile neutrino sensitive data. Thus, for this result to be useful, it is imperative that the IceCube collaboration make available data and MC needed to include this result in the global analysis, in order words a two way interaction between the experiment and the community. *Fin.*

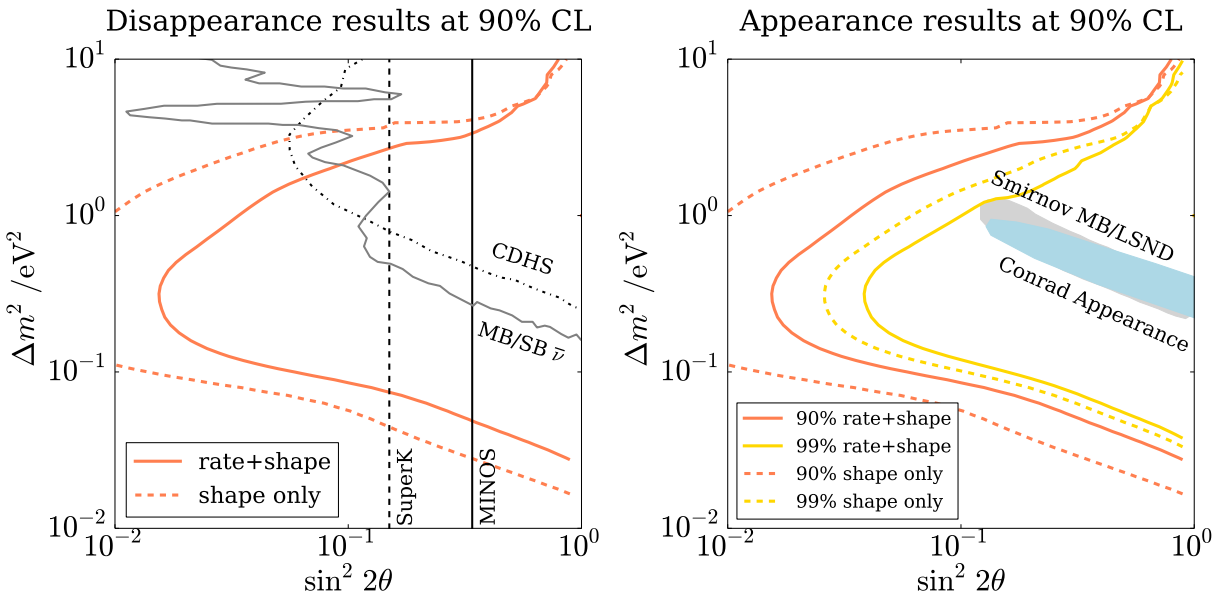

Figure 6.1: Final result compare to the world. Results of the blind analysis – shape only – and post unblinding shape+rate analysis are shown together with disappearance (left) and appearance (right) results.

LIST OF REFERENCES

[1] F. Halzen and A. D. Martin, *QUARKS AND LEPTONS: AN INTRODUCTORY COURSE IN MODERN PARTICLE PHYSICS*. 1984.

[2] J. Beringer *et al.*, "The Review 'of Particle Physics," *Phys. Rev. D*, vol. 86, p. 010001, 2012.

[3] Arg

[4] G. Collins and J. Conrad, "An estimation of systematics for up-going atmospheric neutrino flux at the south pole,"

[5] A. Fedynitch, J. B. Tjus, and P. Desiati, "Influence of hadronic interaction models and the cosmic ray spectrum on the high-energy atmospheric muon and neutrino flux," *EPJ Web Conf.*, vol. 52, p. 09003, 2013.

[6] A. Fedynitch, R. Engel, T. K. Gaisser, F. Riehn, and T. Stanev, "Calculation of conventional and prompt lepton fluxes at very high energy," 2015. [EPJ Web Conf.99,08001(2015)].

[7] C. A. Arguelles Delgado, J. Salvado, and C. N. Weaver, "A Simple Quantum Integro-Differential Solver (SQuIDS)," 2014.

[8] C. A. Arguelles Delgado, J. Salvado, and C. N. Weaver, "ν-SQuIDS." `https://github.com/arguelles/nuSQuIDS`.

[9] J. Kopp, *New phenomena in neutrino physics*. PhD thesis, Heidelberg U., 2009.

[10] A. Esmaili and A. Yu. Smirnov, "Probing Non-Standard Interaction of Neutrinos with IceCube and DeepCore," *JHEP*, vol. 06, p. 026, 2013.

[11] S. Collaboration, "Measurements of d^0 and d^* production in $p+p$ collisions at $\sqrt{s} = 200$ gev," *Phys.Rev. D*, vol. 86, p. 072013, 2012.

[12] A. Esmaili, F. Halzen, and O. L. G. Peres, "Exploring $\nu\_\tau - \nu\_s$ mixing with cascade events in DeepCore," *JCAP*, vol. 1307, p. 048, 2013.

[13] A. Esmaili and A. Yu. Smirnov, "Restricting the LSND and MiniBooNE sterile neutrinos with the IceCube atmospheric neutrino data," *JHEP*, vol. 12, p. 014, 2013.

[14] M. Gonzalez-Garcia, F. Halzen, and M. Maltoni, "Physics reach of high-energy and high-statistics icecube atmospheric neutrino data," *Phys.Rev.*, vol. D71, p. 093010, 2005.

[15] Arg

[16] C. Weaver, *Evidence for Astrophysical Muon Neutrinos from the Northern Sky*. PhD thesis, University of Wisconsin, Madison, 2015.

[17] M. G. Aartsen *et al.*, "Evidence for Astrophysical Muon Neutrinos from the Northern Sky with IceCube," 2015.

[18] A. Cooper-Sarkar, P. Mertsch, and S. Sarkar, "The high energy neutrino cross-section in the standard model and its uncertainty," *JHEP*, vol. 08, 06 2011.

[19] R. D. Ball *et al.*, "Parton distributions for the LHC Run II," *JHEP*, vol. 04, p. 040, 2015.

[20] J. Gao, M. Guzzi, J. Huston, H.-L. Lai, Z. Li, *et al.*, "The CT10 NNLO Global Analysis of QCD," *Phys. Rev.*, vol. D89, p. 033009, 2014.

[21] F. Aaron *et al.*, "Combined measurement and qcd analysis of the inclusive ep scattering cross sections at hera," *JHEP*, 11 2010.

[22] O. Nachtmann, "Positivity constraints for anomalous dimensions," *Nucl. Phys.*, vol. B63, pp. 237–247, 1973.

[23] S. Kretzer and M. H. Reno, "Target mass corrections to electroweak structure functions and perturbative neutrino cross-sections," *Phys. Rev.*, vol. D69, p. 034002, 2004.

[24] V. Bertone, S. Carrazza, and J. Rojo, "APFEL: A PDF Evolution Library with QED corrections," *Comput. Phys. Commun.*, vol. 185, pp. 1647–1668, 2014.

[25] G. Altarelli and G. Parisi, "Asymptotic Freedom in Parton Language," *Nucl.Phys.*, vol. B126, p. 298, 1977.

[26] Y. Dokshitzer *Sov.Phys. JETP*, vol. 46, p. 641, 1977.

[27] V. Gribov and L. Lipatov *Sov. J. Nucl. Phys.*, vol. 15, p. 438, 1972.

[28] M. Froissart, "Asymptotic behavior and subtractions in the mandelstam representation," *Physical Review*, vol. 123, no. 3, pp. 1053–1057, 1961.

[29] M. M. Block, "Hadronic forward scattering: Predictions for the Large Hadron Collider and cosmic rays," *Phys.Rept.*, vol. 436, pp. 71–215, 2006.

[30] M. M. Block and F. Halzen, "Experimental confirmation that the proton is asymptotically a black disk," *Phys.Rev.Lett.*, vol. 107, p. 212002, 09 2011.

[31] M. M. Block and F. Halzen, "Evidence for the saturation of the froissart bound," *Phys.Rev.*, vol. D70, p. 091901, 2004.

[32] M. M. Block and F. Halzen, "New experimental evidence that the proton develops asymptotically into a black disk," *Phys.Rev.*, vol. D86, p. 051504, 2012.

[33] P. Abreu *et al.*, "Ultrahigh energy neutrinos at the pierre auger observatory," *Advances in High Energy Physics*, vol. 2013, 04 2013.

[34] M. M. Block, F. Halzen, G. Pancheri, and T. Stanev, "Breaking the barriers—uniting accelerator and cosmic ray p-p cross sections," 1999.

[35] M. Block, F. Halzen, and T. Stanev, "Extending the frontiers: Reconciling accelerator and cosmic ray pâĹŠp cross sections," *Phys.Rev. D*, vol. 62, no. 7, 2000.

[36] N. N. Nikolaev and B. Zakharov, "Color transparency and scaling properties of nuclear shadowing in deep inelastic scattering," *Z.Phys.*, vol. C49, pp. 607–618, 1991.

[37] N. N. Nikolaev and B. Zakharov, "The Triple pomeron regime and the structure function of the pomeron in the diffractive deep inelastic scattering at very small x," *Z.Phys.*, vol. C64, pp. 631–652, 1994.

[38] A. H. Mueller, "Soft gluons in the infinite momentum wave function and the BFKL pomeron," *Nucl.Phys.*, vol. B415, pp. 373–385, 1994.

[39] A. H. Mueller and B. Patel, "Single and double BFKL pomeron exchange and a dipole picture of high-energy hard processes," *Nucl.Phys.*, vol. B425, pp. 471–488, 1994.

[40] K. Golec-Biernat and M. Wusthoff, "Saturation effects in deep inelastic scattering at low q^2 and its implications on diffraction," *Phys.Rev.*, vol. D59, p. 014017, 1998.

[41] E. Iancu, K. Itakura, and S. Munier, "Saturation and BFKL dynamics in the HERA data at small x," *Phys.Lett.*, vol. B590, pp. 199–208, 2004.

[42] V. Barone, M. Genovese, N. Nikolaev, E. Predazzi, and B. Zakharov, "Longitudinal structure functions," *Physics Letters B*, vol. 304, no. 1ââĆň"2, pp. 176 – 182, 1993.

[43] K. Kutak and J. Kwiecinski, "Screening effects in the ultrahigh-energy neutrino interactions," *Eur.Phys.J.*, vol. C29, p. 521, 2003.

[44] E. M. Henley and J. Jalilian-Marian, "Ultra-high energy neutrino-nucleon scattering and parton distributions at small x," *Phys.Rev.D73:094004,2006; AIPConf.Proc.*, vol. 870, pp. 666–668, 2006.

[45] M. M. Block, L. Durand, and P. Ha, "Connection of virtual $\gamma^* p$ cross sections of ep deep inelastic scattering to real γp scattering, and the implications forνn and ep total cross sections," *Phys.Rev.*, vol. D89, p. 094027, 04 2014.

[46] Y. S. Jeong and M. H. Reno, "Quark mass effects in high energy neutrino nucleon scattering," *Phys.Rev.*, vol. D81, p. 114012, 2010.

[47] P. Jimenez-Delgado and E. Reya, "Variable Flavor Number Parton Distributions and Weak Gauge and Higgs Boson Production at Hadron Colliders at NNLO of QCD," *Phys.Rev.*, vol. D80, p. 114011, 2009.

[48] A. Connolly, R. S. Thorne, and D. Waters, "Calculation of High Energy Neutrino-Nucleon Cross Sections and Uncertainties Using the MSTW Parton Distribution Functions and Implications for Future Experiments," *Phys.Rev.*, vol. D83, p. 113009, 2011.

[49] R. Mohapatra, S. Antusch, K. Babu, G. Barenboim, M.-C. Chen, S. Davidson, A. de Gouvea, P. de Holanda, B. Dutta, Y. Grossman, A. Joshipura, B. Kayser, J. Kersten, Y. Keum, S. King, P. Langacker, M. Lindner, W. Loinaz, I. Masina, I. Mocioiu, S. Mohanty, H. Murayama, S. Pascoli, S. Petcov, A. Pilaftsis, P. Ramond, M. Ratz, W. Rodejohann, R. Shrock, T. Takeuchi, T. Underwood, and L. Wolfenstein, "Theory of neutrinos: A white paper," 2005.

[50] A. de Gouvea, K. Pitts, K. Scholberg, G. Zeller, J. Alonso, A. Bernstein, M. Bishai, S. Elliott, K. Heeger, K. Hoffman, P. Huber, L. Kaufman, B. Kayser, J. Link, C. Lunardini, B. Monreal, J. Morfin, H. Robertson, R. Tayloe, N. Tolich, K. Abazajian, T. Akiri, C. Albright, J. Asaadi, K. Babu, A. Balantekin, P. Barbeau, M. Bass, A. Blake, A. Blondel, E. Blucher, N. Bowden, S. Brice, A. Bross, B. Carls, F. Cavanna, B. Choudhary, P. Coloma, A. Connolly, J. Conrad, M. Convery, R. Cooper, D. Cowen, H. da Motta, T. de Young, F. D. Lodovico, M. Diwan, Z. Djurcic, M. Dracos, S. Dodelson, Y. Efremenko, T. Ekelof, J. Feng, B. Fleming, J. Formaggio, A. Friedland, G. Fuller, H. Gallagher, S. Geer, M. Gilchriese, M. Goodman, D. Grant, G. Gratta, C. Hall, F. Halzen, D. Harris, M. Heffner, and et al. (100 additional authors not shown), "Neutrinos," 10 2013.

[51] B. Pontecorvo, "Neutrino Experiments and the Problem of Conservation of Leptonic Charge," *Sov.Phys.JETP*, vol. 26, pp. 984–988, 1968.

[52] V. Gribov and B. Pontecorvo, "Neutrino astronomy and lepton charge," *Phys.Lett.*, vol. B28, p. 493, 1969.

[53] M. Fukugita and T. Yanagida, *Physics of Neutrinos: And Applications to Astrophysics*. Physics and astronomy online library, Springer, 2003.

[54] E. K. Akhmedov, "Neutrino physics," pp. 103–164, 1999.

[55] A. B. Balantekin and W. C. Haxton, "Neutrino oscillations," 03 2013.

[56] M. Gonzalez-Garcia and M. Maltoni, "Phenomenology with Massive Neutrinos," *Phys.Rept.*, vol. 460, pp. 1–129, 2008.

[57] M. Gonzalez-Garcia, M. Maltoni, and T. Schwetz, "Updated fit to three neutrino mixing: status of leptonic CP violation," 2014.

[58] J. Hewett, H. Weerts, R. Brock, J. Butler, B. Casey, J. Collar, A. de Gouvea, R. Essig, Y. Grossman, W. Haxton, J. Jaros, C. Jung, Z. Lu, K. Pitts, Z. Ligeti, J. Patterson, M. Ramsey-Musolf, J. Ritchie, A. Roodman, K. Scholberg, C. Wagner, G. Zeller, S. Aefsky, A. Afanasev, K. Agashe, C. Albright, J. Alonso, C. Ankenbrandt, M. Aoki, C. Arguelles, N. Arkani-Hamed, J. Armendariz, C. Armendariz-Picon, E. A. Diaz, J. Asaadi, D. Asner, K. Babu, K. Bailey, O. Baker, B. Balantekin, B. Baller, M. Bass, B. Batell, J. Beacham, J. Behr, N. Berger, M. Bergevin, E. Berman, R. Bernstein, A. Bevan, M. Bishai, M. Blanke, S. Blessing, A. Blondel, T. Blum, G. Bock, A. Bodek, G. Bonvicini, F. Bossi, J. Boyce, R. Breedon, M. Breidenbach, S. Brice, R. Briere, S. Brodsky, and et al. (403 additional authors not shown), "Fundamental physics at the intensity frontier," 05 2012.

[59] A. Aguilar, L. Auerbach, R. Burman, D. Caldwell, E. Church, A. Cochran, J. Donahue, A. Fazely, G. Garvey, R. Gunasingha, R. Imlay, W. Louis, R. Majkic, A. Malik, W. Metcalf, G. Mills, V. Sandberg, D. Smith, I. Stancu, M. Sung, R. Tayloe, G. VanDalen, W. Vernon, N. Wadia, D. White, and S. Yellin, "Evidence for neutrino oscillations from the observation of electron anti-neutrinos in a muon anti-neutrino beam," 2001.

[60] G. Mention, M. Fechner, T. Lasserre, T. A. Mueller, D. Lhuillier, M. Cribier, and A. Letourneau, "The reactor antineutrino anomaly," 01 2011.

[61] MiniBooNE-Collaboration, A. A. Aguilar-Arevalo, B. C. Brown, L. Bugel, G. Cheng, E. D. Church, J. M. Conrad, R. Dharmapalan, Z. Djurcic, D. A. Finley, R. Ford, F. G. Garcia, G. T. Garvey, J. Grange, W. Huelsnitz, C. Ignarra, R. Imlay, R. A. Johnson, G. Karagiorgi, T. Katori, T. Kobilarcik, W. C. Louis, C. Mariani, W. Marsh, G. B. Mills, J. Mirabal, C. D. Moore, J. Mousseau, P. Nienaber, B. Osmanov, Z. Pavlovic, D. Perevalov, C. C. Polly, H. Ray, B. P. Roe, A. D. Russell, M. H. Shaevitz, J. Spitz, I. Stancu, R. Tayloe, R. G. V. de Water, D. H. White, D. A. Wickremasinghe, G. P. Zeller, and E. D. Zimmerman, "A combined $\to_e$ and $^- \to ^-_e$ oscillation analysis of the miniboone excesses," 07 2012.

[62] J. Kopp, P. A. Machado, M. Maltoni, and T. Schwetz, "Sterile neutrino oscillations: the global picture," *Journal of High Energy Physics*, vol. 2013, no. 5, pp. 1–52, 2013.

[63] J. M. Conrad, W. C. Louis, and M. H. Shaevitz, "The lsnd and miniboone oscillation searches at high m^2," 06 2013.

[64] K. N. Abazajian, M. A. Acero, S. K. Agarwalla, A. A. Aguilar-Arevalo, C. H. Albright, S. Antusch, C. A. Argüelles, A. B. Balantekin, G. Barenboim, V. Barger, P. Bernardini, F. Bezrukov, O. E. Bjaelde, S. A. Bogacz, N. S. Bowden, A. Boyarsky, A. Bravar, D. B. Berguno, S. J. Brice, A. D. Bross, B. Caccianiga, F. Cavanna, E. J. Chun, B. T. Cleveland, A. P. Collin, P. Coloma, J. M. Conrad, M. Cribier, A. S. Cucoanes, J. C. D'Olivo, S. Das, A. de Gouvea, A. V. Derbin, R. Dharmapalan, J. S. Diaz, X. J. Ding, Z. Djurcic, A. Donini, D. Duchesneau, H. Ejiri, S. R. Elliott, D. J. Ernst, A. Esmaili, J. J. Evans, E. Fernandez-Martinez, E. Figueroa-Feliciano, B. T. Fleming, J. A. Formaggio, D. Franco, J. Gaffiot, R. Gandhi, Y. Gao, G. T. Garvey, V. N. Gavrin, P. Ghoshal, D. Gibin, C. Giunti, S. N. Gninenko, and et al. (129 additional authors not shown), "Light sterile neutrinos: A white paper," 04 2012.

[65] J. Kopp and J. Welter, "The not-so-sterile 4th neutrino: Constraints on new gauge interactions from neutrino oscillation experiments," 08 2014.

[66] M. Pospelov, "Neutrino physics with dark matter experiments and the signature of new baryonic neutral currents," 03 2011.

[67] M. Archidiacono, N. Fornengo, S. Gariazzo, C. Giunti, S. Hannestad, and M. Laveder, "Light sterile neutrinos after bicep-2," 04 2014.

[68] B. Dasgupta and J. Kopp, "A ménage à trois of ev-scale sterile neutrinos, cosmology, and structure formation," 10 2013.

[69] N. Saviano, O. Pisanti, G. Mangano, and A. Mirizzi, "Unveiling secret interactions among sterile neutrinos with big-bang nucleosynthesis," 09 2014.

[70] C. A. Argüelles Delgado and J. Salvado Serra, "A simple quantum integro differential solver (squids)," 2014.

[71] S. Mikheev and A. Y. Smirnov, "Resonance Amplification of Oscillations in Matter and Spectroscopy of Solar Neutrinos," *Sov.J.Nucl.Phys.*, vol. 42, pp. 913–917, 1985.

[72] S. Mikheev and A. Y. Smirnov, "Resonant amplification of neutrino oscillations in matter and solar neutrino spectroscopy," *Nuovo Cim.*, vol. C9, pp. 17–26, 1986.

[73] L. Wolfenstein, "Neutrino Oscillations in Matter," *Phys.Rev.*, vol. D17, pp. 2369–2374, 1978.

[74] H. Duan, G. M. Fuller, and Y.-Z. Qian, "Collective neutrino oscillations," 01 2010.

[75] P. Strack and A. Burrows, "Generalized boltzmann formalism for oscillating neutrinos," 2005.

[76] Y. Zhang and A. Burrows, "Transport equations for oscillating neutrinos," 10 2013.

[77] M. Cirelli, N. Fornengo, T. Montaruli, I. Sokalski, A. Strumia, and F. Vissani, "Spectra of neutrinos from dark matter annihilations," 2005.

[78] M. Blennow, J. Edsjo, and T. Ohlsson, "Neutrinos from WIMP annihilations using a full three-flavor Monte Carlo," *JCAP*, vol. 0801, p. 021, 2008.

[79] C. A. Argüelles and J. Kopp, "Sterile neutrinos and indirect dark matter searches in IceCube," *JCAP*, vol. 1207, p. 016, 2012.

[80] M. Gonzalez-Garcia, F. Halzen, and M. Maltoni, "Physics reach of high-energy and high-statistics icecube atmospheric neutrino data," *Phys.Rev.*, vol. D71, p. 093010, 2005.

[81] F. Halzen and D. Saltzberg, "Tau neutrino appearance with a 1000 megaparsec baseline," 1998.

[82] P. Gondolo, G. Ingelman, and M. Thunman, "Charm production and high-energy atmospheric muon and neutrino fluxes," *Astropart. Phys.*, vol. 5, pp. 309–332, 1996.

[83] T. K. Gaisser, T. Stanev, and S. Tilav, "Cosmic Ray Energy Spectrum from Measurements of Air Showers," *Front.Phys.China*, vol. 8, pp. 748–758, 2013.

[84] V. I. Zatsepin and N. V. Sokolskaya, "Three component model of cosmic ray spectra from 100-gev up to 100-pev," *Astron. Astrophys.*, vol. 458, pp. 1–5, 2006.

[85] J. R. Hoerandel, "On the knee in the energy spectrum of cosmic rays," *Astropart. Phys.*, vol. 19, pp. 193–220, 2003.

[86] S. Ostapchenko, "Monte Carlo treatment of hadronic interactions in enhanced Pomeron scheme: I. QGSJET-II model," *Phys. Rev.*, vol. D83, p. 014018, 2011.

[87] R. S. Fletcher, T. K. Gaisser, P. Lipari, and T. Stanev, "SIBYLL: An Event generator for simulation of high-energy cosmic ray cascades," *Phys. Rev.*, vol. D50, pp. 5710–5731, 1994.

[88] AIRS / AMSU / HSB, "Version 6 level 3 product user guide, version 1.2, jet propulsion laboratory." `http://airs.jpl.nasa.gov/`.

[89] A. Fedynitch, "MCeq." `https://github.com/afedynitch/MCEq`.

[90] T. Sanuki, M. Honda, T. Kajita, K. Kasahara, and S. Midorikawa, "Study of cosmic ray interaction model based on atmospheric muons for the neutrino flux calculation," *Phys. Rev.*, vol. D75, p. 043005, 2007.

[91] M. Honda, T. Kajita, K. Kasahara, S. Midorikawa, and T. Sanuki, "Calculation of atmospheric neutrino flux using the interaction model calibrated with atmospheric muon data," *Phys. Rev.*, vol. D75, p. 043006, 2007.

[92] U. S. C. on Extension to the Standard Atmosphere, *U.S. standard atmosphere, 1976*. National Oceanic and Amospheric [sic] Administration : for sale by the Supt. of Docs., U.S. Govt. Print. Off., 1976.

[93] N. N. Nikolaev, G. Piller, and B. Zakharov, "Quantum coherence in heavy flavor production on nuclei," *J.Exp.Theor.Phys.*, vol. 81, pp. 851–859, 1995.

[94] N. N. Nikolaev, G. Piller, and B. Zakharov, "Inclusive heavy flavor production from nuclei," *Z.Phys.*, vol. A354, pp. 99–105, 1996.

[95] A. Bhattacharya, R. Enberg, M. H. Reno, I. Sarcevic, and A. Stasto, "Perturbative charm production and the prompt atmospheric neutrino flux in light of RHIC and LHC," 2015.

[96] S. Schael *et al.*, "Precision electroweak measurements on the Z resonance," *Phys. Rept.*, vol. 427, pp. 257–454, 2006.

[97] A. Aguilar-Arevalo *et al.*, "Evidence for neutrino oscillations from the observation of anti-neutrino(electron) appearance in a anti-neutrino(muon) beam," *Phys. Rev.*, vol. D64, p. 112007, 2001.

[98] K. Abazajian, M. Acero, S. Agarwalla, A. Aguilar-Arevalo, C. Albright, *et al.*, "Light Sterile Neutrinos: A White Paper," 2012.

[99] P. A. R. Ade *et al.*, "Planck 2015 results. XIII. Cosmological parameters," 2015.

[100] J. Kopp, P. A. N. Machado, M. Maltoni, and T. Schwetz, "Sterile Neutrino Oscillations: The Global Picture," *JHEP*, vol. 1305, p. 050, 2013.

[101] J. Conrad, C. Ignarra, G. Karagiorgi, M. Shaevitz, and J. Spitz, "Sterile Neutrino Fits to Short Baseline Neutrino Oscillation Measurements," *Adv.High Energy Phys.*, vol. 2013, p. 163897, 2013.

[102] A. A. Aguilar-Arevalo *et al.*, "Event Excess in the MiniBooNE Search for $\bar{\nu}_\mu \to \bar{\nu}_e$ Oscillations," *Phys. Rev. Lett.*, vol. 105, p. 181801, 2010.

[103] T. A. Mueller *et al.*, "Improved Predictions of Reactor Antineutrino Spectra," *Phys. Rev.*, vol. C83, p. 054615, 2011.

[104] F. Kaether, W. Hampel, G. Heusser, J. Kiko, and T. Kirsten, "Reanalysis of the GALLEX solar neutrino flux and source experiments," *Phys. Lett.*, vol. B685, pp. 47–54, 2010.

[105] J. N. Abdurashitov *et al.*, "Measurement of the solar neutrino capture rate with gallium metal. III: Results for the 2002–2007 data-taking period," *Phys. Rev.*, vol. C80, p. 015807, 2009.

[106] C. Giunti and M. Laveder, "Statistical Significance of the Gallium Anomaly," *Phys. Rev.*, vol. C83, p. 065504, 2011.

[107] G. Mention, M. Fechner, T. Lasserre, T. A. Mueller, D. Lhuillier, M. Cribier, and A. Letourneau, "The Reactor Antineutrino Anomaly," *Phys. Rev.*, vol. D83, p. 073006, 2011.

[108] K. Abe *et al.*, "Limits on sterile neutrino mixing using atmospheric neutrinos in Super-Kamiokande," *Phys. Rev.*, vol. D91, p. 052019, 2015.

[109] P. Adamson *et al.*, "Search for sterile neutrino mixing in the MINOS long baseline experiment," *Phys. Rev.*, vol. D81, p. 052004, 2010.

[110] P. Adamson *et al.*, "Active to sterile neutrino mixing limits from neutral-current interactions in MINOS," *Phys. Rev. Lett.*, vol. 107, p. 011802, 2011.

[111] L. Wolfenstein, "Neutrino Oscillations in Matter," *Phys.Rev.*, vol. D17, pp. 2369–2374, 1978.

[112] S. Choubey and T. Ohlsson, "Bounds on Non-Standard Neutrino Interactions Using PINGU," *Phys. Lett.*, vol. B739, pp. 357–364, 2014.

[113] V. De Sabbata and M. Gasperini, "Neutrino Oscillations in the Presence of Torsion," *Nuovo Cim.*, vol. A65, pp. 479–500, 1981.

[114] V. A. Kostelecky and M. Mewes, "Lorentz and CPT violation in neutrinos," *Phys.Rev.*, vol. D69, p. 016005, 2004.

[115] V. D. Barger, S. Pakvasa, T. J. Weiler, and K. Whisnant, "CPT odd resonances in neutrino oscillations," *Phys.Rev.Lett.*, vol. 85, pp. 5055–5058, 2000.

[116] S. R. Coleman and S. L. Glashow, "High-energy tests of Lorentz invariance," *Phys.Rev.*, vol. D59, p. 116008, 1999.

[117] M. Gasperini, "Experimental Constraints on a Minimal and Nonminimal Violation of the Equivalence Principle in the Oscillations of Massive Neutrinos," *Phys.Rev.*, vol. D39, pp. 3606–3611, 1989.

[118] S. Glashow, A. Halprin, P. Krastev, C. N. Leung, and J. T. Pantaleone, "Comments on neutrino tests of special relativity," *Phys.Rev.*, vol. D56, pp. 2433–2434, 1997.

[119] M. Butler, S. Nozawa, R. Malaney, and A. Boothroyd, "Gravitationally induced neutrino oscillations," *Phys.Rev.*, vol. D47, pp. 2615–2618, 1993.

[120] V. A. Kostelecky and N. Russell, "Data Tables for Lorentz and CPT Violation," *Rev.Mod.Phys.*, vol. 83, pp. 11–31, 2011.

[121] K. Abe *et al.*, "Test of Lorentz invariance with atmospheric neutrinos," *Phys.Rev.*, vol. D91, no. 5, p. 052003, 2015.

[122] R. Abbasi *et al.*, "Search for a Lorentz-violating sidereal signal with atmospheric neutrinos in IceCube," *Phys.Rev.*, vol. D82, p. 112003, 2010.

[123] J. S. Diaz, "Correspondence between nonstandard interactions and CPT violation in neutrino oscillations," 2015.

[124] M. Gonzalez-Garcia, "Global analyses of oscillation neutrino experiments," *Phys.Dark Univ.*, vol. 4, pp. 1–5, 2014.

[125] L. J. Hall, H. Murayama, and N. Weiner, "Neutrino mass anarchy," *Phys.Rev.Lett.*, vol. 84, pp. 2572–2575, 2000.

[126] N. Haba and H. Murayama, "Anarchy and hierarchy," *Phys.Rev.*, vol. D63, p. 053010, 2001.

[127] A. de Gouvea and H. Murayama, "Neutrino Mixing Anarchy: Alive and Kicking," 2012.

[128] A. de Gouvea and H. Murayama, "Statistical test of anarchy," *Phys.Lett.*, vol. B573, pp. 94–100, 2003.

[129] M. G. Aartsen *et al.*, "Energy Reconstruction Methods in the IceCube Neutrino Telescope," *JINST*, vol. 9, p. P03009, 2014.

[130] G. J. Feldman and R. D. Cousins, "Unified approach to the classical statistical analysis of small signals," *Phys. Rev. D*, vol. 57, pp. 3873–3889, Apr 1998.

[131] S. S. Wilks, "The large-sample distribution of the likelihood ratio for testing composite hypotheses," *Ann. Math. Statist.*, vol. 9, pp. 60–62, 03 1938.

[132] A. Ishihara and K. Hoshina, "neutrino-generator." http://code.icecube.wisc.edu/svn/projects/neutrino-generator/trunk/?p=122347.

[133] A. Gazizov and M. Kowalski, "Anis: High energy neutrino generator for neutrino telescopes," *Computer Physics Communications*, vol. 172, no. 3, pp. 203 – 213, 2005.

[134] C. Weaver, "MuonInjector." http://code.icecube.wisc.edu/projects/icecube/browser/IceCube/sandbox/cweaver/MuonInjector.

[135] C. Weaver, "LeptonInjector." http://code.icecube.wisc.edu/projects/icecube/browser/IceCube/sandbox/cweaver/LeptonInjector.

[136] C. A. Arguelles Delgado, M. Kroll, F. Halzen, and J. Tjus, "New NNLO calculation of the high energy neutrino cross section with LHC pdfs." In preparation.

[137] J.-H. Koehne, K. Frantzen, M. Schmitz, and T. Fuchs, "PROPOSAL." http://code.icecube.wisc.edu/svn/projects/PROPOSAL/trunk/?p=121665.

[138] J.-H. Koehne, K. Frantzen, M. Schmitz, T. Fuchs, W. Rhode, D. Chirkin, and J. Beckerr Tjus, "PROPOSAL: A tool for propagation of charged leptons," *Computer Physics Communications*, vol. 184, pp. 2070–2090, Sept. 2013.

[139] D. Chirkin and W. Rhode, "Muon Monte Carlo: A High-precision tool for muon propagation through matter," 2004.

[140] D. Chirkin and W. Rhode, "Muon Monte Carlo: A High-precision tool for muon propagation through matter," 2004.

[141] B. Voigt, "CMC."

[142] C. Kopper, "CLSim." http://code.icecube.wisc.edu/svn/projects/clsim/trunk?p=121994.

[143] D. Chirkin, "PPC." http://code.icecube.wisc.edu/svn/projects/ppc/trunk.

APPENDIX
The NuFSGen Monte Carlo

The NuFSGen Monte Carlo (MC) chain was specifically designed for the IceCube sterile analysis and, with respect to the standard IceCube NuGen [132] MC – similar to ANIS [133] –, it provides finer control of systematic effects, greater flexibility, and improved statistics. Here the production chain will be briefly described and then the MC weighting procedure will be presented. The MC events discussed in appendix are included as part as a digital appendix as well as the IceCube events that have form part of the analysis presented in this thesis.

A.1 Monte Carlo Chain

The Monte Carlo chain starts by generating events using MuonInjector [134], which is a prototype version of the more general LeptonInjector [135]. Since the analysis selects for muon tracks the topology to be generated is that of a ν_μ charge current interaction. MuonInjector creates a muon-*hadrons*[1] that would be later propagated by the IceCube software. A total energy, E_ν, is assigned to the pair by sampling from a power law distribution, e.g. E^{-2}. Then the muon and shower energy fractions are assigned by sampling from a discretized $\frac{d\sigma^2}{dxdy}$ ansatz that has been chosen to match the differential cross section at a fixed energy. Since both neutrinos and antineutrinos need to be simulated, when the initial lepton-hadron pair is produced a fair coin is tossed to generate either a μ^+ or μ^-. The cross sections used are the ones reported in this thesis, namely Argüelles et al. [136]. The position of the pair is specified by sampling uniformly on $\cos\theta_z$ and then again uniformly in column density on a cylinder that contains the detector and whose axis is in the direction of the primary particle, i.e. the neutrino, and its height corresponds to the 99% C.L. volume which the muon will not survive to exit due to losing energy in the medium.

[1] The IceCube MC contains a particle type call *hadrons* which is a template of a hadronic shower whose structure is energy dependent and obtained from GEANT simulation.

Once the muon and shower pair is generated, and their properties specified, the muon is propagated using `PROPOSAL` [137, 138], which is a `C++` reimplementation of `MMC` [139, 140], while the shower is propagated by CMC [141]. The Cherenkov photons arising from the charged particles are simulated by direct photon propagation using `CLSIM` [142]; which is shown to be compatible with `PPC` [143] used in older IceCube simulations. Then photon and detector simulation are performed as described in Chapter 3 of C. Weaver [16]. After which the cuts on Chapter 4 of C. Weaver [16] are applied.

A.2 Weighting the MC Events

Following the previous prescription, and for the purpose of this work, an IceCube *event* can be represented by the following structure

- MC Event
  - `TrueQuantities`
    - `injectedEnergy` corresponds to the sum of the lepton and shower energies. [GeV]
    - `intX` x of the interaction. [dimensionless]
    - `intY` y of the interaction. [dimensionless]
    - `InjectedMuonEnergy` initial energy of the muon. [GeV]
    - `injectedMuonZenith` initial zenith of the muon. [rad]
    - `inelasticityProbability` probability of given interaction. [dimensionless]
    - `totalColumnDepth` column depth where there interaction was forced. [gr/cm^2]
  - `ReconstructedQuantities`
    - `MuonEnergyProxy` muon energy proxy. [dimensionless]
    - `reconstructedMuonZenith` reconstructed muon zenith. [rad]
  - `FLWeight` Event flux-less weight. [GeV cm^2 sr]

The *true quantities* variables are mostly self explanatory and they always make reference to the particles at the interaction vertex, i.e. when the muon-shower pair is produced. Of these quantities the only one that is not self explanatory is the `inelasticityProbability` which is the probability which corresponds to having selected a given (x, y), namely it is $\frac{1}{\sigma}\frac{d^2\sigma}{dxdy}(x, y)\Delta x\Delta y$ where $\Delta x\Delta y$ is the MC kinematic sampling discretized phase space size [2]. Since the physical neutrino flux is approximately a power law in energy it is

[2] In the MC production we set $\Delta x = \Delta y = 10^{-3}$.

not efficient to generate events according to a flat energy distribution; it is better to sample according to a power law. On the other hand, the spectrum only changes linearly in zenith and azimuth, for which it makes sense to sample uniformly in $\cos\theta_z$ and ϕ_{azimuth}. Under these assumptions – when we simulate MC events from E_{min} to E_{max} with an index $\gamma \neq 1$, from $\cos\theta_{\text{min}}$ to $\cos\theta_{\text{max}}$, and from ϕ_{min} to ϕ_{max} in azimuth with equal numbers of μ^+ and μ^- [3]– the weight of a MC event is given by the following formulae

$$w_{\text{event}} = w_{\text{gen}} \times \texttt{totalColumnDepth} \times N_a \times \frac{d^2\sigma}{dxdy} \times \phi_{\overset{(-)}{\nu}} \equiv w_{\text{FL}} \times \phi_{\overset{(-)}{\nu}} \tag{A.1}$$

where N_a is Avogadro number, $\phi_{\overset{(-)}{\nu}}$ is the flux of (anti)neutrinos in the center of the detector, $\frac{d^2\sigma}{dxdy}$ the charge current (anti)neutrino cross section, and w_{gen} is the MC generation weight which is

$$w_{\text{mc}} = \frac{1}{0.5} \frac{\Delta x \Delta y}{\texttt{inelasticityProbability}} \frac{1}{N_{MC}} \frac{\Omega_{\text{gen}} A_{\text{gen}}}{E^{-\gamma}} \frac{E_{\text{max}}^{1-\gamma} - E_{\text{min}}^{1-\gamma}}{(1-\gamma)} \tag{A.2}$$

where E is the event injected energy, N_{MC} is the number of MC events, 0.5 arrises from the fact that we have generated equal amounts of neutrinos and antineutrinos, $\Omega = \Delta\phi_a \Delta\cos\theta_z$ is the generation solid angle, and $A_{\text{gen}} = \pi R_{\text{inj}}^2$ is the injection area [4]. Finally, Eq. A.1 also introduces the flux-less weight (w_{FL}) which is given in the digital appendix as `FLWeight` in units of GeV cm^2 sr; i.e. if the flux is given in units of GeV^{-1}cm^{-2}sr^{-1}s^{-1}, then w_{event} has units of s^{-1}, namely the event rate associated with the given flux[5].

[3] In the MC production we set $\phi_{\text{a,min}} = 0$, $\phi_{\text{a,max}} = 2\pi$, $\theta_{z,min} = 80°$, $\theta_{z,max} = 180°$, $E_{\text{min}} = 10^2$GeV, and $E_{\text{max}} = 10^6$GeV.

[4] In the MC production we set $R_{\text{inj}} = 800m$.

[5] The Sterile analysis lifetime was of 8249.6 hours.